Near-Infrared-Emissive π-Conjugated Polymers Based on Five-Coordinated Silicon Formazanate Complexes

Shunichiro Ito, Yoshinori Ito, Kazuo Tanaka, Yoshiki Chujo*

Department of Polymer Chemistry, Graduate School of Engineering, Kyoto University

Katsura, Nishikyo-ku, Kyoto 615-8510, Japan

E-mail: tanaka@poly.synchem.kyoto-u.ac.jp

Keywords: Silicon Complex; π-Conjugated Polymer; Near-Infrared Emission

TOC Graphic

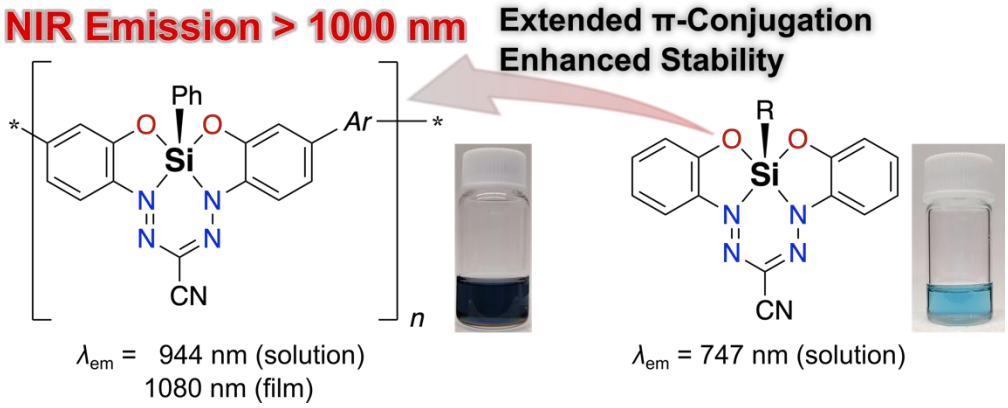
NIR Emission > 1000 nm
Extended π-Conjugation
Enhanced Stability
Ph
Si
O
O
Ar
*
*
N
N
N
N
CN
n
R
λem = 944 nm (solution)
1080 nm (film)
λem = 747 nm (solution)

Abstract

Organic compounds interacting with near-infrared (NIR) light are vital for developing next-generation functional materials. Herein, silicon formazanate complexes and their conjugated polymers with near-infrared luminescence were synthesized using the N_2O_2-type formazanate ligands. In the calculated geometries, the silicon atom possessed square-pyramidal structures. Interestingly, the photophysical properties of the complexes were strongly affected by the types of axial ligands. π-Conjugation efficiently extended through the polymer chains, resulting in narrow energy gaps between frontier orbitals. The emission band from spin-coat films reached the NIR II region (> 1000 nm). Theoretical calculations revealed that the square-pyramidal structure at the coordination center should be responsible for the efficient π-conjugation.

Introduction

Luminescent materials with far-red (FR) to near-infrared (NIR, 700–2,500 nm) emission have been developed with intensive efforts in the recent years because of their potential applications in telecommunications, bio-imaging, photovoltaic cells, and light-emitting devices.[1–8] For obtaining NIR emission, we need materials with a narrow gap (E_g) between energy levels of highest occupied molecular orbital (HOMO) and lowest unoccupied molecular orbital (LUMO). For instance, a molecule with 1.78 eV of E_g can emit light at 700 nm. The strategies for constructing NIR materials could be classified roughly into the following three categories: (1) extension of π-conjugation,[9] (2) construction of intramolecular charge transfer (ICT) systems,[4] and (3) utilization of intermolecular interactions.[10,11] In this context, π-conjugated polymers are one of the most fruitful candidates because of their delocalized electronic structures, outstanding designability of ICT, and strong interchain interactions.[12–14] However, there are still limited examples of NIR-emitting polymers. Emission in over 1000 nm region, especially, is quite rare.

Formazanate complexes of typical elements often possess relatively narrow energy gaps despite their small π-conjugated planes (Figure 1). Therefore, optically and electrochemically functional materials have been emergingly developed,[15–22] including polymers.[23–26] Particularly, Gilroy *et al.* have reported red to NIR emission from boron formazanate complexes such as **B-Ph** in Figure 1b.[15–18,20] In a formazanate scaffold, the two nitrogen atoms are located on the 2- and 4-positions where the LUMO distributes significantly, but the HOMO does not (Figure 1a). Hence, the LUMO should be lowered in energy more efficiently than the HOMO, resulting in a narrow E_g.[7,26] We have recently reported π-conjugated polymers containing a boron formazanate complex exhibit NIR emission (Figure 1b).[26] However, the some portions

of the emission wavelength was still in the visible region (emission maxima, $\lambda_{em,max}$ = 751 nm). This is probably because the sterically hindered structure of the boron formazanate unit hampers the extension of the π-conjugation. Therefore, we envisioned that purely invisible emission could be obtained from formazanate-based polymers if the planarity of the complex moiety is enhanced. Herein, we were planning to take advantage of silicon complexes of N_2O_2-type formazanate ligands. Gilroy *et al.* reported that **Si-Ph** showed a significantly narrow E_g derived from its planar ligand structure. The peculiar square-pyramidal coordination structure is responsible for such planarity.[27] Although this report did not show the emission behavior of the complex, we postulated planarity would allow the π-conjugation to extend efficiently over polymer main chains and afford much longer emission wavelengths.

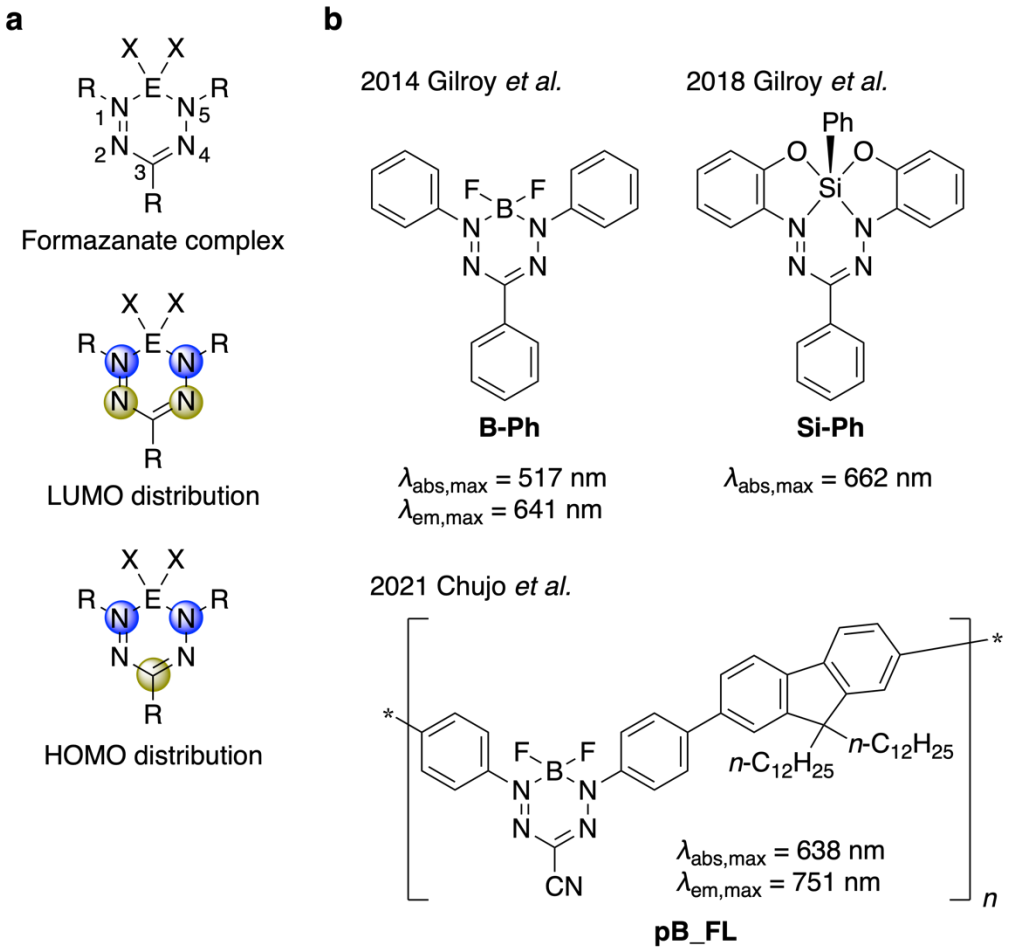

Figure 1. (a) Illustration of typical frontier orbital distributions of formazanate complexes. Blue and gold colors represent the phase of wavefunctions. (b) Previously reported formazanate-based NIR chromophores.

Results and Discussion

The synthetic scheme of the formazanate complexes is shown in Scheme 1. The nitrile group was chosen as the substituent at the 3-position because a nitrile-substituted boron complex emits more efficiently than the phenyl-substituted one.[15,16] Formazan proligands containing hydroxyl groups **L_H** and **L_Br** were synthesized from 2-cyanoacetic acid and hydroxyl-substituted diazonium salts according to the procedure reported by Gilroy *et al.*.[28] The alkyl or aryl substituted silicon complexes were prepared by the reaction of the proligands with substituted trichlorosilanes in the presence of triethylamine. The similar procedures for the synthesis of pentacoordinated silicon complexes have been reported.[27,29] The reaction of **L_H** and tetrachlorosilane afforded the product possessing a Si–O bond despite a chlorosilane complex. The unstable Si–Cl bond was hydrolyzed by atmospheric moisture. According to the literature, the silanol-containing complex may be in equilibrium with the corresponding disiloxane dimer.[29,30] Our attempt to determine the structure of the product has shown no evidence of the presence of disiloxane **SiOSi_H**. The DOSY spectrum of the product, especially, allowed us to determine only one diffusion coefficient. Therefore, the estimated structure of **SiOH_H** was employed for the further measurements of photophysical and electrochemical properties.

It should be noted that the five-coordinated silicon complexes gradually decomposed under air at room temperature. The rate of the decomposition was highly dependent on the axial ligand. In the ^{1}H NMR spectra (*ca.* 10 mg/mL, under air), the decomposition of **SiMe_H** was detected 12 hours after the sample preparation, while those of the aryl substituted complexes were not detected even after 3 days (Figure S51).

Scheme 1. Synthetic scheme of five-coordinated silicon formazanates

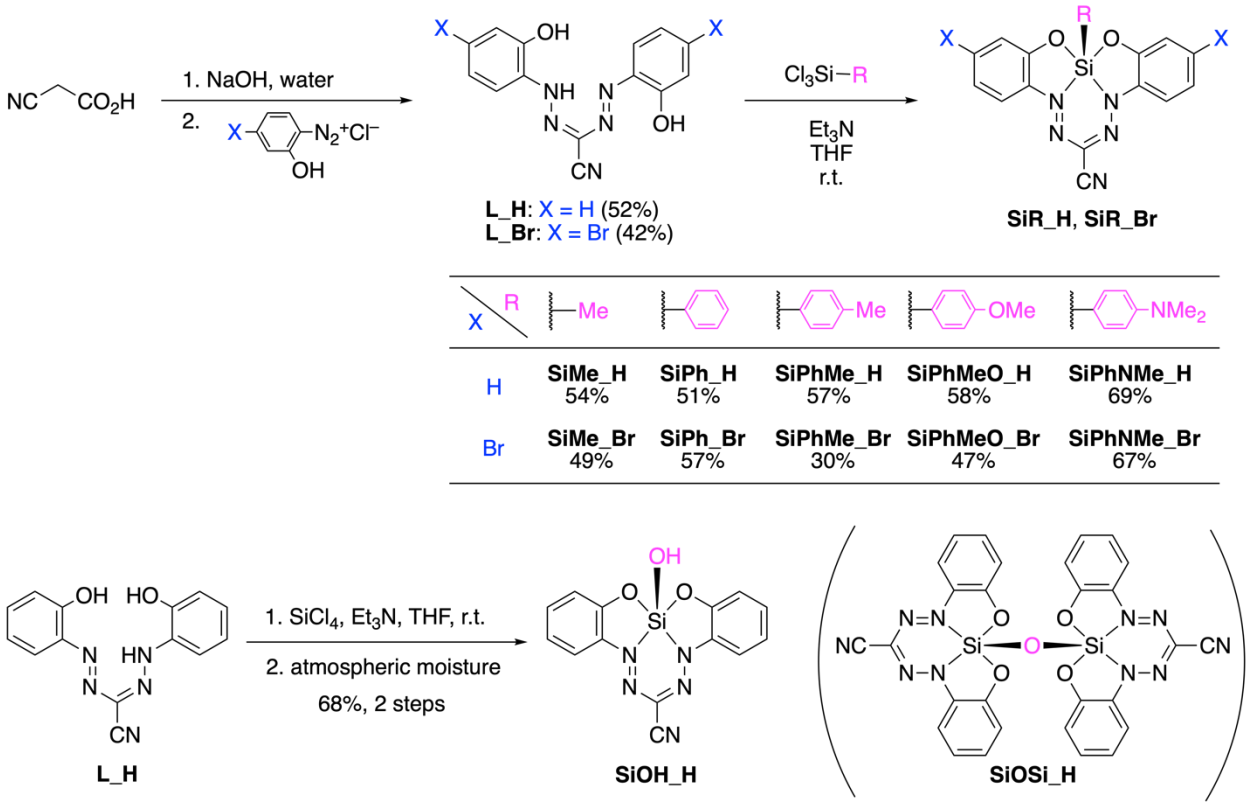

π-Conjugated polymers composed of silicon formazanate were synthesized with the palladium-catalyzed Migita–Kosugi–Stille cross coupling reaction (Scheme 2). **SiPh_Br** was used as a monomer for these polymerizations because of its stability and the best luminescent efficiency. The formazanate complex moiety was expected to act as an electron-acceptor because of its nitrogen-rich scaffold. Fluorene and bithiophene units were employed as electron-donor-type comonomers for constructing donor–acceptor polymers. The polymeric products were purified by the reprecipitation from hexane. Number- and weight-average molecular weights (M_n and M_w) of the polymers were estimated with polystyrene-standard size-exclusion chromatography (Table 1). Both polymers were confirmed to have enough molecular weights (M_w > 10,000). $^{29}Si\{^{1}H\}$ NMR spectra of each polymer showed singlet peak at –110.5 ppm for

pSi_FL and –110.4 ppm for **pSi_BT**. These chemical shift values are like that of **SiPh_Br** (–110.7 ppm) and consistent with reported pentacoordinate silicon complexes.[27,29] These observations and ^{1}H and ^{13}C{^{1}H} NMR spectra revealed that the synthesized polymers possessed the desired chemical structures and had enough purity for further photophysical and electrochemical analyses.

Scheme 2. Palladium-catalyzed polymerizations of silicon formazanate complexes with donor comonomers

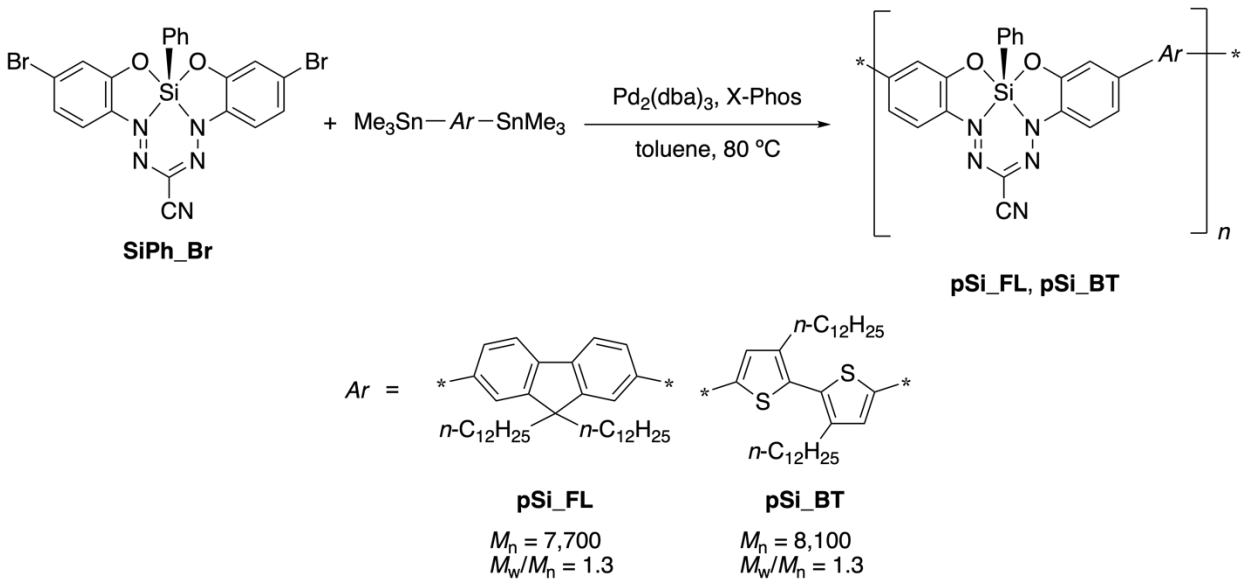

Table 1. Results of polymerizations

	M_n[a]	M_w[a]	$Đ$[b]	n[c]
pSi_FL	7,700	10,000	1.3	8.8
pSi_BT	8,100	11,000	1.3	9.1

[a]Estimated by size-exclusion chromatography based on polystyrene standards in chloroform. [b]Dispersity $Đ = M_w/M_n$. [c]Number-average degree of polymerization.

Properties of Silicon Formazanates

UV–vis absorption and photoluminescence spectra of the monomeric complexes and the proligands were recorded in their toluene solutions (1.0×10^{-5} M) as shown in Figures 2 and S1. The determined photophysical properties are listed in Table 2. The absorption bands of the proligand **L_H** ($\lambda_{abs,max}$ = 481 nm) and **L_Br** ($\lambda_{abs,max}$ = 485 nm) were bathochromically shifted to over the 600-nm region by the complexation. The absorption wavelengths were consistent with the previously-reported value for the silicon formazanate complex ($\lambda_{abs,max}$ = 662 nm).[27] The silicon complexes, except for **SiPhNMe_H**, emitted deep red to NIR fluorescence with 0.01–0.03 of absolute quantum yields (Φ_{PL}), while the photoluminescence from the proligands was not detectable. The delocalization of π-electrons and the restriction of molecular motions by the silicon complexations should be responsible for these bathochromic shifts of their absorption bands and enhancement of their luminescence.

The silicon chelation with the formazanate ligand strongly affected the absorption and emission properties. **SiOH_H** showed absorption and emission bands in the shorter-wavelength region ($\lambda_{abs,max}$ = 616 nm, $\lambda_{em,max}$ = 705 nm) than the alkyl- or aryl-substituted complexes. This hypsochromic shift should be originated from larger electronegativity of the oxygen atom of the OH ligand than the carbon atom of the alkyl or aryl ligands. The absorption and emission bands of **SiMe_H** and **SiMe_Br** were observed in slightly higher energy region than those of the corresponding complexes with an aryl group on silicon. The origin of this difference between alkyl and aryl complexes might be the slight change in electronegativity of a carbon atom attached to the silicon atom: An sp^2 carbon is slightly more electronegative than an sp^3 carbon. Indeed, the complexes bearing phenyl, tolyl and methoxyphenyl groups exhibited almost the

same photophysical properties compared among the same ligands. It should be noted that the emission from **SiPhNMe_H** was not detectable under this condition, while **SiPhNMe_Br** exhibited weak emission ($\lambda_{em,max}$ = 761 nm, Φ_{PL} < 0.01). Such weak emissions would be derived from the strong electron-donating nature of the dimethylamine group. In addition, the absorption edges of the **SiPhNMe_H** and **SiPhNMe_Br** were left a trail in the longer-wavelength regions compared to the other complexes. These observations implied that the strong donor, NMe_2 group, should construct a high-energy HOMO for these complexes.

The absorption and emission of the dibrominated compounds (**SiR_Br**) were observed in the longer-wavelength regions than those of the non-substituted ones (**SiR_H**). In addition, **SiR_Br** showed more efficient fluorescence (Φ_{PL} = 0.02–0.03) than **SiR_H** (Φ_{PL} = 0.01–0.02). These effects by the bromination suggest that the π-conjugation could extend over the bromine atoms.

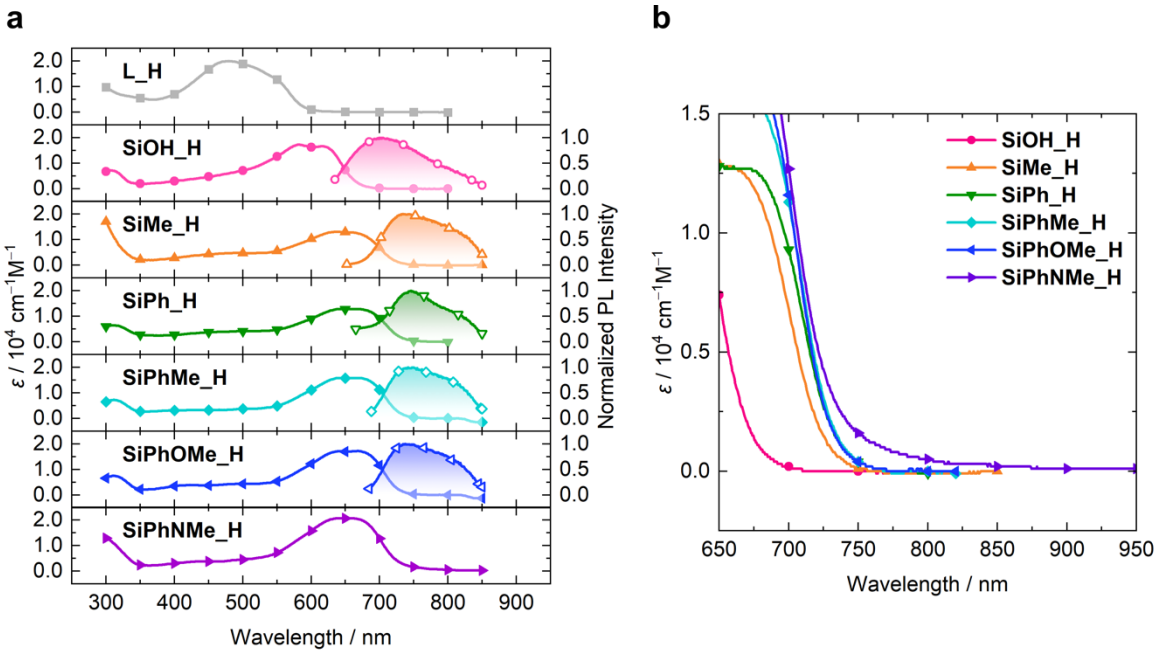

Figure 2. (a) UV–vis absorption and normalized photoluminescence spectra of the toluene solutions (1.0×10^{-5} M) of silicon formazanate complexes and proligand **L_H**. (b) Absorption edge of the complexes.

Table 2. Photophysical properties of silicon formazanate complexes and proligands

	$\lambda_{abs,max}$ / nm	$\lambda_{abs,onset}$ / nm	ε_{max} / 10^4 cm^{-1} M^{-1}	$\lambda_{em,max}$ / nm	Φ_{PL}
L_H	481	591	2.0	—	—
SiOH_H	584, 616	669	1.7	705	0.02
SiMe_H	639, 661	725	1.6	743	0.01
SiPh_H	646, 667	733	1.7	747	0.01
SiPhMe_H	645, 669	732	1.6	742	0.01
SiPhOMe_H	644, 669	729	1.7	737	0.01
SiPhNMe_H	650	730	2.1	—	—
L_Br	485	604	1.9	—	—
SiMe_Br	652, 683	741	2.6	743	0.02
SiPh_Br	660, 693	749	2.4	751	0.03
SiPhMe_Br	659, 694	744	2.3	750	0.03
SiPhOMe_Br	655, 691	746	2.4	748	0.03
SiPhNMe_Br	650, 684	744	2.3	761	< 0.01

Electrochemical properties of the silicon complexes were evaluated with cyclic voltammetry (CV) with their dichloromethane (DCM) solutions (1.0×10^{-3} M). Tetrabutylammonium hexafluorophosphate (NBu_4PF_6, 0.1 M) was used as a supporting electrolyte. The ferrocenium/ferrocene (Fc^+/Fc) redox couple was used as an external standard. The voltammograms of the alkyl- and aryl-substituted complexes showed two (pseudo)reversible reduction waves at around –0.7 and –1.7 V for **SiR_H** and –0.6 and –1.6 V for **SiR_Br** (Figure 3). The LUMO energy levels of these complexes were estimated from the onset potentials of their first reduction waves (Table 3). On the other hand, the oxidation waves of all the complexes, except for **SiPhNMe_H** and **SiPhNMe_Br**, were irreversible. Therefore, the HOMO energy

levels of these complexes were not determined from the electrochemical properties. We estimated the HOMO levels by using optical gaps (ΔE_{opt}) determined from the onset of absorption spectra ($\lambda_{abs,onset}$) as shown in Table 3. For the dimethylamine-substituted complexes, pseudoreversible oxidation waves were detected at 0.72 V (onset) for **SiPhNMe_H** and 0.75 V (onset) for **SiPhNMe_Br**. These peaks were able to be assigned to the oxidation of the dimethylaminophenyl groups. In the voltammogram of **SiOH_H**, the additional irreversible reduction wave was observed at –0.86 V. This peak might be attributable to the evolution of hydrogen originated from the silanol group. It is worthy to note that the silicon complexation can contribute to improvident of reduction stability of the complexes because the redox waves of the proligands were not reversible.

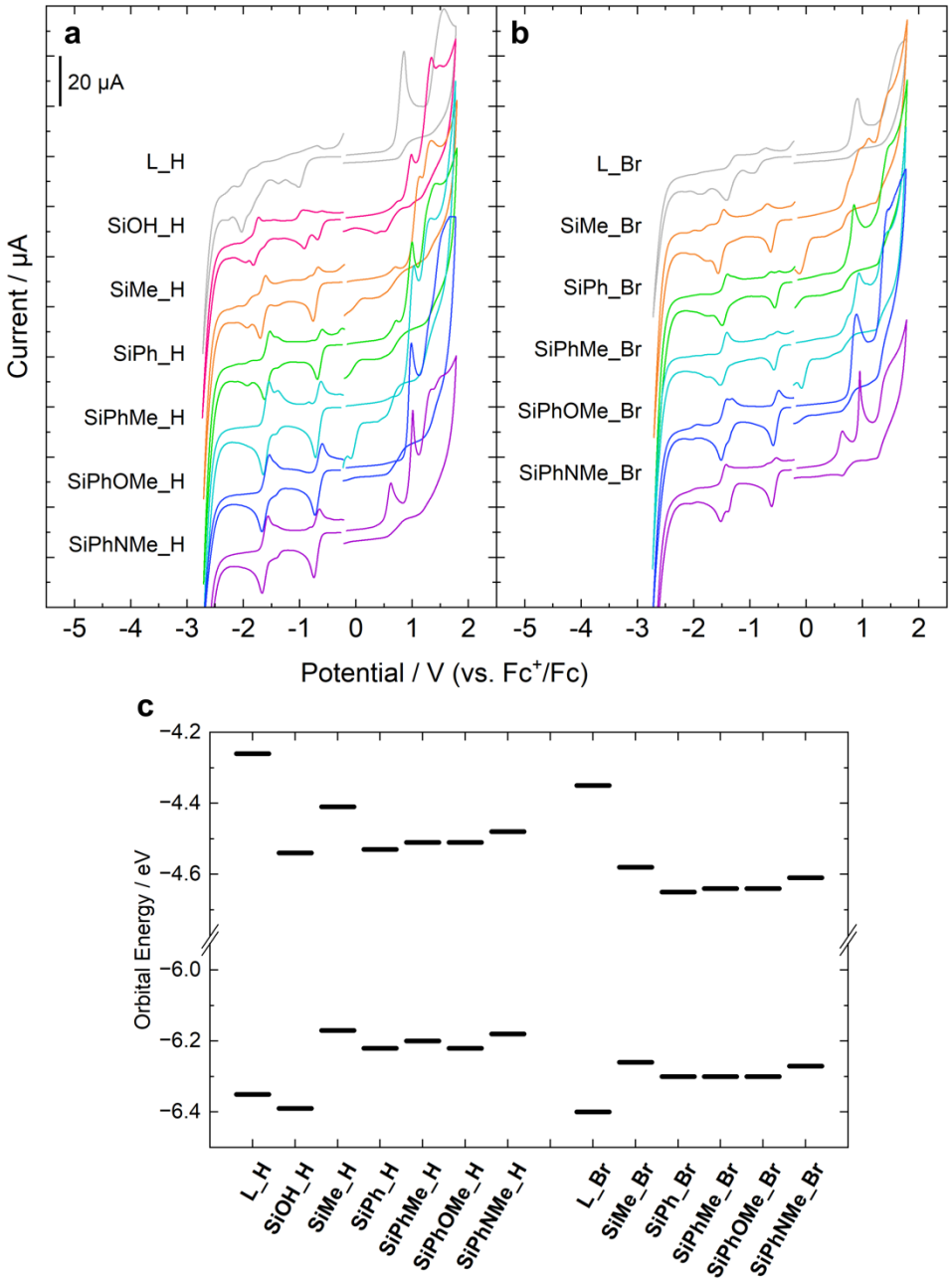

Figure 3. Voltammograms for the silicon formazanates and the proligands (a) without and (b) with bromo groups in DCM (1.0×10^{-3} M) in the presence of NBu_4PF_6 (0.1 M) as a supporting electrolyte. Redox potential was calibrated with the ferrocenium/ferrocene (Fc^+/Fc) redox couple as 0 V. (c) Estimated frontier orbital energy diagram of the complexes.

Table 3. Results of cyclic voltammetry and estimated frontier orbital energies

	$E_{red,onset}$ / V vs. Fc^+/Fc[a]	ΔE_{opt} / eV[b]	E_{LUMO} / eV[c]	E_{HOMO} / eV[d]
L_H	–0.85	2.10	–4.26	–6.35
SiOH_H	–0.56	1.85	–4.54	–6.39
SiMe_H	–0.64	1.71	–4.41	–6.17
SiPh_H	–0.57	1.69	–4.53	–6.22
SiPhMe_H	–0.59	1.69	–4.51	–6.20
SiPhOMe_H	–0.59	1.70	–4.51	–6.22
SiPhNMe_H	–0.62	1.70	–4.48	–6.18
L_Br	–0.75	2.05	–4.35	–6.40
SiMe_Br	–0.52	1.67	–4.58	–6.26
SiPh_Br	–0.45	1.66	–4.65	–6.30
SiPhMe_Br	–0.47	1.67	–4.64	–6.30
SiPhOMe_Br	–0.47	1.66	–4.64	–6.30
SiPhNMe_Br	–0.49	1.67	–4.61	–6.27

[a]Measured in dichloromethane solutions (1.0×10^{-3} M) containing 0.1 M tetrabutylammonium hexafluorophosphate (Bu_4NPF_6) as a supporting electrolyte, using a glassy carbon working electrode, a Pt wire counter electrode, an Ag/Ag^+ reference electrode, and a ferrocenium/ferrocene external standard at room temperature with a scan rate of 0.1 Vs^{-1}. [b]Optical gap determined from the onset wavelengths of absorption spectra ($\lambda_{abs,onset}$). $E_{g,opt}$ / eV = 1240 / ($\lambda_{abs,onset}$ / nm). [c]E_{LUMO} / eV = –5.10 – $E_{red,onset}$ / V. [d]E_{HOMO} / eV = E_{LUMO} / eV – ΔE_{opt} / eV.

To evaluate the electronic structures of the complexes, we performed density functional theory (DFT) and time-dependent DFT (TD-DFT) calculations at the B3LYP/6-31+G(d,p) level of theory with the Gaussian 16 package.[31] The polarizable continuum model (toluene) was employed as well. All optimized geometries were checked as local minima with frequency calculations. All silicon complexes were optimized to square-pyramidal structures which were consistent with the previously reported crystal structures of the similar silicon formazanate.[27] Several structural parameters were listed in Table S1.

The calculated energy diagram for the silicon complexes without bromine atoms were shown in Figure 4. The corresponding data for **SiR_Br** were shown in Figure S2. The HOMOs of **SiOH_H**, **SiMe_H**, **SiPhMe_H**, and **SiPhOMe_H** and the HOMO–1 of **SiPhNMe_H** showed similar distributions. The strong absorption bands of these complexes in the far-red region should be originated mainly from the electronic transitions from these HOMOs or HOMO–1 to their LUMOs (π–π* transitions). Importantly, these occupied orbitals possessed large contributions from the silicon atoms, indicating significant σ-conjugation. The square-pyramidal structures of these complexes should be responsible for such σ-conjugation, since the similar orbital distributions were observed in the previously reported complex with the square-pyramidal structure.[27] On the other hand, silicon complexes of dipyrrin with the trigonal-bipyramidal structures showed no such σ-conjugation through a silicon atom.[32] The square-pyramidal structures provided the coplanarity of the formazanate ligands and allowed the σ-orbital of silicon to interact with the π-orbitals. Therefore, the square-pyramidal structures of silicon play a significant role for the extension of π-conjugation. It should be noted that the HOMOs of group 13 element formazanates showed no contribution from the coordination center[15] even in the hexacoordinated aluminum complex which has a coplanar ligand scaffold.[33]

The HOMOs of **SiPhNMe_H** and **SiPhNMe_Br** were localized on the dimethylaminophenyl moiety due to the strong electron-donating nature of the NMe_2 group. They were located 0.45 and 0.49 eV higher than the HOMO–1 which were attributed to the π* orbital of the formazanate moiety. The first excited states (S_1) of **SiPhNMe_H** (1.49 eV, f = 0.08) and **SiPhNMe_Br** (1.41 eV, f = 0.09) were composed of the transition from the dimethylaminophenyl moiety (HOMO) to the formazanate moiety (LUMO). Thus, these S_1 states exhibited the intramolecular charge transfer (ICT) property. The oscillator strengths (f) for the S_0–S_1 transitions (0.08 for

SiPhNMe_H and 0.09 for **SiPhNMe_Br**) were almost negligible because the HOMO–LUMO overlaps are quite small. These results were consistent with the characteristic long tails of the absorption edges of **SiPhNMe_H** and **SiPhNMe_Br**. As a result, the emission from **SiPhNMe_H** and **SiPhNMe_Br** was not detectable or quite weak ($\Phi_{PL} < 0.01$). The emission spectrum of **SiPhNMe_Br** showed a vibrational structure and was a mirror image of its absorption spectrum and similar to other aryl-substituted complexes. These observations suggest that **SiPhNMe_Br** could emit from its S_2 state (anti-Kasha emission). The occupied orbitals of the axial aryl groups can be found in the HOMO–1 of **SiPhOMe_H** and **SiPhOMe_Br** with even lower energies from the π-orbitals of the ligand.

The HOMO of **SiOH_H** was significantly lower than those of the other complexes, while its LUMO was comparable to the others. As a result, the S_0–S_1 transition energy (2.22 eV) of **SiOH_H** was larger than the other complexes. This calculation was consistent with the experimental results. To clarify the origin of the stabilization of the HOMO of **SiOH_H**, we carried out natural bond orbital (NBO) analysis for **SiOH_H** and **SiMe_H** (Figures S3 and S4, and Tables S2–S3). The results of NBO analyses indicate that the energy of the NBO of the oxygen atom in the OH ligand (–10.47 eV) is lower than that of the carbon atom in the methyl ligand (–5.16 eV). This lower-lying NBO of oxygen is consistent with the electronegative nature of oxygen, and leads to the deep HOMO of **SiOH_H**.

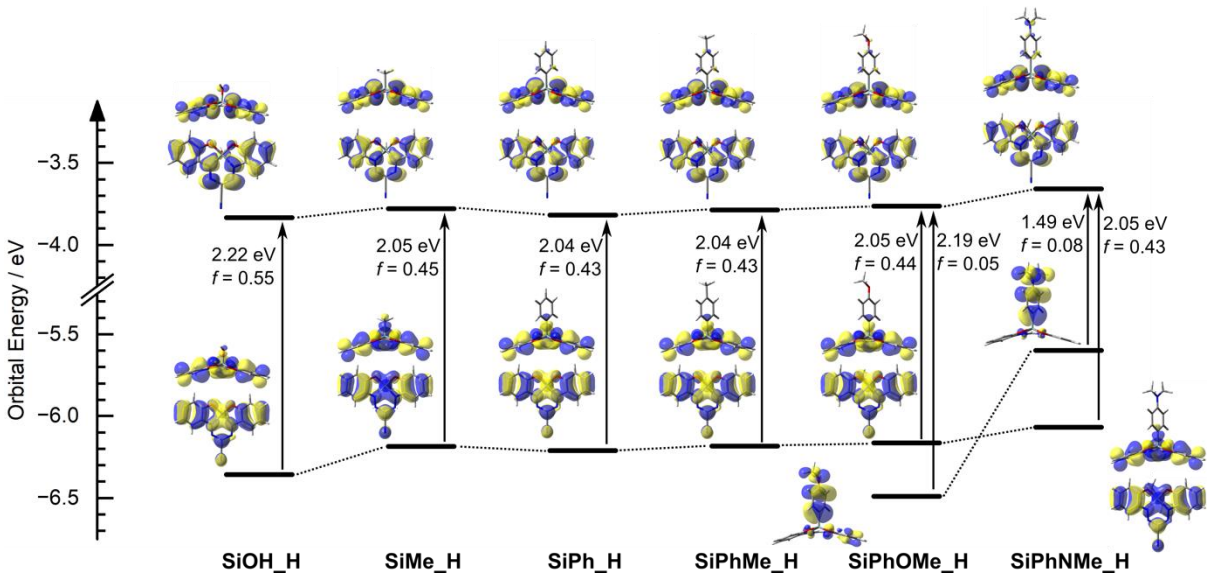

Figure 4. Frontier orbital energy diagram of **SiR_H**. Kohn–Sham molecular orbitals were illustrated with 0.02 of isovalue. Both of front and side views were shown, except for the HOMO–1 of **SiPhOMe_H** and the HOMO of **SiPhNMe_H**. Electronic transition energies were listed with the corresponding oscillator strengths (*f*).

Properties of polymers

The UV–vis absorption and emission spectra of **pSi_FL** and **pSi_BT** showed significant bathochromic shift compared with **Si_Ph** (Figure 5a, Table 4). The emission spectra of **pSi_FL** (852 nm) and **pSi_BT** (944 nm) were peaked in the NIR region and completely out of the visible region. These results strongly indicate that the efficient electronic communication between the formazanate and donor comonomer moieties lead the bathochromic shifts. Importantly, the absolute quantum yields dramatically increased to 0.04 for **pSi_FL** compared to **SiPh_H** (0.01). The quantum yield of **pSi_BT** was prevented from severe quenching despite its significantly low energy emission. Moreover, these silicon formazanate-based polymers showed absorption and

emission in much lower energy regions than the previously reported conjugated polymer composed of boron formazanate and fluorene ($\lambda_{abs,max}$ = 638 nm and $\lambda_{em,max}$ = 751 nm).[26] These observations clearly indicate that the polymerization of silicon formazanates with donor comonomers is one of the efficient ways to construct NIR emitters. To evaluate the ICT property of these polymers, we recorded the absorption and emission spectra in some solvents and prepared the Lippert–Mataga plots (Figure 5b). The relatively keen slopes of these polymers (2300 cm^{-1} for **pSi_FL** and 3400 cm^{-1} for **pSi_BT**) indicate that these polymers possessed the ICT property. The larger value of the slope for **pSi_BT** agreed with the stronger electron-donating nature of bithiophene.

Optical properties of the polymers were also recorded with spin-coat films (Figure 5a, hollow marks). For both polymers, the absorption edges of the films were observed in the lower-energy region ($\lambda_{abs,onset}$ = 906 nm for **pSi_FL** and 1032 nm for **pSi_BT**) than those of the solutions (Table 4). Furthermore, the emission wavelengths were shifted to 944 nm for **pSi_FL** and 1080 nm for **pSi_BT**. The large portion of the emission bands of these films reached the NIR II region (1000–1700 nm). The bathochromic shifts of the spectra could be derived from interchain interactions or extension of π-conjugation lengths.

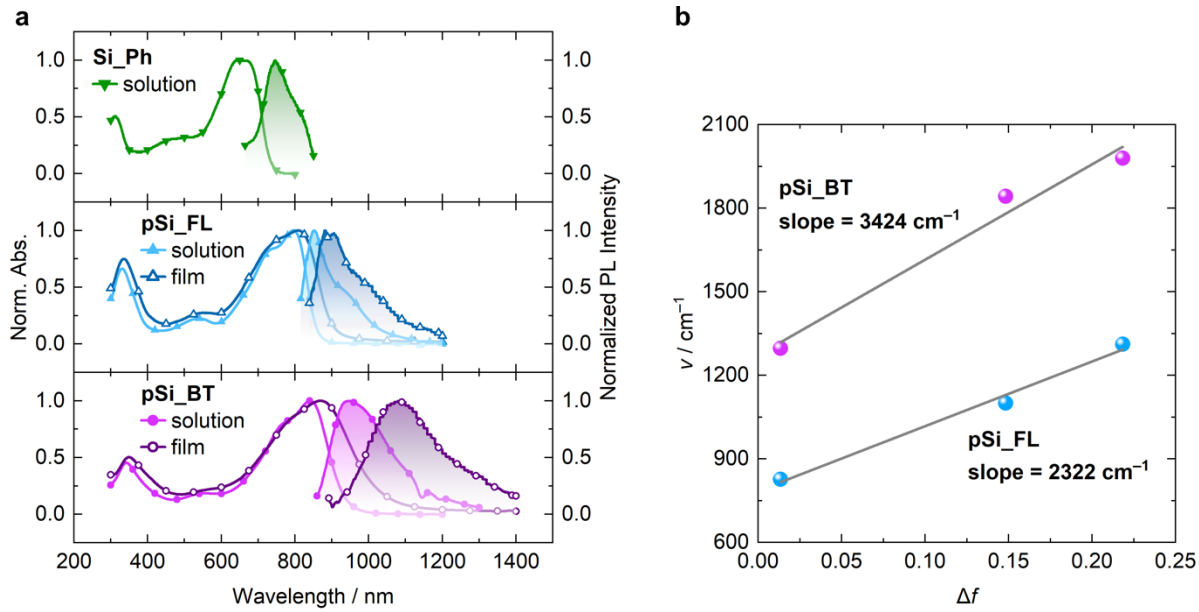

Figure 5. (a) UV–vis absorption and photoluminescence spectra of π-conjugated polymers containing silicon formazanate in $CHCl_3$ solutions (1.0×10^{-5} M for repeating unit, filled marks) and spin-coat films (hollow marks). The dips (~1140 and ~1190 nm) in the emission spectrum of **pSi_BT** were assigned to the vibrational absorption of water. (b) Lippert–Mataga plots for the polymers. ν and Δf are Stokes shift and Lippert's polarity parameter, respectively. The slopes were determined with a least-square method.

Table 4. Photophysical properties of π-conjugated polymers composed of silicon formazanates

		$\lambda_{abs,max}$ / nm	$\lambda_{abs,onset}$ / nm	ε_{max} / 10^4 cm^{-1} M^{-1}	$\lambda_{em,max}$ / nm	Φ_{PL}
pSi_FL	solution	796	860	4.0	852	0.04
	film	807	906		882	<0.01
pSi_BT	solution	841	937	4.0	944	0.01
	film	870	1032		1080	<0.01

The frontier orbital energies of the polymers were estimated from reduction waves of CV and optical band gaps (Figure 6 and Table 5). The LUMO levels of the polymers (–4.54 eV for **pSi_FL** and –4.55 eV for **pSi_BT**) were estimated to be almost the same value of **SiPh_H** (–4.53 eV). On the other hand, the HOMO levels were highly dependent on the donor comonomers (–5.98 eV for **pSi_FL** and –5.87 eV for **pSi_BT**) as typical donor–acceptor polymers. It is also worth to note that the two distinct reversible reduction waves in the voltammograms were found even after the polymerization. This stable electron-accepting nature of silicon formazanates suggests that these polymers could be potentially applied to acceptor materials for organic photovoltaics and field-effect transistors.

Importantly, the LUMO level of the previously reported boron formazanate-containing conjugated polymer was electrochemically estimated to be –4.53 eV, which is almost the same as **pSi_FL** (–4.54 eV) and the corresponding boron formazanate (–4.53 eV). In contrast, the absorption and emission bands of the boron polymer ($\lambda_{abs,max}$ = 638 nm and $\lambda_{em,max}$ = 751 nm) were located at the significantly higher energies than those of **pSi_FL**.[26] These results clearly indicate that HOMO levels of these formazanate-containing polymers should be strongly affected not only by the structures of the comonomer but also the formazanate moieties despite the donor–acceptor nature of the main chains.

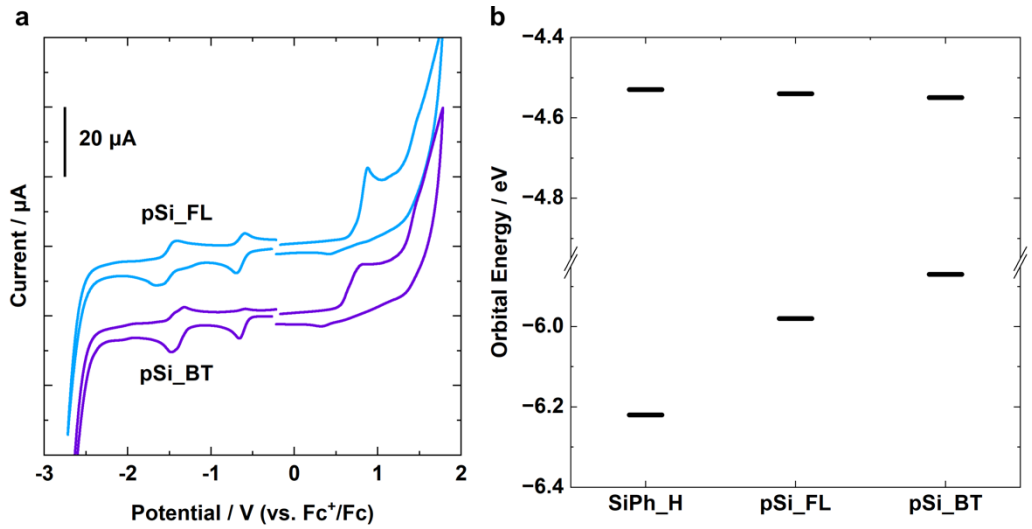

Figure 6. (a) Voltammograms for **pSi_FL** and **pSi_BT** in DCM (1.0×10^{-3} M) in the presence of NBu_4PF_6 (0.1 M) as a supporting electrolyte. Redox potential was calibrated with the ferrocenium/ferrocene (Fc^+/Fc) redox couple as 0 V. (b) Estimated frontier orbital energy diagram of the polymers.

Table 5. Results of cyclic voltammetry and estimated frontier orbital energies of the polymers

	$E_{red,onset}$ / V vs. Fc^+/Fc^a	ΔE_{opt} / eV^b	E_{LUMO} / eV^c	E_{HOMO} / eV^d
pSi_FL	–0.56	1.44	–4.54	–5.98
pSi_BT	–0.55	1.32	–4.55	–5.87

^{a}Measured in dichloromethane solutions (1.0×10^{-3} M) containing 0.1 M tetrabutylammonium hexafluorophosphate (Bu_4NPF_6) as a supporting electrolyte, using a glassy carbon working electrode, a Pt wire counter electrode, an Ag/Ag^+ reference electrode, and a ferrocenium/ferrocene external standard at room temperature with a scan rate of 0.1 Vs^{-1}. ^{b}Optical gap determined from the onset wavelengths of absorption spectra ($\lambda_{abs,onset}$). $E_{g,opt}$ / eV = 1240 / ($\lambda_{abs,onset}$ / nm). $^c E_{LUMO}$ / eV = –5.10 – $E_{red,onset}$ / V. $^d E_{HOMO}$ / eV = E_{LUMO} / eV – ΔE_{opt} / eV.

To obtain further insight for the electronic structures of these polymers, DFT and TD-DFT calculations were performed using the model structures for each polymer (Figure 7). The LUMOs of all model compounds localized at each formazanate moiety, indicating its strong electron accepting nature. The LUMO energies were not significantly affected by the comonomers. The LUMO levels of donor–formazanate–donor type models **FL_Si_FL** and **BT_Si_BT** were located at slightly higher energy region than those of the formazanate–donor–formazanate type models **Si_FL_Si** and **Si_BT_Si** probably because of the weak inductive effects of the comonomers. The HOMOs of the models, on the other hand, delocalized over the whole molecule, indicating that the π-conjugation in the occupied orbitals could extend over at least two repeating units. The in-phase contributions from the silicon atoms remained in these HOMO distributions. The HOMOs of the models of the corresponding boron polymer much more localized at the fluorene unit. Therefore, the coplanar structure and σ-conjugation observed in silicon formazanates should result in the efficient delocalization of π-electrons along the polymer main chains.

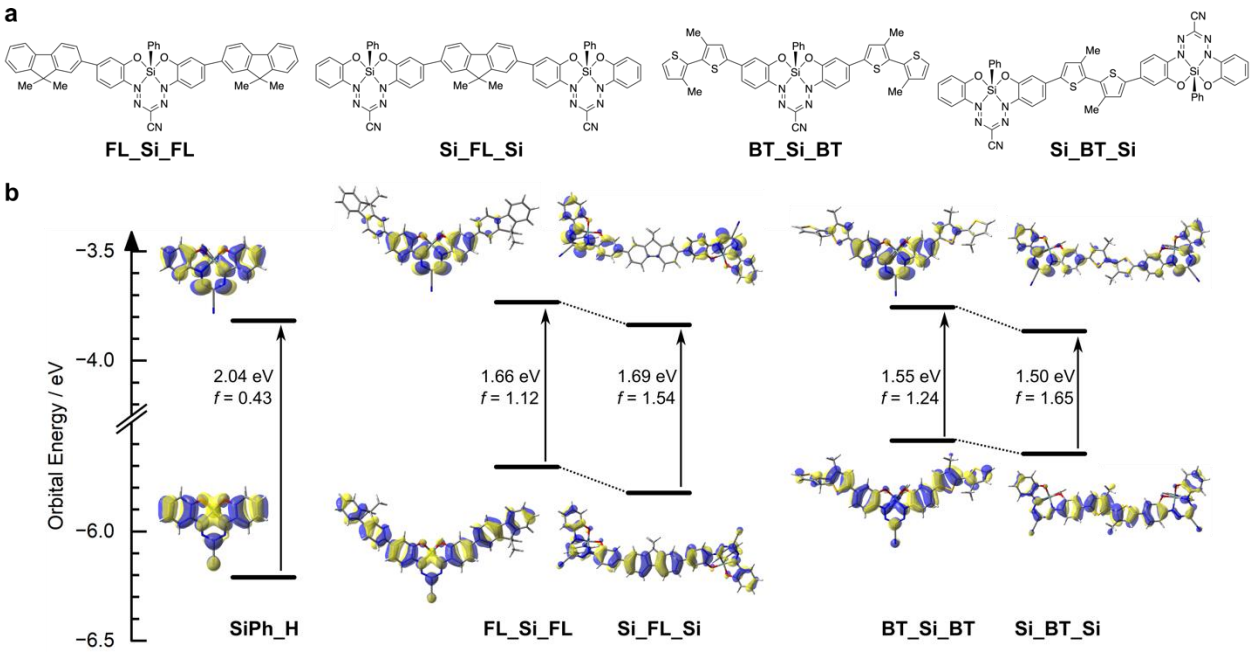

Figure 7. (a) Chemical structures of the model compounds for DFT calculations. (b) Frontier orbital energy diagram. Kohn–Sham molecular orbitals were illustrated with 0.02 of isovalue. Electronic transition energies were listed with the corresponding oscillator strengths (*f*).

Finally, we observed a dramatic increase in the durability of the photophysical properties of the polymeric compounds compared to the small molecules. Time dependence (0, 7, 10, and 15 days) of the absorption spectra in chloroform were monitored at room temperature for **SiPh_H**, **pSi_FL** and **pSi_BT** (Figure 8). The solutions were prepared under air, and each cuvette was sealed with a teflon screw cap. They were stored under the dark at room temperature. In the spectra of **SiPh_H**, gradual degradation of the complex was detected. After 15 days, the absorption bands attributed to **SiPh_H** disappeared significantly, and those of proligand **L_H** accounted for a major portion of the spectrum. The main route of the degradation of the complex should be hydrolyzation. On the other hand, the absorption properties of **pSi_FL** and **pSi_BT** were preserved even after 15 days. The polymeric structures likely limit the diffusion of

chromophores and prevent from encounter with water molecules. In addition, the local polarity of the chromophores might decrease by polymerization.

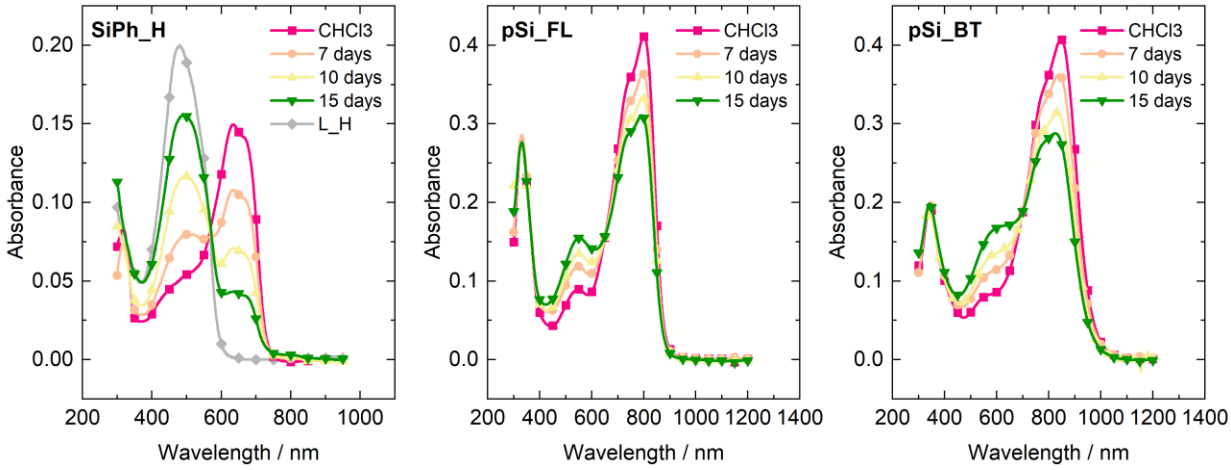

Figure 8. Degradation behavior (from 0 to 15 days) of **SiPh_H**, **pSi_FL**, and **pSi_BT** in chloroform solutions (1.0×10^{-5} M) under ambient condition.

Conclusion

We synthesized a new series of FR to NIR emissive complexes and polymers based on pentacoordinated silicon formazanates. For the small molecules, the absorption and emission bands were observed in the range from 616 to 694 nm and from 705 to 761 nm, respectively. The maximum emission wavelengths of small molecules reached 761 nm for **SiPhNMe_Br**. It is suggested that electronegativity of the non-chelating axial ligand could be responsible for the optical gaps. Bromination at the formazanate ligand enhanced the photoluminescence quantum yields and bathochromic shifts of absorption and emission bands. For the polymers in solutions, the absorption maxima were found over the 800-nm region. The peaks of emission bands from **pSi_FL** and **pSi_BT** were detected at 852 and 944 nm, respectively. These NIR emissions were originated from the strong ICT nature of the polymers. Importantly, the spin-coat film of **pSi_BT** emitted with the peak at 1080 nm, and its emission tail reached over 1400 nm. DFT and TD-DFT calculations revealed that the coplanar structure of the formazanate ligand should be responsible for the effective conjugation through silicon at the HOMO levels of the small and polymeric molecules. These results motivated us to develop NIR materials using not only silicon formazanates but also other multicoordinated typical-element complexes.

Acknowledgments

A part of computation time was provided by the SuperComputer System, Institute for Chemical Research, Kyoto University. This work was partially supported by Iketani Science and Technology Foundation (for S.I.), a Grant-in-Aid for Research Activity Start-up (for S.I.) (JSPS KAKENHI Grant Numbers 20K22532), for Early-Career Scientists (for S.I.) (JSPS KAKENHI Grant Numbers 21K14673), for Scientific Research (B) (for K.T) (JSPS KAKENHI Grant Number, 21H02001), and a Grant-in-Aid for Scientific Research on Innovative Areas “New Polymeric Materials Based on Element-Blocks (No.2401)” (JSPS KAKENHI Grant Number P24102013).

Conflict of Interest

The authors declare no conflict of interest.

CRediT authorship contribution statement

Shunichiro Ito: Conceptualization, Methodology, Validation, Formal Analysis, Investigation, Writing – Original Draft, Writing – review & editing, Visualization, Funding acquisition. **Yoshinori Ito:** Methodology, Validation, Formal Analysis, Investigation, Writing – Original Draft, Writing – review & editing, Visualization. **Kazuo Tanaka:** Conceptualization, Writing – Original Draft, Writing – review & editing, Supervision, Project administration, Funding acquisition. **Yoshiki Chujo:** Conceptualization, Writing – review & editing, Supervision, Funding acquisition.

References

[1] G. Qian, Z.Y. Wang, Near-Infrared Organic Compounds and Emerging Applications, Chem. Asian J. 5 (2010) 1006–1029.

[2] Z. Sun, Q. Ye, C. Chi, J. Wu, Low Band Gap Polycyclic Hydrocarbons : From Closed-Shell Near Infrared Dyes and Semiconductors to Open-Shell Radicals, Chem. Soc. Rev. 41 (2012) 7857–7889.

[3] H. Xiang, J. Cheng, X. Ma, X. Zhou, J.J. Chruma, Near-Infrared Phosphorescence: Materials and Applications, Chem. Soc. Rev. 42 (2013) 6128–6185.

[4] J. Qi, W. Qiao, Z.Y. Wang, Advances in Organic Near-Infrared Materials and Emerging Applications, Chem. Rec. 16 (2016) 1531–1548.

[5] Y. Ni, J. Wu, Far-Red and Near Infrared BODIPY Dyes: Synthesis and Applications for Fluorescent pH Probes and Bio-imaging, Org. Biomol. Chem. 12 (2014) 3774.

[6] Y. Ge, D.F. O'Shea, Azadipyrromethenes: From Traditional Dye Chemistry to Leading Edge Applications, Chem. Soc. Rev. 45 (2016) 3846–3864.

[7] M. Gon, S. Ito, K. Tanaka, Y. Chujo, Design Strategies and Recent Results for Near-Infrared-Emissive Materials Based on Element-Block π-Conjugated Polymers, Bull. Chem. Soc. Jpn. 94 (2021) 2290–2301.

[8] A. Zampetti, A. Minotto, F. Cacialli, Near-Infrared (NIR) Organic Light-Emitting Diodes (OLEDs): Challenges and Opportunities, Adv. Funct. Mater. 29 (2019) 1807623.

[9] N.G. Pschirer, C. Kohl, F. Nolde, J. Qu, K. Müllen, Pentarylene- and Hexarylenebis(dicarboximide)s: Near-Infrared-Absorbing Polyaromatic Dyes, Angew. Chem. Int. Ed. 45 (2006) 1401–1404.

[10] D. Tian, F. Qi, H. Ma, X. Wang, Y. Pan, R. Chen, Z. Shen, Z. Liu, L. Huang, W. Huang, Domino-Like Multi-emissions Across Red and Near Infrared from Solid-State 2-/2,6-aryl Substituted BODIPY Dyes, Nat. Commun. 9 (2018) 2688.

[11] Y.-C. Wei, S.F. Wang, Y. Hu, L.-S. Liao, D.-G. Chen, K.-H. Chang, C.-W. Wang, S.-H. Liu, W.-H. Chan, J.-L. Liao, W.-Y. Hung, T.-H. Wang, P.-T. Chen, H.-F. Hsu, Y. Chi, P.-T. Chou, Overcoming the Energy Gap Law in Near-Infrared OLEDs by Exciton–Vibration Decoupling, Nat. Photonics 14 (2020) 570–577.

[12] H.A.M. van Mullekom, J.A.J.M. Vekemans, E.E. Havinga, E.W. Meijer, Developments in the Chemistry and Band Gap Engineering of Donor–Acceptor Substituted Conjugated Polymers, Sci. Eng. R. Reports 32 (2001) 1–40.

[13] C. Winder, N.S. Sariciftci, Low Bandgap Polymers for Photon Harvesting in Bulk Heterojunction Solar Cells, J. Mater. Chem. 14 (2004) 1077–1086.

[14] J. Chen, Y. Cao, Development of Novel Conjugated Donor Polymers for High-Efficiency Bulk-Heterojunction Photovoltaic Devices, Acc. Chem. Res. 42 (2009) 1709–1718.

[15] S.M. Barbon, P.A. Reinkeluers, J.T. Price, V.N. Staroverov, J.B. Gilroy, Structurally Tunable 3-Cyanoformazanate Boron Difluoride Dyes, Chem. Eur. J. 20 (2014) 11340–11344.

[16] S.M. Barbon, J.T. Price, P.A. Reinkeluers, J.B. Gilroy, Substituent-Dependent Optical and Electrochemical Properties of Triarylformazanate Boron Difluoride Complexes, Inorg. Chem. 53 (2014) 10585–10593.

[17] S.M. Barbon, V.N. Staroverov, J.B. Gilroy, Effect of Extended π Conjugation on the Spectroscopic and Electrochemical Properties of Boron Difluoride Formazanate Complexes, J. Org. Chem. 80 (2015) 5226–5235.

[18] R.R. Maar, S.M. Barbon, N. Sharma, H. Groom, L.G. Luyt, J.B. Gilroy, Evaluation of Anisole-Substituted Boron Difluoride Formazanate Complexes for Fluorescence Cell Imaging, Chem. Eur. J. 21 (2015) 15589–15599.

[19] S.M. Barbon, J.V. Buddingh, R.R. Maar, J.B. Gilroy, Boron Difluoride Adducts of a Flexidentate Pyridine-Substituted Formazanate Ligand: Property Modulation via Protonation and Coordination Chemistry, Inorg. Chem. 56 (2017) 12003–12011.

[20] R.R. Maar, R. Zhang, D.G. Stephens, Z. Ding, J.B. Gilroy, Near-Infrared Photoluminescence and Electrochemiluminescence from a Remarkably Simple Boron Difluoride Formazanate Dye, Angew. Chem. Int. Ed. 58 (2019) 1052–1056.

[21] J.B. Gilroy, E. Otten, Formazanate Coordination Compounds: Synthesis, Reactivity, and Applications, Chem. Soc. Rev. 49 (2019) 85–113.

[22] G.N. Lipunova, T.G. Fedorchenko, O.N. Chupakhin, New Aspects of the Chemistry of Formazans, Russ. J. Gen. Chem. 89 (2019) 1225–1245.

[23] S.M. Barbon, J.B. Gilroy, Boron Difluoride Formazanate Copolymers with 9,9-Di-*n*-hexylfluorene Prepared by Copper-Catalyzed Alkyne–Azide Cycloaddition Chemistry, Polym. Chem. 7 (2016) 3589–3598.

[24] J.S. Dhindsa, R.R. Maar, S.M. Barbon, M.O. Avilés, Z.K. Powell, F. Lagugné-Labarthet, J.B. Gilroy, A π-Conjugated Inorganic Polymer Constructed from Boron Difluoride Formazanates and Platinum(II) Diynes, Chem. Commun. 54 (2018) 6899–6902.

[25] C. Kumar, A.R. Agrawal, N.G. Ghosh, H.S. Karmakar, S. Das, N.R. Kumar, V.W. Banewar, S.S. Zade, Boron Difluoride Formazanates with Thiophene and 3,4-Ethylenedioxythiophene Capping and Their Electrochemical Polymerization, Dalton Trans.. 49 (2020) 13202–13206.

[26] Y. Kawano, Y. Ito, S. Ito, K. Tanaka, Y. Chujo, π-Conjugated Copolymers Composed of Boron Formazanate and Their Application for a Wavelength Converter to Near-Infrared Light, Macromolecules 54 (2021) 1934–1942.

[27] R.R. Maar, S.D. Catingan, V.N. Staroverov, J.B. Gilroy, Formazanate Complexes of Hypervalent Group 14 Elements as Precursors to Electronically Stabilized Radicals, Angew. Chem. Int. Ed. 57 (2018) 9870–9874.

[28] J.B. Gilroy, P.O. Otieno, M.J. Ferguson, R. McDonald, R.G. Hicks, Synthesis and Characterization of 3-Cyano- and 3-Nitroformazans, Nitrogen-Rich Analogues of β-Diketimine Ligands, Inorg. Chem. 47 (2008) 1279–1286.

[29] N. Sakamoto, C. Ikeda, M. Yamamura, T. Nabeshima, Structural Interconversion and Regulation of Optical Properties of Stable Hypercoordinate Dipyrrin−Silicon Complexes, J. Am. Chem. Soc. 133 (2011) 4726–4729.

[30] T. Nabeshima, M. Yamamura, G.J. Richards, T. Nakamura, Design and Synthesis of Dipyrrin Complexes Bearing Unique Structures, Properties and Functions, J. Synth. Org. Chem. Jpn. 73 (2015) 1111–1119.

[31] M.J. Frisch, G.W. Trucks, H.B. Schlegel, G.E. Scuseria, M.A. Robb, J.R. Cheeseman, G. Scalmani, V. Barone, G.A. Petersson, H. Nakatsuji, X. Li, M. Caricato, A.V. Marenich, J. Bloino, B.G. Janesko, R. Gomperts, B. Mennucci, H.P. Hratchian, J.V. Ortiz, A.F. Izmaylov, J.L. Sonnenberg, D. Williams-Young, F. Ding, F. Lipparini, F. Egidi, J. Goings, B. Peng, A. Petrone, T. Henderson, D. Ranasinghe, V.G. Zakrzewski, J. Gao, N. Rega, G. Zheng, W. Liang, M. Hada, M. Ehara, K. Toyota, R. Fukuda, J. Hasegawa, M. Ishida, T. Nakajima, Y. Honda, O. Kitao, H. Nakai, T. Vreven, K. Throssell, J.A. Montgomery, Jr., J.E. Peralta, F. Ogliaro, M.J. Bearpark, J.J. Heyd, E.N. Brothers, K.N. Kudin, V.N. Staroverov, T.A. Keith, R. Kobayashi, J. Normand, K. Raghavachari, A.P. Rendell, J.C. Burant, S.S. Iyengar, J. Tomasi, M. Cossi, J.M. Millam, M. Klene, C. Adamo, R. Cammi, J.W. Ochterski, R.L. Martin, K. Morokuma, O. Farkas, J.B. Foresman, and D.J. Fox, Gaussian 16 Rev. C.01, Wallingford, CT, 2016.

[32] M. Yamamura, M. Albrecht, M. Albrecht, Y. Nishimura, T. Arai, T. Nabeshima, Red/Near-Infrared Luminescence Tuning of Group-14 Element Complexes of Dipyrrins Based on a Central Atom, Inorg. Chem. 53 (2014) 1355–1360.

[33] R.R. Maar, A.R. Kenaree, R. Zhang, Y. Tao, B.D. Katzman, V.N. Staroverov, Z. Ding, J.B. Gilroy, Aluminum Complexes of $N_2O_2^{3-}$ Formazanate Ligands Supported by Phosphine Oxide Donors, Inorg. Chem. 56 (2017) 12436–12447.

Supporting Information

Shunichiro Ito, Yoshinori Ito, Kazuo Tanaka, Yoshiki Chujo*

Department of Polymer Chemistry, Graduate School of Engineering, Kyoto University

Katsura, Nishikyo-ku, Kyoto 615-8510, Japan

E-mail: tanaka@poly.synchem.kyoto-u.ac.jp

Table of Contents

Experimental Section

General

^{1}H (400 MHz), $^{13}C\{^{1}H\}$ (100 MHz, 151 MHz) and $^{29}Si\{^{1}H\}$ (79, 99, 119 MHz) NMR spectra were recorded on JEOL JNM-EX400, AL400, ECZ500R and ECZ600R spectrometers. In ^{1}H, ^{13}C and ^{29}Si NMR spectra, tetramethylsilane (TMS) was used as an internal standard in CD_2Cl_2 or $CDCl_3$. High-resolution mass spectra (HRMS) were obtained on a Thermo Fisher Scientific EXACTIVE for electron spray ionization (ESI), a Thermo Fisher Scientific EXACTIVE spectrometer for direct analysis in real time (DART). Analytical thin-layer chromatography was performed with SiO_2 60 Merck F_{254} plates. Column chromatography was performed with Wakogel C-300 SiO_2. Number-average molecular weight (M_n) and molecular weight distribution ($Đ = M_w/M_n$) values of all polymers were estimated by size exclusion chromatography (SEC) with a TOSOH 8020 series (a dual pump system (DP-8020), a column oven (CO-8020), and a degasser (SD-8020)) equipped with three consecutive polystyrene gel columns (TSKgel: G4000H, G3000H and G2000H) and a refractive-index (RI-8020) and an ultraviolet detector (UV-8020) at 40 °C. The system was operated at a flow rate of 1.0 mL/min with $CHCl_3$ as an eluent. Polystyrene standards were employed for calibration. Cyclic voltammetry (CV) was carried out on a BASALS-Electrochemical-Analyzer Model 600D with a grassy carbon working electrode, a Pt counter electrode, an Ag/AgCl reference electrode, and the ferrocenenium/ferrocene (Fc^+/Fc) external reference at a scan rate of 0.1 V s^{-1}. UV−vis absorption spectra were recorded on a SHIMADZU UV–3600 or UV–3600i plus spectrophotometer. HORIBA JOBIN YVON Fluorolog-3 and Oxford Optistat DN2 were used for Photoluminescence spectra. Absolute photoluminescence quantum yields were measured with a Hamamatsu Photonics Quantaurus-QY Plus C13534-01 using a integrating sphere.

Materials

Reagents (cyanoacetic acid, 2-aminophnol, 2-amino-5-bromophenol, sodium hydroxide, sodium nitrite, hydrochloric acid, methyltrichlorosilane, phenyltrichlorosilane, tetrachlorosilane, magnesium turnings, 4-bromotoluene, 4-bromoanisole, 4-bromo-*N*,*N*-dimethylaniline, 2-dicyclohexylphosphino-2',4',6'-triisopropylbiphenyl (XPhos), tris(dibenzylideneacetone)dipalladium ($Pd_2(dba)_3$)) and solvents (hexane) were purchased from commercial sources and used without further purification. Tetrahydrofuran (THF) and triethylamine (NEt_3) were purified using a two-column solid-state purification system (Glasscontour System, Joerg Meyer, Irvine, CA).

Synthesis of Small Molecules

Synthesis of L_H

In air, cyanoacetic acid (0.510 g, 6.00 mmol) was dissolved in deionized water (40 mL) containing sodium hydroxide (2.64 g, 66.0 mmol). This colorless solution was left to stir for 30 min in an ice bath. In separate flask, 2-aminophenol (1.31 g, 12.0 mmol) in deionized water (14 mL) was cooled in an ice bath for 3 min before concentrated hydrochloric acid (3.00 mL, 36.0 mmol) was added, and stirred 20 min at 0°C. A solution of sodium nitrite (0.910 g, 6.60 mmol) in deionized water (8 mL) was cooled in an ice bath for 15 min before it was also added dropwise to the 2-aminophenol solution over a 5 min period. The resulting reddish brown diazonium salt solution was stirred in an ice bath for 30 min, and then added slowly to the basic cyanoacetic acid solution over a 15 min period. The solution turned dark red-purple mixture and was stirred in an ice bath for an additional 1 h before it was acidified by concentrated hydrochloric acid (4–5 mL) and extracted by ethyl acetate (200 mL). The organic layer was isolated, then washed with deionized water (3 × 200 mL) and dried over Na_2SO_4, gravity filtered and concentrated *in vacuo*. The resulting residue was semi-purified by column chromatography on silica gel (eluent: hexane/EtOAc = 2/1 v/v). The obtained solid was purified by reprecipitation with hexane/EtOAc to afford **L_H** (1.3 g, 4.6 mmol, 76%) as a black solid. ^{1}H NMR (DMSO-d_6, 400 MHz): δ 13.1 (s, 1H, N*H*), 10.4 (s, 1H, O*H*), 7.61 (d, *J* = 8.0 Hz, 2H, Ar-*H*), 7.23 (dd, *J* = 8.0 Hz, 2H, Ar-*H*), 7.02 (d, *J* = 8.0 Hz, 2H, Ar-*H*), 6.93 (dd, *J* = 8.0 Hz, 2H, Ar-*H*) ppm; ^{13}C{^{1}H} NMR (DMSO-d_6, 100 MHz): *δ* 150.9, 134.4, 130.3, 125.0, 120.0, 117.2, 117.1, 115.0 ppm. HRMS (n-ESI): calcd. for $[C_{14}H_{10}N_5O_2\text{-}H]^-$ 280.0840, found 280.0841.

Synthesis of L_Br

In air, cyanoacetic acid (0.510 g, 6.00 mmol) was dissolved in deionized water (40 mL) containing sodium hydroxide (2.64 g, 66.0 mmol). This colorless solution was left to stir for 30 min in an ice bath. In separate flask, 5-bromo-2-aminophenol (2.26 g, 12.0 mmol) in deionized water (14 mL) was cooled in an ice bath for 3 min before concentrated hydrochloric acid (3.00 mL, 36.0 mmol) was added, and stirred 20 min at 0 ℃. A solution of sodium nitrite (0.910 g, 6.60 mmol) in deionized water (8 mL) was cooled in an ice bath for 15 min before it was also added dropwise to the 2-aminophenol solution over a 5 min period. The solution turned yellow-brown and a yellow precipitate formed. The diazonium salt solution was stirred in an ice bath for 30 min, and then added slowly to the basic cyanoacetic acid solution over a 15 min period. The solution turned dark purple mixture and was stirred in an ice bath for an additional 1.5 h before it was acidified by concentrated hydrochloric acid (4–5 mL) and extracted by ethyl acetate (200 mL). The organic layer was isolated, then washed with deionized water (3 × 200 mL) and dried over Na_2SO_4, gravity filtered and concentrated in vacuo. The resulting residue was semi-purified by column chromatography on silica gel (eluent: hexane/EtOAc = 3/1 v/v). The obtained solid was purified by reprecipitation with hexane/EtOAc to afford **L_Br** (0.46 g, 1.0 mmol, 35%) as a black solid. ^{1}H NMR (DMSO-d_6, 400 MHz): δ 12.9 (s, 1H, N*H*), 10.9 (s, 1H, O*H*), 7.56 (d, *J* = 8.0 Hz, 2H, Ar-*H*), 7.19 (s, 2H, Ar-*H*), 7.11 (d, *J* = 8.0 Hz, 2H, Ar-*H*), ppm; ^{13}C{^{1}H} NMR (DMSO-d_6, 100 MHz): *δ* 151.9, 134.0, 125.6, 122.9, 122.4, 119.6, 118.6, 114.6 ppm. HRMS (n-ESI): calcd. for $[C_{14}H_9Br_2N_5O_2\text{-}H]^-$ 435.9050, found 435.9053.

General Procedure for the synthesis of silicon complexes

To a methyltrichlorosilane or phenyltrichlorosilane (2.30 mL, 0.40 mmol) in dry THF (2 mL) was added triethylamine (0.15 mL, 0.80 mmol) under nitrogen atmosphere. The clouded solution was stirred at room temperature for 1 h before formazan ligand **L_H** or **L_Br** (0.20 mmol) in dry THF solution (10mL) was added to the trichlorosilane solution. The solution turned blue-green and was stirred at room temperature for 16 h. The solvent was evaporated to dryness and the residue was dissolved by chloroform (50 mL), then washed with deionized water (3 × 50 mL) and dried over Mg_2SO_4, gravity filtered and concentrated *in vacuo*.

SiMe_H: The obtained solid was purified by column chromatography on silica gel (eluent : $CHCl_3$) to give **SiMe_H** (0.035 g, 0.11 mmol, 54%). ^{1}H NMR (CD_2Cl_2, 400 MHz): δ 7.83–7.81 (ddd, *J* = 8.2 Hz, 1.5 Hz, 0.7 Hz 2H, Ar-*H*), 7.50–7.46 (ddd, 8.3 Hz, 7.4 Hz, 1.5 Hz, 2H, Ar-*H*), 7.12–7.08 (m, 4H, Ar-*H*) ppm; ^{13}C{^{1}H} NMR ($CDCl_3$, 100 MHz): δ 152.1, 134.3, 134.0, 128.0, 122.3, 116.5, 116.2, 115.0, -2.46 ppm; ^{29}Si{^{1}H} NMR ($CDCl_3$, 79 MHz): δ –100.2 ppm. HRMS (DART): calcd. for $[C_{15}H_{11}N_5O_2Si+H]^+$ 322.0755, found 322.0760.

SiPh_H: The obtained solid was purified by column chromatography on silica gel (eluent : $CHCl_3$) to give **SiPh_H** (0.039 g, 0.10 mmol, 51%). ^{1}H NMR (CD_2Cl_2, 400 MHz): δ 7.88–7.86 (dd, *J* = 8.2 Hz, 1.4 Hz, 2H, Ar-*H*), 7.52-7.48 (ddd, 8.3 Hz, 7.4 Hz, 1.5 Hz, 2H, Ar-*H*), 7.39–7.35 (m, 1H, Ar-*H*), 7.28–7.10 (m, 8H, Ar-*H*) ppm; ^{13}C{^{1}H} NMR ($CDCl_3$, 100 MHz): δ 152.2, 134.8, 134.2, 133.1, 131.6, 130.1, 128.6, 128.1, 122.6, 116.6, 116.3, 114.9 ppm; ^{29}Si{^{1}H} NMR ($CDCl_3$, 79 MHz): δ –111.4 ppm. HRMS (DART): calcd. for $[C_{20}H_{13}N_5O_2Si+H]^+$ 384.0911, found 384.0915.

SiMe_Br: The obtained solid was purified by column chromatography on silica gel (eluent : $CHCl_3$) to give **SiMe_Br** (0.047 g, 0.097 mmol, 49%). ^{1}H NMR (CD_2Cl_2, 400 MHz): δ 7.83–7.81 (d, *J* = 8.7 Hz, 2H, Ar-*H*), 7.32 (d, 2.0 Hz, 2H, Ar-*H*), 7.27–7.24 (dd, 8.7 Hz, 2.0 Hz, 2H, Ar-*H*), 0.13 (s, 3H, -C*H*$_3$) ppm; ^{13}C{^{1}H} NMR ($CDCl_3$, 151 MHz): δ 152.2, 133.4, 128.5, 128.3, 126.1, 119.6, 117.6, 114.6, –2.20 ppm; ^{29}Si{^{1}H} NMR ($CDCl_3$, DEPT, 99 MHz): δ –99.2 ppm. HRMS (DART): calcd. for $[C_{15}H_9Br_2N_5O_2Si+H]^+$ 477.8965, found 477.8970.

SiPh_Br: The reaction was performed on a three times larger scale of the general procedure. The obtained solid was purified by column chromatography on silica gel (eluent: CH_2Cl_2) to give **SiPh_Br** (0.19 g, 0.34 mmol, 57%).

^{1}H NMR (CD_2Cl_2, 400 MHz): δ 7.76–7.74 (d, *J* = 8.7 Hz, 2H, Ar-*H*), 7.42–7.18 (m, 9H, Ar-*H*) ppm; ^{13}C{^{1}H} NMR ($CDCl_3$, 151 MHz): δ 152.3, 133.8, 133.0, 132.0, 129.4, 128.8, 128.7, 128.4, 126.3, 119.6, 117.6, 114.5 ppm; ^{29}Si{^{1}H} NMR ($CDCl_3$, 79 MHz): δ –110.7 ppm. HRMS (DART): calcd. for $[C_{20}H_{11}Br_2N_5O_2Si]^-$ 538.9054, found 538.9057.

General Procedure for the synthesis of aryl trichrolosilane

Two-necked pear-shaped flask was charged with magnesium turnings (0.27 g, 11.0 mmol) and heated with a heat gun under vacuum. Anhydrous THF (10 mL) was added, and the suspension was stirred for 5 min before aryl bromide was added slowly to the suspension. After the addition, the suspension turned dark gray black solution and was stirred at 50 ℃ for 3 h. In separate flask, which was heated with a heat gun under vacuum, a hexane (20 mL) solution of SiCl4 (3.40 g, 2.30 mL, 20.0 mol) was prepared. The Grignard reagent was cooled to room temperature and added dropwise to the hexane solution of SiCl4 using a dropping funnel to which the Grignard reagent was transferred via canula. The resulting mixture was stirred at room temperature for 16 h and filtered before the pale-yellow solution was concentrated under reduced pressure. The crude yellow oil was used for the next reaction of silicon complexation.

General Procedure for the synthesis of silicon complexes

To aryl trichlorosilane in dry THF (2 mL) was added triethylamine (0.15 mL, 0.80 mmol) under nitrogen atmosphere. The clouded solution was stirred at room temperature for 1 h before formazan ligand **L_H** or **L_Br** (0.20 mmol) in dry THF solution (10 mL) was added to the trichlorosilane solution. The solution turned blue-green and was stirred at room temperature for 16 h. The solvent was evaporated to dryness and the residue was dissolved by chloroform (50 mL), then washed with deionized water (3 × 50 mL) and dried over Mg_2SO_4, gravity filtered and concentrated *in vacuo*.

SiPhMe_H: The obtained solid was purified by column chromatography on silica gel (eluent : $CHCl_3$) to give **SiPhMe_H** as a black solid (0.046 g, 0.11 mmol, 57%). ^{1}H NMR (CD_2Cl_2, 400

MHz): δ 7.87–7.85 (dd, *J* = 8.2 Hz, 1.5 Hz, 2H, Ar-*H*), 7.52–7.47 (ddd, 8.3 Hz, 7.4 Hz, 1.5 Hz, 2H, Ar-*H*), 7.18–7.16 (dd, *J* = 8.3 Hz, 1.2 Hz, 2H, Ar-*H*), 7.14–7.06 (m, 6H, Ar-*H*), 2.25 (s, 3H, C*H*$_3$) ppm; ^{13}C{^{1}H} NMR ($CDCl_3$, 100 MHz): δ 152.2, 142.0, 134.8, 134.1, 133.2, 129.4, 128.1, 126.5, 122.5, 116.5, 116.3, 114.9, 21.5 ppm; ^{29}Si{^{1}H} NMR ($CDCl_3$, 79 MHz): δ –110.9 ppm. HRMS (DART): calcd. for $[C_{21}H_{15}N_5O_2Si+H]^+$ 398.1068, found 398.1070.

SiPhMe_Br: The obtained solid was purified by column chromatography on silica gel (eluent : $CHCl_3$) to give **SiPhMe_Br** as a black solid (0.033 g, 0.060 mmol, 30%). ^{1}H NMR (CD_2Cl_2, 400 MHz): δ 7.75–7.73 (d, *J* = 8.7 Hz, 2H, Ar-*H*), 7.37 (d, 1.9 Hz, 2H, Ar-*H*), 7.28–7.26 (dd, *J* = 8.7 Hz, 1.9 Hz, 2H, Ar-*H*), 7.09–7.08 (m, 4H, Ar-*H*), 2.26 (s, 3H, C*H*$_3$) ppm; ^{13}C{^{1}H} NMR ($CDCl_3$, 151 MHz): δ 152.3, 142.5, 133.8, 133.1, 129.6, 128.6, 128.3, 126.2, 125.8, 119.6, 117.5, 114.5, 21.6 ppm; ^{29}Si{^{1}H} NMR ($CDCl_3$, 119 MHz): δ –110.1 ppm. HRMS (DART): calcd. for $[C_{21}H_{13}Br_2N_5O_2Si+H]^+$ 553.9278, found 553.9274.

SiPhOMe_H: The obtained solid was purified by column chromatography on silica gel (eluent : $CHCl_3$) to give **SiPhOMe_H** as a black solid (0.048 g, 0.21 mmol, 58%). ^{1}H NMR (CD_2Cl_2, 400 MHz): δ 7.88–7.85 (dd, *J* = 8.0 Hz, 1.5 Hz, 2H, Ar-*H*), 7.51-7.47 (ddd, 8.3 Hz, 7.4 Hz, 1.4 Hz, 2H, Ar-*H*), 7.18-7.09 (m, 6H, Ar-*H*), 6.69-6.67 (d, 2H, Ar-*H*), 3.72 (s, 3H, OC*H*$_3$) ppm; ^{13}C{^{1}H} NMR ($CDCl_3$, 100 MHz): δ 162.3, 152.2, 135.0, 134.8, 134.1, 128.0, 122.5, 121.0, 116.5, 116.2, 114.9, 114.3, 55.1 ppm; ^{29}Si{^{1}H} NMR ($CDCl_3$, 79 MHz): δ –110.8 ppm. HRMS (DART): calcd. for $[C_{21}H_{15}N_5O_3Si+H]^+$ 414.1017, found 414.1023.

SiPhOMe_Br: The obtained solid was purified by column chromatography on silica gel (eluent : $CHCl_3$) to give **SiPhOMe_Br** as a black solid (0.054 g, 0.095 mmol, 47%). ^{1}H NMR (CD_2Cl_2, 400 MHz): δ 7.76–7.73 (d, *J* = 8.6 Hz, 2H, Ar-*H*), 7.37 (d, 1.8 Hz, 2H, Ar-*H*), 7.28–7.25 (dd, 8.6 Hz, 1.8 Hz, 2H, Ar-*H*), 7.14–7.12 (d, 8.8 Hz, 2H, Ar-*H*), 6.80–6.78 (d, 8.8 Hz, 2H, Ar-*H*), 3.73 (s, 3H, OC*H*$_3$) ppm; ^{13}C{^{1}H} NMR ($CDCl_3$, 151 MHz): δ 162.6, 152.2, 134.9, 133.8, 128.5, 128.3, 126.2, 120.3, 119.6, 117.5, 114.6, 114.5, 55.2 ppm; ^{29}Si{^{1}H} NMR ($CDCl_3$, 79 MHz): δ –109.9 ppm. HRMS (DART): calcd. for $[C_{21}H_{13}Br_2N_5O_3Si+H]^+$ 569.9227, found 569.9232.

SiPhNMe_H: The obtained solid was purified by column chromatography on silica gel (eluent : $CHCl_3$) to give **SiPhNMe_H** as a black solid (0.059 g, 0.14 mmol, 69%). ^{1}H NMR (CD_2Cl_2, 400 MHz): δ 7.87–7.85 (dd, *J* = 8.2 Hz, 1.4 Hz, 2H, Ar-*H*), 7.49–7.45 (ddd, *J* = 8.2 Hz, 7.4 Hz, 1.4 Hz, 2H, Ar-*H*), 7.17–7.14 (dd, *J* = 8.2 Hz, 1.1 Hz, 2H, Ar-*H*), 7.11–7.07 (ddd, *J* = 8.1 Hz, 7.3 Hz, 1.2 Hz, 2H, Ar-*H*), 7.06–7.04 (d, *J* = 8.9 Hz, 2H, Ar-*H*), 6.55–6.53 (d, *J* = 8.9 Hz, 2H, Ar-*H*), 2.88 (s, 6H, NC*H*$_3$) ppm; ^{13}C{^{1}H} NMR ($CDCl_3$, 100 MHz): δ 152.5, 152.2, 134.9, 134.7, 133.8, 127.9, 122.2, 116.4, 116.3, 115.2, 114.7, 111.8, 39.8 ppm; ^{29}Si{^{1}H} NMR ($CDCl_3$, 79 MHz): δ –109.5 ppm. HRMS (DART): calcd. for $[C_{22}H_{18}N_6O_2Si+H]^+$ 427.1333, found 427.1333.

SiPhNMe_Br: The obtained solid was purified by column chromatography on silica gel (eluent : $CHCl_3$) to give **SiPhNMe_Br** as a black solid (0.078 g, 0.13 mmol, 67%). ^{1}H NMR (CD_2Cl_2, 400 MHz): δ 7.75–7.73 (d, *J* = 8.6 Hz, 2H, Ar-*H*), 7.36 (d, *J* = 1.9 Hz, 2H, Ar-*H*), 7.26–7.24 (dd, *J* = 8.6 Hz, 1.9 Hz, 2H, Ar-*H*), 7.06–7.04 (d, *J* = 8.8 Hz, 2H, Ar-*H*), 6.63–6.61 (d, *J* = 8.8 Hz, 2H, Ar-*H*), 2.90 (s, 6H, NC*H*$_3$) ppm; ^{13}C{^{1}H} NMR ($CDCl_3$, 151 MHz): δ 152.6, 152.2, 134.6, 133.9, 128.1, 128.1, 125.9, 119.6, 117.4, 114.8, 113.9, 111.8, 39.8 ppm; ^{29}Si{^{1}H} NMR

($CDCl_3$, 119 MHz): δ –108.7 ppm. HRMS (DART): calcd. for $[C_{22}H_{16}Br_2N_6O_2Si+H]^+$ 582.9544, found 582.9542.

SiOH_H: The obtained solid was purified by reprecipitation into hexane/$CHCl_3$ to afford **SiOH_H** as a black solid (0.044 g, 0.14 mmol, 68%). ^{1}H NMR (CD_2Cl_2, 400 MHz): δ 7.75–7.73 (d, *J* = 8.3 Hz, 2H, Ar-*H*), 7.49–7.45 (dd, *J* = 7.8 Hz, 2H, Ar-*H*), 7.14–7.10 (dd, *J* = 7.8 Hz, 2H, Ar-*H*), 7.02–7.00 (d, *J* = 8.3 Hz, 2H, Ar-*H*) ppm; ^{13}C{^{1}H} NMR ($CDCl_3$, 151 MHz): δ 150.7, 134.2, 134.0, 127.7, 122.8, 116.2, 116.0, 114.6 ppm; ^{29}Si{^{1}H} NMR ($CDCl_3$, 79 MHz): δ –142.5 ppm. HRMS (DART): calcd. for $[C_{14}H_9N_5O_3Si+H]^+$ 324.0574, found 324.0547.

Synthesis of Polymers

Synthesis of pB_FL

Toluene (1.0 mL) was added to the mixture of **SiPh_Br** (0.027 g, 0.05 mmol), 2,7-bis(trimethylstannyl)-9,9-didodecylfluorene (41 mg, 50 μmol), $Pd_2(dba)_3$ (dba = dibenzylideneacetone) (1.4 mg, 1.5 μmol), and 2-dicyclohexylphosphino-2',4',6'-triisopropylbiphenyl (XPhos) (1.4 mg, 3.0 μmol). The reaction mixture was stirred at 80 °C for 22 h. After the reaction, the obtained polymer was redissolved in a small amount of $CHCl_3$, and then the product was reprecipitated in hexane. The polymer collected by filtration was dried *in vacuum* to give **pSi_FL** as a navy blue solid (35 mg, 69%). M_n = 7744, M_w/M_n = 1.34. ^{1}H NMR ($CDCl_3$, 600 MHz): δ 7.98–7.97 (d, 2H, *J* = 8.34 Hz, Ar-*H*), 7.84–7.83 (d, 2H, *J* = 8.34 Hz, Ar-*H*), 7.69–7.64 (m, 4H, Ar-*H*), 7.54–7.49 (m, 4H, Ar-*H*), 7.41–7.31 (m, 5H, Ar-*H*), 2.07 (br, 4H, -CH_2-), 1.23–1.07 (br, 40H, -CH_2-), 0.84 (t, 6H, *J* = 6.8 Hz, -CH_3) ppm; ^{13}C{^{1}H} NMR (CDCl3, 151 MHz): δ 152.4, 152.2, 151.7, 147.5, 141.2, 138.9, 134.2, 133.1, 131.6, 130.3, 128.6, 128.3, 126.4, 122.0, 121.4, 120.6, 116.8, 115.1, 114,0, 55.5, 40.4, 31.9, 30.0, 29.6, 29.5, 29.3, 29.3, 23.9, 22.7, 14.1 ppm; ^{29}Si{^{1}H} NMR ($CDCl_3$,119 MHz): δ –110.5 ppm.

Synthesis of pSi_BT

Toluene (1.0 mL) was added to the mixture of **SiPh_Br** (27 mg, 50 μmol), 5,5'-bis(trimethylstannyl)-3,3'-didodecyl-2,2'-bithiophene (41 mg, 50 μmol), $Pd_2(dba)_3$ (dba = dibenzylideneacetone) (1.4 mg, 1.5 μmol), and 2-dicyclohexylphosphino-2',4',6'-triisopropylbiphenyl (XPhos) (1.4 mg, 3.0 μmol). The reaction mixture was stirred at 80 °C for 22 h. After the reaction, the obtained polymer was redissolved in a small amount of $CHCl_3$, and then the product was reprecipitated in hexane. The polymer collected by filtration was dried *in vacuo*

to give **pSi_BT** as a navy blue solid (20 mg, 44%). M_n = 8079, M_w/M_n = 1.34. ^{1}H NMR ($CDCl_3$, 400 MHz): δ 7.87–7.85 (d, 4H, *J* = 8.5 Hz, Ar-*H*), 7.41–7.27 (m, 11H, Ar-*H*), 2.62 (br, 4H, -CH_2-), 1.23 (br, 40H, -CH_2-), 0.86 (t, 6H, *J* = 6.8 Hz, -CH_3) ppm; ^{13}C{^{1}H} NMR (CDCl3, 151 MHz): δ 152.4, 152.3, 144.5, 142.9, 139.5, 134.4, 133.0, 131.5, 130.8, 130.3, 128.6, 128.3, 127.1, 120.4, 117.0, 115.1, 111.7, 31.9, 30. 7, 29.7, 29.6, 29.6, 29.5, 29.4, 29.3, 29.2, 22.7, 14.1 ppm; ^{29}Si{^{1}H} NMR ($CDCl_3$,119 MHz): δ –110.4 ppm.

Photophysical Properties

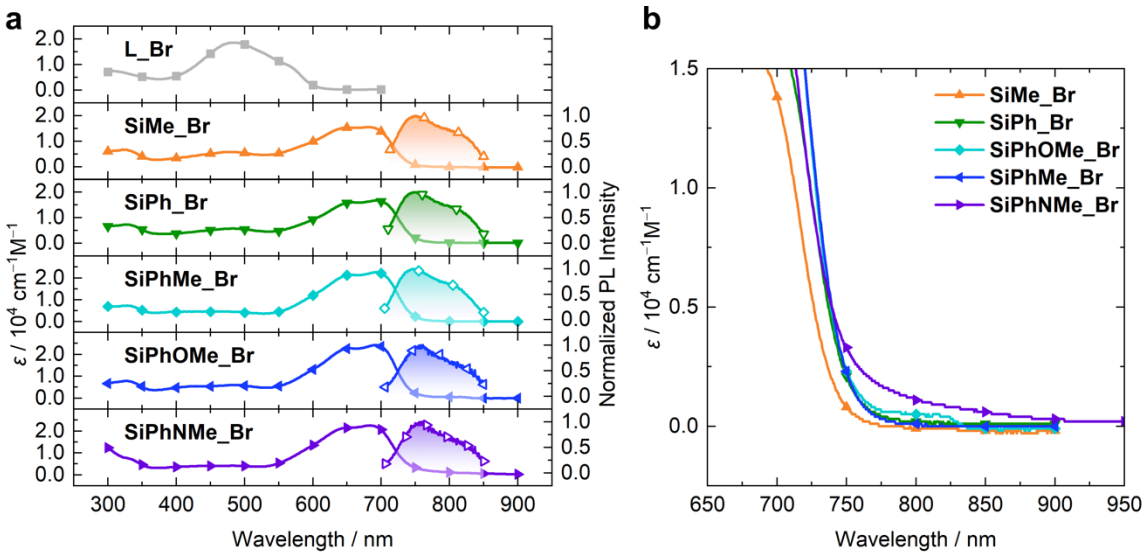

Figure S1. (a) UV–vis absorption and normalized photoluminescence spectra of $CHCl_3$ solutions (1.0×10^{-5} M) of dibrominated silicon formazanate complexes and proligand **L_Br**. (b) Absorption edge of the complexes.

Density Functional Theory Calculations

Density functional theory (DFT) and time-dependent (TD) DFT calculations were performed at the B3LYP/6-31+G(d,p) level of theory using the polarizable continuum model for treating solvent effect of toluene. Geometry optimizations were performed for S_0 states, followed by frequency calculation at the same level. TD-DFT calculations were carried out with S_0-optimized structures.

Structural parameters of each S_0 geometry were shown in Table S@. For example, Addison's parameter τ was calculated for each structure.[1] This parameter becomes 0 and 1 for a perfect square-pyramidal and a perfect trigonal-bipyramidal geometries, respectively. Since all complexes possessed 0–0.2 of τ, they were optimized to square-pyramidal structures rather than trigonal-bipyramidal structures.

Table S1. Structural parameters for the optimized structures of silicon formazanate complexes

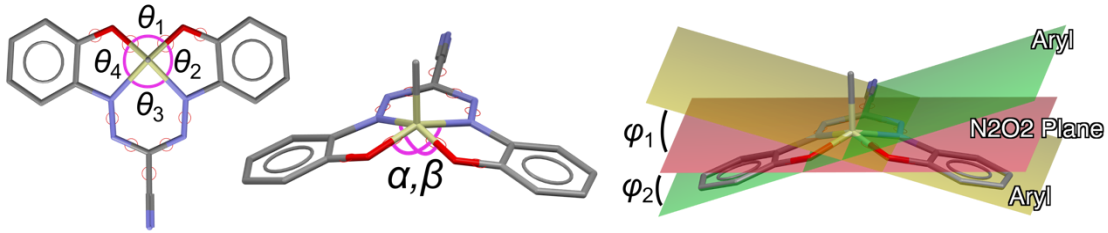

	θ_1 / deg	θ_2 / deg	θ_3 / deg	θ_4 / deg	$\Sigma\theta$ / deg	φ_1 / deg	φ_2 / deg	$\varphi_{average}$ / deg	d / Å[a]	α / deg	β (> α) /deg	$\tau = (\beta - \alpha) / 60$[b]
SiOH_H	88.91	86.19	85.60	85.60	346.29	12.74	18.04	15.39	0.459	145.00	156.38	0.195
SiMe_H	89.03	84.90	83.44	84.91	342.28	17.19	17.34	17.27	0.508	147.51	147.69	0.003
SiPh_H	88.65	85.15	83.73	84.94	342.47	15.38	18.31	16.85	0.507	144.79	150.57	0.096
SiPhMe_H	88.60	85.17	83.68	84.87	342.32	15.29	18.62	16.96	0.510	144.17	150.80	0.111
SiPhOMe_H	88.51	85.20	83.66	84.78	342.15	15.01	18.97	16.99	0.513	143.34	151.19	0.131
SiPhNMe_H	88.29	85.16	83.59	84.63	341.67	15.01	19.20	17.11	0.521	142.45	151.12	0.145
SiMe_Br	88.83	84.89	83.43	84.89	342.04	17.25	17.26	17.26	0.512	147.39	147.41	0.000
SiPh_Br	88.40	84.90	83.73	85.15	342.18	15.34	18.45	16.90	0.512	144.30	150.51	0.104
SiPhMe_Br	88.37	84.85	83.68	85.13	342.03	15.18	18.49	16.84	0.514	143.91	150.54	0.111
SiPhOMe_Br	88.26	85.19	83.67	84.76	341.88	15.01	18.93	16.97	0.518	143.04	150.98	0.132
SiPhNMe_Br	88.01	85.14	83.61	84.63	341.39	14.93	19.05	16.99	0.526	142.21	150.86	0.144

[a]Distance between a N2O2 plane and a silicon atom. [b]Addison's structural parameter. τ is 0 and 1 for a perfect square-pyramidal and a perfect trigonal-bipyramidal geometries, respectively.[1]

Calculated Optical Properties

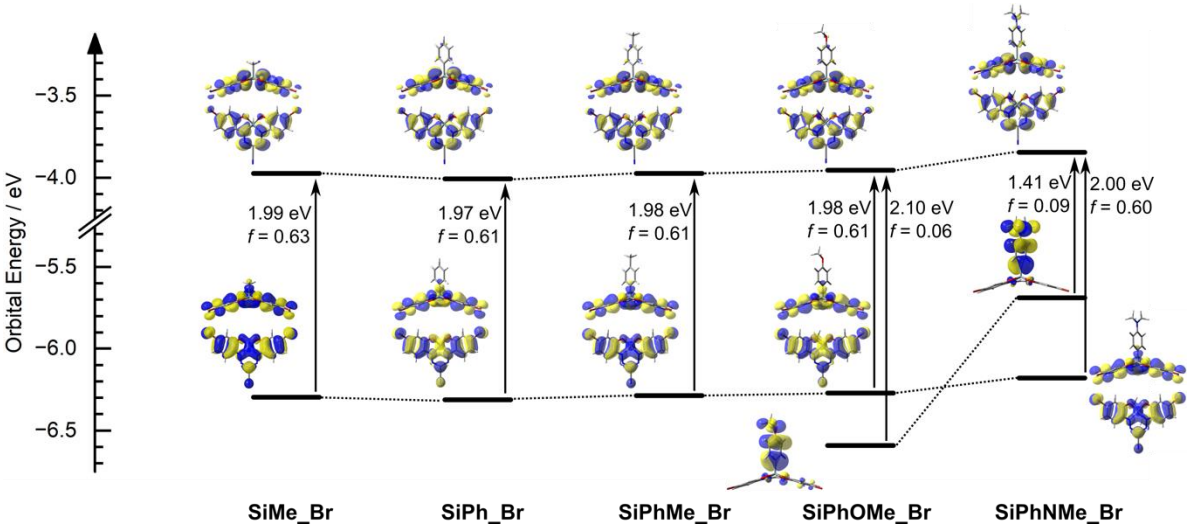

Figure S2. Frontier orbital energy diagram of **SiR_Br**. Kohn–Sham molecular orbitals were illustrated with 0.02 of isovalue. Both of front and side views were shown, except for the HOMO–1 of **SiPhOMe_Br** and the HOMO of **SiPhNMe_Br**. Electronic transition energies were listed with the corresponding oscillator strengths (*f*).

Natural Bond Orbital Analysis

To obtain deep insight into effects of an axial ligand on photophysical properties, we performed natural bond orbital (NBO) analysis for **SiOH_H** and **SiMe_H**. NBOs 87 and 41 show significant contributions in the HOMOs of **SiOH_H** and **SiMe_H**, respectively. NBO 87 of **SiOH_H** is composed mainly of the lone pair (LP) orbital of the oxygen atom O23, while NBO 41 of **SiMe_H** is mainly of the bonding (BD) orbital of the Si22–C23, as illustrated in Figures S3 and S4. The 2pz natural atomic orbital (NAO) of O23 and C23 possesses the main contribution to NBO 87 of **SiOH_H** and NBO 41 of **SiMe_H**, respectively (Tables S2 and S3). The NBO calculations revealed that the energy of the 2pz NAO of O23 of **SiOH_H** (–10.47 eV) is significantly lower than that of the 2pz NAO of C23 of **SiMe_H** (–5.16 eV). This lower-lying valence orbital of the oxygen atom is consistent with the electronegative nature of oxygen. Consequently, the resulting HOMO of **SiOH_H** (–6.36 eV) is also more stable than that of **SiMe_H** (–6.18 eV). It should be noted that the LUMOs of both compounds show no contributions from each axial ligand because the axial ligand is located on the nodal plane of LUMO. Therefore, these LUMO levels are less efficiently stabilized by the electronegative oxygen than the HOMOs.

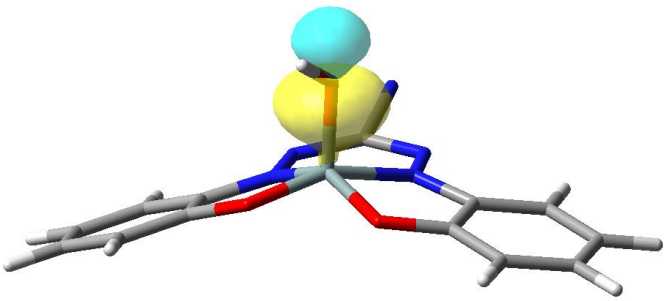

Figure S3. Illustration of NBO 87 of **SiOH_H**. Occupancy, 1.71089; orbital type, LP(3); hybridization, $sp^{1.83}d^{0.00}$ (s, 35.34%; p, 64.52%; d, 0.14%).

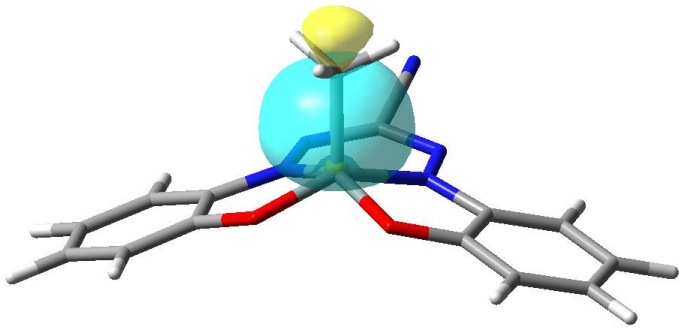

Figure S4. Illustration of NBO 41 of **SiMe_H**. Occupancy, 1.98411; type, BD(1). Composition: (28.18%) 0.5308*Si22 (hybridization, $sp^{0.76}d^{0.02}$ (s, 56.35%; p, 42.75%; d, 0.90%)) and (71.82%) 0.8475*C23 (hybridization, $sp^{2.55}d^{0.00}$ (s, 28.16%; p, 71.80%; d, 0.04%)).

Table S2. Contributions from the natural atomic orbitals of oxygen atom O23 to NBO 87 of **SiOH_H**

	Type(AO)	occupancy	Energy / hartree	Energy / eV	Coeff. for NBO87
S	Cor(1S)	1.99983	-18.99428	-516.85	-0.0005
S	Val(2S)	1.74686	-0.97128	-26.43	0.5944
S	Ryd(4S)	0.00092	1.83941	50.05	0.0069
S	Ryd(3S)	0.00011	1.13382	30.85	-0.0005
S	Ryd(5S)	0.00001	4.16339	113.29	-0.0004
px	Val(2p)	1.87837	-0.33633	-9.15	-0.0249
px	Ryd(3p)	0.00149	0.74653	20.31	0
px	Ryd(4p)	0.00019	0.86008	23.40	0.0005
py	Val(2p)	1.79356	-0.34063	-9.27	-0.0824
py	Ryd(3p)	0.00104	0.82338	22.40	-0.0004
py	Ryd(4p)	0.00032	0.97131	26.43	0.0004
pz	Val(2p)	1.70354	-0.38473	-10.47	-0.7986
pz	Ryd(3p)	0.00292	0.72878	19.83	-0.0002
pz	Ryd(4p)	0.00063	1.00581	27.37	0.0011
dxy	Ryd(3d)	0.00149	2.0805	56.61	0.0043
dxz	Ryd(3d)	0.00092	2.06875	56.29	0.0092
dyz	Ryd(3d)	0.00179	2.31421	62.97	0.02
dx2y2	Ryd(3d)	0.00141	1.96689	53.52	-0.0034
dz2	Ryd(3d)	0.00194	2.27706	61.96	0.0301

Table S3. Contributions from the natural atomic orbitals of oxygen atom C23 to NBO 41 of **SiMe_H**

	Type(AO)	occupancy	Energy / hartree	Energy / eV	Coeff. for NBO41
S	Cor(1S)	1.99945	-10.05272	-273.54	-0.0001
S	Val(2S)	1.23345	-0.36204	-9.85	-0.5299
S	Ryd(4S)	0.00301	1.12262	30.55	-0.0291
S	Ryd(3S)	0.00010	0.68102	18.53	0.0011
S	Ryd(5S)	0.00001	4.40738	119.93	0.0011
px	Val(2p)	1.29462	-0.11866	-3.23	0.0039
px	Ryd(4p)	0.00227	0.60285	16.40	0
px	Ryd(3p)	0.00012	0.55098	14.99	-0.0001
py	Val(2p)	1.30193	-0.12213	-3.32	0.0949
py	Ryd(4p)	0.00062	0.61638	16.77	-0.0046
py	Ryd(3p)	0.00011	0.47461	12.91	0.0035
pz	Val(2p)	1.42779	-0.18979	-5.16	0.8414
pz	Ryd(4p)	0.00342	0.61795	16.81	-0.0302
pz	Ryd(3p)	0.00037	0.34571	9.41	-0.0028
dxy	Ryd(3d)	0.00068	2.42258	65.92	0
dxz	Ryd(3d)	0.00016	2.09911	57.12	-0.0002
dyz	Ryd(3d)	0.00035	2.22082	60.43	-0.0044
dx2y2	Ryd(3d)	0.00051	2.30739	62.79	0.0002
dz2	Ryd(3d)	0.00087	2.24694	61.14	-0.0194

Table S4. Optimized geometry of **SiOH_H**

Center Number	Atomic Number	Atomic Type	Coordinates (Angstroms)		
			x	y	z
1	7	0	-1.266966	0.587704	0.017332
2	7	0	-1.182424	1.887855	-0.056341
3	6	0	0.02093	2.462208	0.05347
4	7	0	1.240356	1.900201	0.019948
5	7	0	1.309761	0.604394	0.096457
6	6	0	2.531981	-0.011158	-0.167437
7	6	0	-2.508716	-0.002905	-0.235728
8	6	0	3.756828	0.591384	-0.477712
9	6	0	4.843507	-0.235818	-0.729732
10	6	0	4.702208	-1.635416	-0.687565
11	6	0	3.479674	-2.235829	-0.39185
12	6	0	2.388084	-1.411122	-0.123064
13	6	0	-2.450948	-1.386331	0.017374
14	6	0	-3.582436	-2.179064	-0.170912
15	6	0	-4.755827	-1.56276	-0.60398
16	6	0	-4.810388	-0.179875	-0.853712
17	6	0	-3.683978	0.614617	-0.675333
18	8	0	-1.25539	-1.859339	0.422596
19	8	0	1.150096	-1.867491	0.157732
20	14	0	-0.004688	-0.681311	0.638698
21	8	0	0.103069	-0.388016	2.260139
22	6	0	0.012297	3.902279	0.050633
23	7	0	0.005387	5.064145	0.063841
24	1	0	3.835113	1.671683	-0.510719
25	1	0	5.808968	0.200184	-0.963171
26	1	0	5.564268	-2.263224	-0.890321
27	1	0	3.362057	-3.313081	-0.362517
28	1	0	-3.532297	-3.244844	0.021324
29	1	0	-5.646099	-2.165998	-0.752226
30	1	0	-5.738231	0.270288	-1.190124
31	1	0	-3.697405	1.682125	-0.86122
32	1	0	-0.275026	-1.071362	2.8281

Low Frequencies:					
-3.2495	-2.031	-0.0003	0.0001	0.0014	3.3273
31.3576	51.8994	69.6424			

Table S5. Optimized geometry of **SiMe_H**

Center Number	Atomic Number	Atomic Type	Coordinates (Angstroms)		
			x	y	z
1	1	0	0.921043	0.070578	2.90893
2	1	0	-0.046885	-1.402622	3.075356
3	1	0	-0.848012	0.167468	2.906641
4	1	0	-3.730528	1.67193	-0.810266
5	1	0	-5.722588	0.223753	-1.257582
6	1	0	-5.56804	-2.22919	-0.945604
7	1	0	-3.440368	-3.287164	-0.182382
8	1	0	3.437275	-3.287893	-0.188389
9	1	0	5.566352	-2.230126	-0.947962
10	1	0	5.723009	0.223284	-1.255206
11	1	0	3.731733	1.672145	-0.80663
12	7	0	-0.000541	5.069671	0.067228
13	6	0	-0.000494	3.907458	0.049473
14	6	0	0.006792	-0.430442	2.576028
15	14	0	-0.000102	-0.687937	0.727219
16	8	0	1.216805	-1.867557	0.345872
17	8	0	-1.21924	-1.867182	0.351062
18	6	0	-3.691582	0.59733	-0.67537
19	6	0	-4.789802	-0.217128	-0.922455
20	6	0	-4.69958	-1.609571	-0.744527
21	6	0	-3.518603	-2.214236	-0.3167
22	6	0	-2.416161	-1.401336	-0.052138
23	6	0	2.414466	-1.401538	-0.05517
24	6	0	3.516469	-2.214768	-0.320554
25	6	0	4.698216	-1.610221	-0.746376
26	6	0	4.789633	-0.217509	-0.921612
27	6	0	3.691879	0.597322	-0.673772
28	6	0	-2.509632	-0.007517	-0.232519
29	6	0	2.509149	-0.007412	-0.23279
30	7	0	1.291198	0.60306	0.069936
31	7	0	1.211403	1.89701	-0.030626
32	6	0	-0.000209	2.468757	0.056153
33	7	0	-1.211446	1.896591	-0.030711
34	7	0	-1.291376	0.602485	0.069966

Low Frequencies:					
-5.3807	-2.6255	0.0004	0.0015	0.0017	6.9464
31.0288	36.7618	52.3786			

Table S6. Optimized geometry of **SiPh_H**

Center Number	Atomic Number	Atomic Type	Coordinates (Angstroms)		
			x	y	z
1	6	0	-0.114666	-1.842533	1.828297
2	7	0	-1.305292	-1.578256	1.267682
3	7	0	-1.330346	-0.82892	0.203522
4	6	0	-2.523424	-0.74552	-0.515304
5	6	0	2.497025	-0.904119	-0.368012
6	6	0	-3.748653	-1.359395	-0.22986
7	6	0	-4.80619	-1.143866	-1.104413
8	6	0	-4.634143	-0.345263	-2.24994
9	6	0	-3.409876	0.252706	-2.543527
10	6	0	-2.347438	0.053202	-1.661921
11	6	0	2.478113	-0.018211	-1.461967
12	6	0	3.619915	0.147434	-2.245557
13	6	0	4.765264	-0.571491	-1.906145
14	6	0	4.781333	-1.454046	-0.811142
15	6	0	3.643324	-1.634044	-0.034434
16	8	0	1.308637	0.606851	-1.696138
17	8	0	-1.112501	0.557205	-1.84754
18	14	0	0.026793	0.325555	-0.558632
19	6	0	-0.169318	-2.583851	3.060394
20	7	0	-0.214574	-3.163906	4.066534
21	6	0	0.011603	1.803225	0.583497
22	6	0	-0.765826	1.856076	1.756401
23	6	0	-0.752535	2.981893	2.580371
24	6	0	0.039397	4.081999	2.248297
25	6	0	0.816426	4.052594	1.088716
26	6	0	0.802805	2.925944	0.26709
27	1	0	-3.850761	-1.976184	0.655332
28	1	0	-5.771353	-1.596687	-0.903923
29	1	0	-5.472688	-0.19122	-2.921967
30	1	0	-3.267778	0.864118	-3.427382
31	7	0	1.114881	-1.66818	1.320573
32	7	0	1.250369	-0.925446	0.261541
33	1	0	3.598964	0.825616	-3.091169
34	1	0	5.663725	-0.44691	-2.502636
35	1	0	5.687931	-1.999788	-0.572444
36	1	0	3.625373	-2.310615	0.811922
37	1	0	-1.395668	1.017253	2.036386
38	1	0	-1.359929	2.998885	3.480468
39	1	0	0.050219	4.958539	2.889626
40	1	0	1.43294	4.906734	0.824141
41	1	0	1.410745	2.916574	-0.632098

Low Frequencies:					
-4.924	-2.6677	-0.0009	-0.0003	0.0004	3.9168
19.6707	32.8517	34.7763			

Table S7. Optimized geometry of **SiPhMe_H**

Center Number	Atomic Number	Atomic Type	Coordinates (Angstroms)		
			x	y	z
1	7	0	1.245833	-0.975146	0.612054
2	7	0	1.110122	-1.184502	1.888722
3	6	0	-0.118249	-1.114841	2.423347
4	7	0	-1.31003	-1.11376	1.805127
5	7	0	-1.334135	-0.899814	0.521573
6	6	0	-2.526836	-1.133972	-0.163232
7	6	0	2.491638	-1.233474	0.035259
8	6	0	-3.754782	-1.556371	0.359546
9	6	0	-4.811267	-1.741527	-0.523189
10	6	0	-4.635464	-1.526062	-1.902437
11	1	0	0.210301	6.495553	-0.384633
12	1	0	0.901142	6.156603	1.202293
13	1	0	-0.851034	6.246734	1.013854
14	1	0	1.391506	2.120829	-1.867568
15	1	0	1.405305	4.535679	-1.421334
16	1	0	-1.35462	3.962	1.817053
17	1	0	-1.38598	1.559123	1.382117
18	1	0	3.613616	-2.00457	1.705544
19	1	0	5.676214	-2.328817	0.324451
20	1	0	5.658566	-1.752481	-2.085064
21	1	0	3.600435	-0.843052	-3.164637
22	1	0	-3.263555	-0.960191	-3.487782
23	1	0	-5.473192	-1.678633	-2.575844
24	1	0	-5.778461	-2.056973	-0.146568
25	1	0	-3.859507	-1.722996	1.425257
26	7	0	-0.215718	-1.334179	5.013348
27	6	0	-0.171616	-1.248178	3.855096
28	6	0	0.070136	5.911076	0.529414
29	6	0	0.789342	2.511735	-1.053268
30	6	0	0.797677	3.881286	-0.801183
31	6	0	0.033599	4.430892	0.237713
32	6	0	-0.746677	3.561019	1.010061
33	6	0	-0.758385	2.18991	0.759878
34	6	0	0.010766	1.62965	-0.27733
35	14	0	0.026956	-0.193301	-0.666503
36	8	0	-1.110085	-0.551952	-1.928814
37	8	0	1.31055	-0.430237	-1.813735
38	6	0	3.634246	-1.756213	0.650894
39	6	0	4.772482	-1.932898	-0.126414
40	6	0	4.760125	-1.604527	-1.493884
41	6	0	3.618414	-1.09389	-2.11004
42	6	0	2.476268	-0.901524	-1.332882
43	6	0	-2.346972	-0.919014	-1.543582
44	6	0	-3.408502	-1.121956	-2.425676

Low Frequencies:					
-0.5609	-0.0005	0.0011	0.0018	2.8336	5.2022
23.002	27.8876	35.0896			

Table S8. Optimized geometry of **SiPhOMe_H**

Center Number	Atomic Number	Atomic Type	Coordinates (Angstroms)		
			x	y	z
1	7	0	0.382502	1.697702	0.58673
2	7	0	0.672422	1.720948	1.855069
3	6	0	1.295939	0.6614	2.391161
4	7	0	1.920088	-0.354432	1.773065
5	7	0	1.712492	-0.514002	0.498289
6	6	0	2.534811	-1.399774	-0.197876
7	6	0	-0.096943	2.873975	0.004517
8	6	0	3.566938	-2.199775	0.306723
9	6	0	4.270597	-2.99796	-0.586175
10	6	0	3.959188	-2.980417	-1.958219
11	6	0	2.943257	-2.171395	-2.463818
12	6	0	2.221565	-1.378529	-1.57108
13	6	0	-0.418439	2.655332	-1.348647
14	6	0	-0.905211	3.704962	-2.127791
15	6	0	-1.071944	4.952842	-1.528529
16	6	0	-0.751687	5.166781	-0.176042
17	6	0	-0.254222	4.128816	0.602809
18	8	0	-0.200801	1.411437	-1.814338
19	8	0	1.235314	-0.539747	-1.940153
20	14	0	0.343157	0.227369	-0.662446
21	6	0	-1.157214	-0.775814	-0.214239
22	6	0	-1.18542	-1.701803	0.851813
23	6	0	-2.32356	-2.437243	1.147854
24	6	0	-3.487599	-2.27366	0.380224
25	6	0	-3.49065	-1.364199	-0.685772
26	6	0	-2.33714	-0.632749	-0.967442
27	6	0	1.483289	0.717764	3.816774
28	7	0	1.618004	0.751052	4.97075
29	8	0	-4.549373	-3.03823	0.747873
30	6	0	-5.761281	-2.919861	0.008321
31	1	0	3.791186	-2.187228	1.366933
32	1	0	5.067841	-3.637923	-0.223314
33	1	0	4.522733	-3.60999	-2.63984
34	1	0	2.701759	-2.147582	-3.520402
35	1	0	-1.145348	3.534252	-3.171202
36	1	0	-1.456372	5.777024	-2.121465
37	1	0	-0.891654	6.1493	0.261977
38	1	0	0.005087	4.26575	1.646079
39	1	0	-0.303411	-1.861757	1.46418
40	1	0	-2.338029	-3.146456	1.968855
41	1	0	-4.374839	-1.220017	-1.294793
42	1	0	-2.359995	0.066426	-1.797522
43	1	0	-6.46281	-3.613501	0.472354
44	1	0	-6.16706	-1.902956	0.063269
45	1	0	-5.618597	-3.197223	-1.042626

Low Frequencies:					
-2.9743	0.0014	0.0015	0.0016	1.6101	2.544
20.5467	25.5957	37.1527			

Table S9. Optimized geometry of **SiPhNMe_H**

Center Number	Atomic Number	Atomic Type	Coordinates (Angstroms)		
			x	y	z
1	1	0	-5.774736	-1.761222	1.091601
2	1	0	-1.177988	-1.310386	1.322277
3	1	0	-3.564984	-1.275053	1.631231
4	7	0	1.315616	-1.364869	0.524705
5	1	0	-5.591937	-0.388104	2.203278
6	1	0	-7.039274	-0.527175	1.197089
7	1	0	-6.101478	0.51193	-1.790698
8	1	0	-7.229529	0.759069	-0.449457
9	1	0	-5.937363	1.93162	-0.735912
10	1	0	-3.952843	1.406786	-1.742068
11	1	0	-1.548883	1.368082	-2.031897
12	1	0	2.021359	-3.93319	1.406191
13	1	0	2.423781	-5.813468	-0.196209
14	1	0	2.219468	-5.430268	-2.635546
15	1	0	1.609255	-3.180065	-3.526593
16	1	0	1.522477	3.667677	-3.037794
17	1	0	2.424387	5.67642	-1.863316
18	1	0	2.893586	5.617057	0.569019
19	1	0	2.466667	3.52476	1.876216
20	7	0	1.540704	-0.351877	5.055841
21	6	0	1.516057	-0.281793	3.895801
22	6	0	-6.188317	0.863298	-0.753892
23	6	0	-5.961229	-0.685842	1.213676
24	7	0	-5.346818	0.097187	0.152459
25	6	0	-1.766412	-0.700106	0.643397
26	6	0	-3.141705	-0.687866	0.826008
27	6	0	-3.982731	0.074006	-0.022977
28	6	0	-3.358196	0.810846	-1.060945
29	6	0	-1.981362	0.785163	-1.224183
30	6	0	-1.133912	0.033683	-0.381468
31	14	0	0.69496	0.040459	-0.66648
32	8	0	1.00546	1.351576	-1.770704
33	8	0	1.138612	-1.064126	-1.935332
34	6	0	1.929554	-3.794525	0.335254
35	6	0	2.153928	-4.829204	-0.564169
36	6	0	2.037301	-4.609234	-1.948972
37	6	0	1.69444	-3.359153	-2.460727
38	6	0	1.452614	-2.318313	-1.563171
39	6	0	1.478177	2.492362	-1.238008
40	6	0	1.727084	3.651805	-1.973156
41	6	0	2.232527	4.765791	-1.304123
42	6	0	2.500044	4.734478	0.07598
43	6	0	2.266176	3.579185	0.812569
44	6	0	1.56791	-2.542923	-0.177047
45	6	0	1.749607	2.464549	0.143488
46	7	0	1.441919	1.209183	0.674621
47	7	0	1.581642	1.041578	1.958088
48	6	0	1.458601	-0.196008	2.460503
49	7	0	1.46052	-1.375728	1.818368

Low Frequencies:					
-0.001	-0.0007	0.0007	2.314	3.5081	3.9127
19.8143	21.7351	29.9604			

Table S10. Optimized geometry of **SiMe_Br**

Center Number	Atomic Number	Atomic Type	Coordinates (Angstroms)		
			x	y	z
1	7	0	-1.290255	1.435619	0.139848
2	7	0	-1.21106	2.691869	-0.189487
3	6	0	-0.000014	3.270122	-0.206191
4	7	0	1.211033	2.69184	-0.189562
5	7	0	1.290222	1.435572	0.139768
6	6	0	2.50627	0.781652	-0.050302
7	6	0	-2.506314	0.781692	-0.050197
8	6	0	3.689785	1.294794	-0.590475
9	6	0	4.791081	0.455206	-0.693918
10	6	0	4.683704	-0.879854	-0.271497
11	6	0	3.509794	-1.411644	0.256006
12	6	0	2.411931	-0.559596	0.370603
13	6	0	-2.411888	-0.55962	0.370475
14	6	0	-3.509716	-1.411695	0.255819
15	6	0	-4.683698	-0.879862	-0.271494
16	6	0	-4.791164	0.455261	-0.693672
17	6	0	-3.68989	1.294879	-0.590182
18	8	0	-1.217689	-0.947871	0.846649
19	8	0	1.217806	-0.947803	0.846952
20	14	0	-0.000012	0.283377	1.015628
21	35	0	-6.212157	-2.010423	-0.429181
22	35	0	6.212204	-2.01037	-0.429122
23	6	0	0.000007	4.684987	-0.468079
24	7	0	0.000017	5.831649	-0.65714
25	6	0	-0.000133	0.854163	2.791159
26	1	0	3.735959	2.328271	-0.912907
27	1	0	5.726567	0.821094	-1.098483
28	1	0	3.438914	-2.444264	0.572916
29	1	0	-3.438768	-2.44437	0.572537
30	1	0	-5.726701	0.821191	-1.098083
31	1	0	-3.736133	2.328407	-0.91244
32	1	0	-0.886031	1.452999	3.023701
33	1	0	0.000087	-0.01964	3.449776
34	1	0	0.8855	1.4534	3.023687

Low Frequencies:					
-2.6308	-1.8663	-0.0075	-0.0031	0.0026	2.1147
18.5524	42.1903	51.6706			

Table S11. Optimized geometry of **SiPh_Br**

Center Number	Atomic Number	Atomic Type	Coordinates (Angstroms)		
			x	y	z
1	1	0	0.00582	4.048799	4.744098
2	1	0	-1.314311	4.554764	2.700062
3	1	0	-1.340805	2.980163	0.820632
4	1	0	-3.805875	1.431409	-2.099575
5	1	0	-5.774483	-0.047056	-1.645932
6	1	0	-3.382693	-2.450016	1.036227
7	1	0	3.488839	-2.296981	1.12573
8	1	0	5.70107	-0.063412	-1.841557
9	1	0	3.685794	1.350488	-2.2989
10	6	0	0.724011	1.26709	2.922058
11	6	0	0.731688	2.16335	3.990166
12	6	0	-0.000538	3.349616	3.913025
13	6	0	-0.742045	3.634195	2.765445
14	6	0	-0.750206	2.735796	1.698234
15	6	0	-0.016925	1.534698	1.753138
16	7	0	-0.043623	4.637443	-3.481578
17	6	0	-0.038644	3.678963	-2.824565
18	35	0	6.243256	-2.312348	-0.010962
19	35	0	-6.19184	-2.431228	0.039035
20	14	0	-0.001079	0.294228	0.360079
21	8	0	1.243025	-0.857198	0.753544
22	8	0	-1.17904	-0.950344	0.656877
23	6	0	-3.73271	0.592258	-1.417943
24	6	0	-4.821299	-0.23186	-1.166341
25	6	0	-4.678882	-1.315256	-0.283473
26	6	0	-3.48131	-1.607828	0.363416
27	6	0	-2.395821	-0.767777	0.117962
28	6	0	2.425864	-0.703479	0.136129
29	6	0	3.537604	-1.505976	0.388344
30	6	0	4.696786	-1.244395	-0.337941
31	1	0	1.308512	1.936004	4.881799
32	1	0	1.296659	0.34798	2.995805
33	6	0	4.776149	-0.227211	-1.302699
34	6	0	3.660897	0.560035	-1.558204
35	6	0	-2.526056	0.323423	-0.763565
36	6	0	2.491824	0.318508	-0.830405
37	7	0	1.266359	0.978343	-0.924745
38	7	0	1.175944	1.980197	-1.750694
39	6	0	-0.034013	2.507117	-1.989209
40	7	0	-1.245175	2.003522	-1.705132
41	7	0	-1.313949	1.001433	-0.875974

Low Frequencies:					
-2.8849	0.0081	0.0088	0.0103	0.8403	3.5607
15.065	27.477	32.3263			

Table S12. Optimized geometry of **SiPhMe_Br**

Center Number	Atomic Number	Atomic Type	Coordinates (Angstroms)		
			x	y	z
1	7	0	1.316223	0.42867	1.278167
2	7	0	1.247258	1.05114	2.419951
3	6	0	0.035336	1.410519	2.871314
4	7	0	-1.174053	1.007437	2.454839
5	7	0	-1.263945	0.383091	1.316342
6	6	0	-2.489549	-0.194703	0.984142
7	6	0	2.52882	-0.157721	0.921515
8	6	0	-3.658073	-0.241132	1.750223
9	6	0	-4.773745	-0.877206	1.221273
10	6	0	-4.69512	-1.462738	-0.052463
11	6	0	-3.536558	-1.435294	-0.824836
12	6	0	-2.424313	-0.783954	-0.293228
13	6	0	2.397248	-0.848905	-0.2991
14	6	0	3.483274	-1.537347	-0.838619
15	6	0	4.682447	-1.500129	-0.132364
16	6	0	4.826225	-0.81665	1.086456
17	6	0	3.737173	-0.145334	1.625873
18	8	0	1.17919	-0.823747	-0.864451
19	8	0	-1.242364	-0.696679	-0.92443
20	14	0	0.002277	0.227685	-0.132797
21	6	0	0.016559	1.893405	-0.964344
22	35	0	6.195952	-2.416039	-0.846183
23	35	0	-6.242114	-2.333144	-0.751907
24	6	0	0.740998	2.994729	-0.470523
25	6	0	0.729841	4.222135	-1.130525
26	6	0	-0.004728	4.403127	-2.309425
27	6	0	-0.723511	3.308831	-2.810977
28	6	0	-0.716119	2.081367	-2.153902
29	6	0	-0.041402	5.740711	-3.006772
30	6	0	0.038855	2.188791	4.08181
31	7	0	0.042878	2.835239	5.047501
32	1	0	-3.682343	0.217478	2.731623
33	1	0	-5.698251	-0.925457	1.783074
34	1	0	-3.488366	-1.89531	-1.803547
35	1	0	3.383695	-2.073537	-1.77365
36	1	0	5.780662	-0.818472	1.598079
37	1	0	3.811285	0.384709	2.568052
38	1	0	1.332698	2.90367	0.435357
39	1	0	1.302348	5.052085	-0.724518
40	1	0	-1.294539	3.420303	-3.729294
41	1	0	-1.282473	1.25522	-2.5724
42	1	0	-0.910943	6.326025	-2.683004
43	1	0	0.850908	6.332638	-2.785289
44	1	0	-0.115962	5.623834	-4.091885

Low Frequencies:					
-4.5908	-3.3076	0.0025	0.0067	0.0067	0.8852
14.1441	21.5617	27.14			

Table S13. Optimized geometry of **SiPhOMe_Br**

Center Number	Atomic Number	Atomic Type	Coordinates (Angstroms)		
			x	y	z
1	7	0	-1.343856	-0.072162	1.413405
2	7	0	-1.276262	0.231722	2.677817
3	6	0	-0.061778	0.437399	3.212071
4	7	0	1.143862	0.133271	2.710314
5	7	0	1.234149	-0.175887	1.448686
6	6	0	2.454762	-0.667565	0.984124
7	6	0	-2.560037	-0.528901	0.910768
8	6	0	3.612924	-0.936394	1.719217
9	6	0	4.725563	-1.429093	1.049129
10	6	0	4.653744	-1.653529	-0.334814
11	6	0	3.505302	-1.401161	-1.081115
12	6	0	2.396172	-0.895067	-0.40443
13	6	0	-2.422384	-0.895336	-0.442793
14	6	0	-3.510684	-1.410123	-1.146628
15	6	0	-4.717816	-1.531739	-0.464033
16	6	0	-4.867752	-1.172282	0.885674
17	6	0	-3.776818	-0.674318	1.585287
18	8	0	-1.197451	-0.749083	-0.973552
19	8	0	1.224046	-0.621735	-0.998977
20	14	0	-0.017917	0.076186	0.004247
21	6	0	-0.011557	1.895222	-0.369066
22	35	0	-6.23423	-2.216539	-1.397437
23	35	0	6.195984	-2.334272	-1.228993
24	6	0	0.699522	2.371558	-1.486428
25	6	0	0.734291	3.724559	-1.821058
26	6	0	0.044483	4.650057	-1.026082
27	6	0	-0.674172	4.201832	0.094024
28	6	0	-0.699077	2.851957	0.410359
29	6	0	-0.062341	0.873699	4.583495
30	7	0	-0.06353	1.245868	5.684393
31	8	0	0.008543	5.98837	-1.252929
32	6	0	0.715903	6.508252	-2.375794
33	1	0	3.632063	-0.755353	2.787358
34	1	0	5.642092	-1.641512	1.585329
35	1	0	3.462354	-1.583617	-2.147262
36	1	0	-3.406591	-1.697379	-2.185061
37	1	0	-5.828438	-1.286727	1.372182
38	1	0	-3.85573	-0.395774	2.629481
39	1	0	1.240909	1.671418	-2.114987
40	1	0	1.294496	4.043714	-2.69147
41	1	0	-1.203809	4.931514	0.697445
42	1	0	-1.272104	2.544324	1.279603
43	1	0	0.549671	7.585507	-2.359784
44	1	0	1.790533	6.305682	-2.30097
45	1	0	0.33288	6.095741	-3.316332

Low Frequencies:					
0.0023	0.0041	0.0063	1.0315	1.9028	3.0361
13.874	18.5726	31.5864			

Table S14. Optimized geometry of **SiPhNMe_Br**

Center Number	Atomic Number	Atomic Type	Coordinates (Angstroms) x	y	z
1	6	0	3.648612	-1.117551	1.704823
2	6	0	-2.529153	-0.794967	0.904999
3	6	0	2.486291	-0.849114	0.976554
4	1	0	1.739539	6.127366	-2.328952
5	7	0	1.256402	-0.393787	1.453782
6	7	0	1.162025	-0.119166	2.723773
7	6	0	-0.048976	0.151877	3.232089
8	7	0	-1.260841	-0.055388	2.692364
9	7	0	-1.322163	-0.329333	1.420175
10	6	0	4.770918	-1.571174	1.022852
11	6	0	4.704048	-1.757259	-0.366733
12	6	0	3.552127	-1.504382	-1.107183
13	6	0	2.432638	-1.038007	-0.418274
14	6	0	-2.381389	-1.132378	-0.455355
15	6	0	-3.45961	-1.651436	-1.172287
16	6	0	-4.665895	-1.80789	-0.495695
17	6	0	-4.825555	-1.478608	0.860325
18	6	0	-3.744887	-0.975709	1.572659
19	8	0	-1.158797	-0.954438	-0.979453
20	8	0	1.257438	-0.769282	-1.006255
21	14	0	0.002076	-0.117511	0.015902
22	6	0	-0.025889	1.701843	-0.307069
23	35	0	-6.168485	-2.500915	-1.447341
24	35	0	6.259651	-2.385181	-1.278263
25	6	0	0.63917	2.228674	-1.436122
26	6	0	0.64684	3.583937	-1.726923
27	6	0	-0.021088	4.513196	-0.888952
28	6	0	-0.69663	3.994028	0.244261
29	6	0	-0.692712	2.633971	0.515478
30	7	0	-0.014356	5.859612	-1.164043
31	6	0	-0.720152	6.788279	-0.29357
32	6	0	0.667615	6.362068	-2.347533
33	6	0	-0.056376	0.553292	4.614174
34	7	0	-0.063729	0.898195	5.72402
35	1	0	3.66335	-0.966512	2.777708
36	1	0	5.690581	-1.782376	1.55418
37	1	0	3.513666	-1.656688	-2.178228
38	1	0	-3.34802	-1.915866	-2.216012
39	1	0	-5.785123	-1.62013	1.34196
40	1	0	-3.830943	-0.720265	2.622209
41	1	0	1.167708	1.556965	-2.10598
42	1	0	1.175127	3.924821	-2.608493
43	1	0	-1.228963	4.656896	0.914627
44	1	0	-1.235966	2.298563	1.394061
45	1	0	-1.797427	6.578821	-0.25839
46	1	0	-0.333921	6.755099	0.733051
47	1	0	-0.586672	7.802434	-0.669164
48	1	0	0.244523	5.946142	-3.271308
49	1	0	0.562491	7.445935	-2.387705

Low Frequencies:					
-1.2539	0.0108	0.0111	0.0116	1.6861	1.9673
13.8442	16.5417	29.5673			

Table S15. Calculated electronic transitions for **SiOH_H**

Excited State	Spin Multiplicity	Energy / eV	Wavelength / nm	f	Composition	Coefficient
1	Singlet-A	2.2176	559.09	0.5497	HOMO-2 -> LUMO	-0.10942
					HOMO -> LUMO	0.6979
2	Singlet-A	2.4816	499.62	0.0735	HOMO-3 -> LUMO	0.11332
					HOMO-1 -> LUMO	0.69423
3	Singlet-A	2.8078	441.57	0.0831	HOMO-4 -> LUMO	-0.27528
					HOMO-2 -> LUMO	0.63909
4	Singlet-A	2.874	431.4	0.0303	HOMO-4 -> LUMO	0.63811
					HOMO-3 -> LUMO	-0.10014
					HOMO-2 -> LUMO	0.27526
5	Singlet-A	3.4312	361.35	0.0736	HOMO-4 -> LUMO	0.11388
					HOMO-3 -> LUMO	0.6785
					HOMO-1 -> LUMO	-0.107
					HOMO -> LUMO+1	0.1037
6	Singlet-A	4.2091	294.57	0.295	HOMO -> LUMO+1	0.68956
7	Singlet-A	4.2635	290.8	0.0095	HOMO-5 -> LUMO	0.65989
					HOMO-1 -> LUMO+1	0.1995
8	Singlet-A	4.6256	268.04	0.0197	HOMO-6 -> LUMO	-0.16854
					HOMO-5 -> LUMO	-0.16892
					HOMO-1 -> LUMO+1	0.64062
9	Singlet-A	4.6375	267.35	0.0074	HOMO-8 -> LUMO	-0.14785
					HOMO-7 -> LUMO	-0.3095
					HOMO-6 -> LUMO	0.55854
					HOMO-4 -> LUMO+1	-0.15861
					HOMO-1 -> LUMO+1	0.13298
10	Singlet-A	4.778	259.49	0.0042	HOMO-9 -> LUMO	-0.15248
					HOMO-7 -> LUMO	0.55377
					HOMO-6 -> LUMO	0.35486
					HOMO-4 -> LUMO+1	0.14033
11	Singlet-A	4.9647	249.73	0.0496	HOMO-2 -> LUMO+1	0.55337
					HOMO -> LUMO+2	0.4011
12	Singlet-A	5.007	247.62	0.005	HOMO-12 -> LUMO	-0.1067
					HOMO-9 -> LUMO	-0.11699
					HOMO-8 -> LUMO	0.64835
					HOMO-6 -> LUMO	0.1551

13	Singlet-A	5.1102	242.62	0.0092	HOMO-12 -> LUMO	-0.11427
					HOMO-11 -> LUMO	0.14871
					HOMO-9 -> LUMO	-0.23847
					HOMO-8 -> LUMO	-0.13047
					HOMO-7 -> LUMO	-0.22047
					HOMO-4 -> LUMO+1	0.3619
					HOMO-2 -> LUMO+1	-0.11797
					HOMO -> LUMO+2	0.23036
					HOMO -> LUMO+3	-0.31385
14	Singlet-A	5.1397	241.23	0.0361	HOMO-2 -> LUMO+1	-0.32761
					HOMO -> LUMO+2	0.36078
					HOMO -> LUMO+3	0.42768
15	Singlet-A	5.1603	240.27	0.022	HOMO-11 -> LUMO	0.15854
					HOMO-9 -> LUMO	-0.21136
					HOMO-7 -> LUMO	-0.1697
					HOMO-4 -> LUMO+1	0.26188
					HOMO-2 -> LUMO+1	0.24035
					HOMO -> LUMO+2	-0.29511
					HOMO -> LUMO+3	0.34858
16	Singlet-A	5.2557	235.91	0.0038	HOMO-10 -> LUMO	0.64325
					HOMO-9 -> LUMO	-0.25499
17	Singlet-A	5.2578	235.81	0.0289	HOMO-12 -> LUMO	0.1028
					HOMO-10 -> LUMO	0.24852
					HOMO-9 -> LUMO	0.44575
					HOMO-4 -> LUMO+1	0.4356
18	Singlet-A	5.3225	232.94	0.005	HOMO -> LUMO+4	-0.32942
					HOMO -> LUMO+5	0.60332
19	Singlet-A	5.3714	230.82	0.0081	HOMO-12 -> LUMO	-0.1516
					HOMO-11 -> LUMO	0.6011
					HOMO-9 -> LUMO	0.23075
					HOMO-4 -> LUMO+1	-0.12664
					HOMO-3 -> LUMO+1	-0.11637
20	Singlet-A	5.466	226.83	0.0317	HOMO-12 -> LUMO	0.57415
					HOMO-11 -> LUMO	0.17345
					HOMO-1 -> LUMO+2	0.16312
					HOMO -> LUMO+4	-0.25297
					HOMO -> LUMO+5	-0.10244

Table S16. Calculated electronic transitions for **SiMe_H**

Excited State	Spin Multiplicity	Energy / eV	Wavelength / nm	f	Composition	Coefficient
1	Singlet-A	2.05	604.79	0.4509	HOMO -> LUMO	0.70181
2	Singlet-A	2.4445	507.2	0.0589	HOMO-1 -> LUMO	0.69754
3	Singlet-A	2.8169	440.14	0.0002	HOMO-4 -> LUMO	0.69189
					HOMO-3 -> LUMO	-0.13248
4	Singlet-A	2.8283	438.38	0.1157	HOMO-2 -> LUMO	0.69816
5	Singlet-A	3.426	361.89	0.058	HOMO-4 -> LUMO	0.12843
					HOMO-3 -> LUMO	0.67148
					HOMO -> LUMO+1	-0.13841
6	Singlet-A	4.095	302.77	0.3368	HOMO-3 -> LUMO	0.12978
					HOMO -> LUMO+1	0.68748
7	Singlet-A	4.19	295.9	0.0442	HOMO-5 -> LUMO	0.67352
					HOMO-1 -> LUMO+1	0.13644
8	Singlet-A	4.4911	276.06	0.023	HOMO-8 -> LUMO	0.21977
					HOMO-6 -> LUMO	0.48378
					HOMO-1 -> LUMO+1	0.43589
9	Singlet-A	4.592	270	0.0179	HOMO-8 -> LUMO	-0.28844
					HOMO-6 -> LUMO	-0.2739
					HOMO-5 -> LUMO	-0.14458
					HOMO-4 -> LUMO+1	0.23139
					HOMO-1 -> LUMO+1	0.49522
10	Singlet-A	4.7704	259.9	0.0365	HOMO-8 -> LUMO	0.57154
					HOMO-6 -> LUMO	-0.38117
					HOMO-1 -> LUMO+1	0.13271
11	Singlet-A	4.8294	256.73	0.0001	HOMO-7 -> LUMO	0.69897
12	Singlet-A	4.9181	252.1	0.0609	HOMO-2 -> LUMO+1	-0.45708
					HOMO -> LUMO+2	0.50779
13	Singlet-A	5.0378	246.11	0.0466	HOMO-3 -> LUMO+1	-0.11205
					HOMO-2 -> LUMO+6	-0.1121
					HOMO-1 -> LUMO+4	0.14734
					HOMO -> LUMO+3	0.65139
14	Singlet-A	5.078	244.16	0.0112	HOMO-2 -> LUMO+1	0.51711
					HOMO -> LUMO+2	0.41479
					HOMO -> LUMO+4	0.16732
15	Singlet-A	5.162	240.19	0.0534	HOMO-8 -> LUMO	0.16882

					HOMO-6 -> LUMO	0.12401
					HOMO-4 -> LUMO+1	0.63131
					HOMO -> LUMO+6	0.1103
16	Singlet-A	5.2018	238.35	0.0092	HOMO-9 -> LUMO	0.63785
					HOMO -> LUMO+4	0.22606
17	Singlet-A	5.2745	235.06	0.0031	HOMO-9 -> LUMO	-0.15861
					HOMO -> LUMO+4	0.26362
					HOMO -> LUMO+5	0.61399
18	Singlet-A	5.2901	234.37	0.0022	HOMO-10 -> LUMO	0.69936
19	Singlet-A	5.3673	231	0.029	HOMO-9 -> LUMO	-0.16831
					HOMO-2 -> LUMO+2	0.12051
					HOMO -> LUMO+2	-0.10696
					HOMO -> LUMO+4	0.56252
					HOMO -> LUMO+5	-0.32011
20	Singlet-A	5.3889	230.07	0.0121	HOMO-11 -> LUMO	0.6578
					HOMO-3 -> LUMO+1	-0.10708
					HOMO -> LUMO+6	-0.15479

Table S17. Calculated electronic transitions for **SiPh_H**

Excited State	Spin Multiplicity	Energy / eV	Wavelength / nm	f	Composition	Coefficient
1	Singlet-A	2.0367	608.74	0.4314	HOMO -> LUMO	0.70167
2	Singlet-A	2.4069	515.12	0.0533	HOMO-5 -> LUMO	0.10136
					HOMO-1 -> LUMO	0.69771
3	Singlet-A	2.7086	457.74	0.0406	HOMO-6 -> LUMO	0.34707
					HOMO-4 -> LUMO	-0.25834
					HOMO-2 -> LUMO	0.54725
4	Singlet-A	2.811	441.07	0.0568	HOMO-6 -> LUMO	-0.38321
					HOMO-4 -> LUMO	0.33021
					HOMO-3 -> LUMO	0.22871
					HOMO-2 -> LUMO	0.4289
5	Singlet-A	2.8565	434.04	0.0121	HOMO-6 -> LUMO	0.16974
					HOMO-4 -> LUMO	-0.15748
					HOMO-3 -> LUMO	0.66272
6	Singlet-A	3.0203	410.51	0.0404	HOMO-6 -> LUMO	0.44478
					HOMO-4 -> LUMO	0.54274
7	Singlet-A	3.395	365.2	0.0565	HOMO-5 -> LUMO	0.68267
					HOMO -> LUMO+1	-0.12804
8	Singlet-A	4.1013	302.31	0.2979	HOMO-5 -> LUMO	0.12019
					HOMO -> LUMO+1	0.68779
9	Singlet-A	4.1318	300.07	0.0619	HOMO-8 -> LUMO	0.16188
					HOMO-7 -> LUMO	0.66933
10	Singlet-A	4.3999	281.79	0.0226	HOMO-10 -> LUMO	-0.116
					HOMO-8 -> LUMO	0.5871
					HOMO-7 -> LUMO	-0.10041
					HOMO-1 -> LUMO+1	0.31801
11	Singlet-A	4.5599	271.9	0.0023	HOMO-10 -> LUMO	0.13924
					HOMO-8 -> LUMO	-0.20834
					HOMO-7 -> LUMO	0.12584
					HOMO-6 -> LUMO+1	0.15999
					HOMO-1 -> LUMO+1	0.52668
					HOMO -> LUMO+2	-0.30254
12	Singlet-A	4.6141	268.71	0.0487	HOMO-10 -> LUMO	0.11263
					HOMO-6 -> LUMO+1	0.10266
					HOMO-1 -> LUMO+1	0.24556
					HOMO -> LUMO+2	0.63084

13	Singlet-A	4.6974	263.94	0.0109	HOMO-12 -> LUMO	-0.11675
					HOMO-10 -> LUMO	0.51898
					HOMO-9 -> LUMO	-0.32443
					HOMO-8 -> LUMO	0.23867
					HOMO-1 -> LUMO+1	-0.15668
14	Singlet-A	4.8026	258.16	0.0008	HOMO-11 -> LUMO	-0.11272
					HOMO-10 -> LUMO	0.37724
					HOMO-9 -> LUMO	0.57776
15	Singlet-A	4.8801	254.06	0.0355	HOMO-2 -> LUMO+1	0.36371
					HOMO -> LUMO+3	0.57446
16	Singlet-A	4.9644	249.75	0.0098	HOMO-2 -> LUMO+1	0.49834
					HOMO -> LUMO+3	-0.37081
					HOMO -> LUMO+4	-0.29811
17	Singlet-A	5.0544	245.3	0.0125	HOMO-6 -> LUMO+1	0.21901
					HOMO-4 -> LUMO+1	-0.36754
					HOMO-3 -> LUMO+1	-0.20308
					HOMO-2 -> LUMO+1	0.12452
					HOMO -> LUMO+4	0.42292
					HOMO -> LUMO+5	0.12535
18	Singlet-A	5.0553	245.25	0.0229	HOMO-3 -> LUMO+1	0.14287
					HOMO-1 -> LUMO+2	0.21492
					HOMO-1 -> LUMO+6	0.12497
					HOMO -> LUMO+5	0.60119
19	Singlet-A	5.0699	244.55	0.0038	HOMO-3 -> LUMO+1	0.60033
					HOMO-2 -> LUMO+1	0.1929
					HOMO -> LUMO+4	0.26382
20	Singlet-A	5.1275	241.8	0.0256	HOMO-11 -> LUMO	-0.12605
					HOMO-6 -> LUMO+1	-0.26652
					HOMO-4 -> LUMO+1	0.37325
					HOMO-3 -> LUMO+1	-0.23882
					HOMO-2 -> LUMO+1	0.2125
					HOMO -> LUMO+4	0.30235
					HOMO -> LUMO+6	-0.13105

Table S18. Calculated electronic transitions for **SiPhMe_H**

Excited State	Spin Multiplicity	Energy / eV	Wavelength / nm	f	Composition	Coefficient
1	Singlet-A	2.0403	607.67	0.4311	HOMO-34 -> LUMO-34	0.7017
2	Singlet-A	2.4084	514.79	0.0534	HOMO-39 -> LUMO-34	0.10115
					HOMO-35 -> LUMO-34	0.69743
3	Singlet-A	2.582	480.18	0.0421	HOMO-40 -> LUMO-34	-0.2086
					HOMO-36 -> LUMO-34	0.66914
4	Singlet-A	2.802	442.48	0.0343	HOMO-40 -> LUMO-34	-0.2122
					HOMO-38 -> LUMO-34	-0.11145
					HOMO-37 -> LUMO-34	0.64921
					HOMO-36 -> LUMO-34	-0.12645
5	Singlet-A	2.8395	436.64	0.0509	HOMO-40 -> LUMO-34	-0.25797
					HOMO-38 -> LUMO-34	0.64629
6	Singlet-A	2.8905	428.94	0.0285	HOMO-40 -> LUMO-34	0.57904
					HOMO-38 -> LUMO-34	0.25333
					HOMO-37 -> LUMO-34	0.26188
					HOMO-36 -> LUMO-34	0.1497
7	Singlet-A	3.4009	364.56	0.0573	HOMO-39 -> LUMO-34	0.68087
					HOMO-34 -> LUMO-33	-0.12948
8	Singlet-A	4.0993	302.45	0.2992	HOMO-39 -> LUMO-34	0.12152
					HOMO-34 -> LUMO-33	0.68751
9	Singlet-A	4.1368	299.71	0.0618	HOMO-42 -> LUMO-34	0.16222
					HOMO-41 -> LUMO-34	0.66872
10	Singlet-A	4.4002	281.77	0.0209	HOMO-44 -> LUMO-34	-0.1015
					HOMO-42 -> LUMO-34	0.58359
					HOMO-35 -> LUMO-33	0.32113
11	Singlet-A	4.5558	272.15	0.0072	HOMO-44 -> LUMO-34	0.13879
					HOMO-42 -> LUMO-34	-0.21035
					HOMO-41 -> LUMO-34	0.13843
					HOMO-40 -> LUMO-33	0.19025
					HOMO-35 -> LUMO-33	0.57206
					HOMO-34 -> LUMO-32	-0.11005
12	Singlet-A	4.678	265.04	0.0258	HOMO-45 -> LUMO-34	0.13843
					HOMO-44 -> LUMO-34	0.20297
					HOMO-43 -> LUMO-34	-0.15927
					HOMO-42 -> LUMO-34	0.10667
					HOMO-34 -> LUMO-32	0.61629

13	Singlet-A	4.6988	263.86	0.0298	HOMO-45 -> LUMO-34	0.25762
					HOMO-44 -> LUMO-34	0.36353
					HOMO-43 -> LUMO-34	-0.32595
					HOMO-42 -> LUMO-34	0.22029
					HOMO-35 -> LUMO-33	-0.17621
					HOMO-34 -> LUMO-32	-0.31402
14	Singlet-A	4.7992	258.34	0.0008	HOMO-45 -> LUMO-34	-0.18586
					HOMO-44 -> LUMO-34	0.51304
					HOMO-43 -> LUMO-34	0.41644
					HOMO-36 -> LUMO-33	0.13773
15	Singlet-A	4.8191	257.27	0.0204	HOMO-43 -> LUMO-34	-0.17047
					HOMO-36 -> LUMO-33	0.64352
					HOMO-34 -> LUMO-31	-0.15478
16	Singlet-A	4.9049	252.77	0.0199	HOMO-38 -> LUMO-33	0.16228
					HOMO-37 -> LUMO-33	0.19517
					HOMO-36 -> LUMO-33	0.15019
					HOMO-34 -> LUMO-31	0.61879
17	Singlet-A	4.9995	247.99	0.0173	HOMO-38 -> LUMO-33	0.11341
					HOMO-37 -> LUMO-33	0.48829
					HOMO-34 -> LUMO-31	-0.22075
					HOMO-34 -> LUMO-30	0.41988
18	Singlet-A	5.0356	246.22	0.0035	HOMO-38 -> LUMO-33	0.49994
					HOMO-37 -> LUMO-33	-0.36086
					HOMO-34 -> LUMO-30	0.27983
					HOMO-34 -> LUMO-29	-0.10716
19	Singlet-A	5.0566	245.19	0.0279	HOMO-45 -> LUMO-34	-0.10221
					HOMO-39 -> LUMO-33	-0.10496
					HOMO-35 -> LUMO-32	0.13733
					HOMO-35 -> LUMO-28	0.12619
					HOMO-34 -> LUMO-29	0.6183
20	Singlet-A	5.078	244.16	0.0011	HOMO-45 -> LUMO-34	0.54861
					HOMO-44 -> LUMO-34	-0.10993
					HOMO-43 -> LUMO-34	0.37285
					HOMO-40 -> LUMO-33	0.11611
					HOMO-34 -> LUMO-29	0.11051

Table S19. Calculated electronic transitions for **SiPhOMe_H**

Excited State	Spin Multiplicity	Energy / eV	Wavelength / nm	f	Composition	Coefficient
1	Singlet-A	2.0403	607.67	0.4311	HOMO -> LUMO	0.7017
2	Singlet-A	2.4084	514.79	0.0534	HOMO-5 -> LUMO	0.10115
					HOMO-1 -> LUMO	0.69743
3	Singlet-A	2.582	480.18	0.0421	HOMO-6 -> LUMO	-0.2086
					HOMO-2 -> LUMO	0.66914
4	Singlet-A	2.802	442.48	0.0343	HOMO-6 -> LUMO	-0.2122
					HOMO-4 -> LUMO	-0.11145
					HOMO-3 -> LUMO	0.64921
					HOMO-2 -> LUMO	-0.12645
5	Singlet-A	2.8395	436.64	0.0509	HOMO-6 -> LUMO	-0.25797
					HOMO-4 -> LUMO	0.64629
6	Singlet-A	2.8905	428.94	0.0285	HOMO-6 -> LUMO	0.57904
					HOMO-4 -> LUMO	0.25333
					HOMO-3 -> LUMO	0.26188
					HOMO-2 -> LUMO	0.1497
7	Singlet-A	3.4009	364.56	0.0573	HOMO-5 -> LUMO	0.68087
					HOMO -> LUMO+1	-0.12948
8	Singlet-A	4.0993	302.45	0.2992	HOMO-5 -> LUMO	0.12152
					HOMO -> LUMO+1	0.68751
9	Singlet-A	4.1368	299.71	0.0618	HOMO-8 -> LUMO	0.16222
					HOMO-7 -> LUMO	0.66872
10	Singlet-A	4.4002	281.77	0.0209	HOMO-10 -> LUMO	-0.1015
					HOMO-8 -> LUMO	0.58359
					HOMO-1 -> LUMO+1	0.32113
11	Singlet-A	4.5558	272.15	0.0072	HOMO-10 -> LUMO	0.13879
					HOMO-8 -> LUMO	-0.21035
					HOMO-7 -> LUMO	0.13843
					HOMO-6 -> LUMO+1	0.19025
					HOMO-1 -> LUMO+1	0.57206
					HOMO -> LUMO+2	-0.11005
12	Singlet-A	4.678	265.04	0.0258	HOMO-11 -> LUMO	0.13843
					HOMO-10 -> LUMO	0.20297
					HOMO-9 -> LUMO	-0.15927
					HOMO-8 -> LUMO	0.10667
					HOMO -> LUMO+2	0.61629

13	Singlet-A	4.6988	263.86	0.0298	HOMO-11 -> LUMO	0.25762
					HOMO-10 -> LUMO	0.36353
					HOMO-9 -> LUMO	-0.32595
					HOMO-8 -> LUMO	0.22029
					HOMO-1 -> LUMO+1	-0.17621
					HOMO -> LUMO+2	-0.31402
14	Singlet-A	4.7992	258.34	0.0008	HOMO-11 -> LUMO	-0.18586
					HOMO-10 -> LUMO	0.51304
					HOMO-9 -> LUMO	0.41644
					HOMO-2 -> LUMO+1	0.13773
15	Singlet-A	4.8191	257.27	0.0204	HOMO-9 -> LUMO	-0.17047
					HOMO-2 -> LUMO+1	0.64352
					HOMO -> LUMO+3	-0.15478
16	Singlet-A	4.9049	252.77	0.0199	HOMO-4 -> LUMO+1	0.16228
					HOMO-3 -> LUMO+1	0.19517
					HOMO-2 -> LUMO+1	0.15019
					HOMO -> LUMO+3	0.61879
17	Singlet-A	4.9995	247.99	0.0173	HOMO-4 -> LUMO+1	0.11341
					HOMO-3 -> LUMO+1	0.48829
					HOMO -> LUMO+3	-0.22075
					HOMO -> LUMO+4	0.41988
18	Singlet-A	5.0356	246.22	0.0035	HOMO-4 -> LUMO+1	0.49994
					HOMO-3 -> LUMO+1	-0.36086
					HOMO -> LUMO+4	0.27983
					HOMO -> LUMO+5	-0.10716
19	Singlet-A	5.0566	245.19	0.0279	HOMO-11 -> LUMO	-0.10221
					HOMO-5 -> LUMO+1	-0.10496
					HOMO-1 -> LUMO+2	0.13733
					HOMO-1 -> LUMO+6	0.12619
					HOMO -> LUMO+5	0.6183
20	Singlet-A	5.078	244.16	0.0011	HOMO-11 -> LUMO	0.54861
					HOMO-10 -> LUMO	-0.10993
					HOMO-9 -> LUMO	0.37285
					HOMO-6 -> LUMO+1	0.11611
					HOMO -> LUMO+5	0.11051

Table S20. Calculated electronic transitions for **SiPhNMe_H**

Excited State	Spin Multiplicity	Energy / eV	Wavelength / nm	f	Composition	Coefficient
1	Singlet-A	1.4932	830.32	0.0842	HOMO -> LUMO	0.70563
2	Singlet-A	2.0546	603.45	0.4304	HOMO-1 -> LUMO	0.70191
3	Singlet-A	2.447	506.68	0.0574	HOMO-2 -> LUMO	0.69759
4	Singlet-A	2.8194	439.76	0.0259	HOMO-6 -> LUMO	0.55921
					HOMO-5 -> LUMO	-0.12276
					HOMO-4 -> LUMO	0.23215
					HOMO-3 -> LUMO	0.33006
5	Singlet-A	2.8318	437.82	0.0373	HOMO-6 -> LUMO	-0.20001
					HOMO-4 -> LUMO	-0.33506
					HOMO-3 -> LUMO	0.58365
6	Singlet-A	2.8715	431.78	0.0392	HOMO-6 -> LUMO	-0.34272
					HOMO-4 -> LUMO	0.57617
					HOMO-3 -> LUMO	0.20009
7	Singlet-A	3.4197	362.56	0.056	HOMO-6 -> LUMO	0.14051
					HOMO-5 -> LUMO	0.66612
					HOMO-1 -> LUMO+1	0.12958
8	Singlet-A	3.612	343.26	0.0186	HOMO -> LUMO+1	0.69942
9	Singlet-A	3.9459	314.21	0.0091	HOMO-7 -> LUMO	0.69447
10	Singlet-A	4.0917	303.02	0.2931	HOMO-5 -> LUMO	-0.12284
					HOMO-1 -> LUMO+1	0.68414
11	Singlet-A	4.1831	296.39	0.0434	HOMO-9 -> LUMO	0.13317
					HOMO-8 -> LUMO	0.6699
					HOMO-2 -> LUMO+1	-0.11942
12	Singlet-A	4.4138	280.9	0.0505	HOMO-9 -> LUMO	0.11634
					HOMO -> LUMO+2	-0.4235
					HOMO -> LUMO+3	-0.1798
					HOMO -> LUMO+4	0.47497
					HOMO -> LUMO+5	0.11782
13	Singlet-A	4.4528	278.44	0.0291	HOMO-11 -> LUMO	-0.11446
					HOMO-9 -> LUMO	0.53713
					HOMO-2 -> LUMO+1	0.36667
					HOMO -> LUMO+2	0.11072
14	Singlet-A	4.5844	270.45	0.0179	HOMO-12 -> LUMO	0.11091
					HOMO-11 -> LUMO	0.16606

					HOMO-10 -> LUMO	0.12808
					HOMO-9 -> LUMO	-0.24269
					HOMO-8 -> LUMO	0.1405
					HOMO-6 -> LUMO+1	-0.19561
					HOMO-2 -> LUMO+1	0.53458
15	Singlet-A	4.6294	267.82	0.0479	HOMO-2 -> LUMO+1	-0.11388
					HOMO -> LUMO+2	0.52791
					HOMO -> LUMO+3	-0.11946
					HOMO -> LUMO+4	0.39079
					HOMO -> LUMO+5	0.11513
					HOMO -> LUMO+6	-0.13116
16	Singlet-A	4.6932	264.18	0.14	HOMO -> LUMO+3	0.64412
					HOMO -> LUMO+4	0.23843
17	Singlet-A	4.7227	262.53	0.0129	HOMO-12 -> LUMO	0.30337
					HOMO-11 -> LUMO	0.29586
					HOMO-10 -> LUMO	0.43293
					HOMO-9 -> LUMO	0.29464
					HOMO-2 -> LUMO+1	-0.13844
18	Singlet-A	4.7279	262.24	0.0227	HOMO -> LUMO+2	0.1146
					HOMO -> LUMO+5	0.11587
					HOMO -> LUMO+6	0.61247
					HOMO -> LUMO+7	0.19602
					HOMO -> LUMO+9	-0.19459
19	Singlet-A	4.7785	259.46	0.2671	HOMO-1 -> LUMO+2	-0.10004
					HOMO -> LUMO+3	0.10195
					HOMO -> LUMO+4	-0.14474
					HOMO -> LUMO+5	0.64388
20	Singlet-A	4.8172	257.38	0.0035	HOMO-12 -> LUMO	-0.14718
					HOMO-11 -> LUMO	0.58387
					HOMO-10 -> LUMO	-0.34564

Table S21. Calculated electronic transitions for **SiMe_Br**

Excited State	Spin Multiplicity	Energy / eV	Wavelength / nm	f	Composition	Coefficient
1	Singlet-A	1.9874	623.84	0.6313	HOMO -> LUMO	0.70476
2	Singlet-A	2.5427	487.6	0.0722	HOMO-3 -> LUMO	0.20472
					HOMO-1 -> LUMO	0.67356
3	Singlet-A	2.8156	440.35	0	HOMO-4 -> LUMO	0.69791
4	Singlet-A	2.8607	433.41	0.1047	HOMO-2 -> LUMO	0.70101
5	Singlet-A	3.1187	397.55	0.1	HOMO-3 -> LUMO	0.6643
					HOMO-1 -> LUMO	-0.20153
6	Singlet-A	3.7232	333.01	0.0254	HOMO-5 -> LUMO	0.69353
7	Singlet-A	3.9185	316.4	0.0004	HOMO-6 -> LUMO	0.70342
8	Singlet-A	3.923	316.04	0.0001	HOMO-7 -> LUMO	0.70477
9	Singlet-A	4.0134	308.93	0.3363	HOMO-8 -> LUMO	0.10703
					HOMO -> LUMO+1	0.68591
10	Singlet-A	4.3893	282.47	0.0235	HOMO-8 -> LUMO	0.69333
					HOMO -> LUMO+1	-0.10678
11	Singlet-A	4.4928	275.96	0.0324	HOMO-11 -> LUMO	0.12542
					HOMO-10 -> LUMO	-0.36972
					HOMO-9 -> LUMO	0.42674
					HOMO-4 -> LUMO+1	0.1053
					HOMO-1 -> LUMO+1	-0.3514
					HOMO -> LUMO+3	-0.14748
12	Singlet-A	4.6226	268.21	0.0111	HOMO-11 -> LUMO	0.31051
					HOMO-10 -> LUMO	-0.38109
					HOMO-9 -> LUMO	-0.10684
					HOMO-4 -> LUMO+1	0.20727
					HOMO-1 -> LUMO+1	0.40961
13	Singlet-A	4.6871	264.52	0.0009	HOMO-11 -> LUMO	-0.16024
					HOMO-10 -> LUMO	0.20321
					HOMO-9 -> LUMO	0.51694
					HOMO-1 -> LUMO+1	0.36685
14	Singlet-A	4.7814	259.31	0.0779	HOMO-2 -> LUMO+1	-0.21191
					HOMO -> LUMO+2	0.64035
15	Singlet-A	4.8565	255.3	0.0432	HOMO-3 -> LUMO+1	0.11778
					HOMO-1 -> LUMO+1	-0.17434
					HOMO-1 -> LUMO+6	0.10649
					HOMO -> LUMO+3	0.63933

16	Singlet-A	4.9058	252.73	0.0427	HOMO-11 -> LUMO	0.57171
					HOMO-10 -> LUMO	0.37955
17	Singlet-A	4.9087	252.58	0.0086	HOMO-1 -> LUMO+5	-0.15636
					HOMO -> LUMO+4	0.64874
					HOMO -> LUMO+6	-0.15028
18	Singlet-A	4.917	252.15	0.0017	HOMO-12 -> LUMO	0.69145
19	Singlet-A	4.9484	250.55	0.0008	HOMO-1 -> LUMO+4	-0.17453
					HOMO -> LUMO+5	0.66429
20	Singlet-A	5.0981	243.2	0.0107	HOMO-2 -> LUMO+1	0.55766
					HOMO -> LUMO+2	0.13949
					HOMO -> LUMO+6	0.37994

Table S22. Calculated electronic transitions for **SiPh_Br**

Excited State	Spin Multiplicity	Energy / eV	Wavelength / nm	f	Composition	Coefficient
1	Singlet-A	1.9723	628.62	0.6094	HOMO -> LUMO	0.7048
2	Singlet-A	2.5025	495.44	0.0626	HOMO-5 -> LUMO	0.10806
					HOMO-4 -> LUMO	-0.13904
					HOMO-1 -> LUMO	0.6722
3	Singlet-A	2.689	461.07	0.0328	HOMO-6 -> LUMO	-0.34565
					HOMO-5 -> LUMO	-0.20655
					HOMO-3 -> LUMO	-0.30985
					HOMO-2 -> LUMO	0.4826
4	Singlet-A	2.7561	449.85	0.0034	HOMO-3 -> LUMO	0.56533
					HOMO-2 -> LUMO	0.4175
5	Singlet-A	2.8419	436.28	0.0697	HOMO-6 -> LUMO	0.36546
					HOMO-5 -> LUMO	0.2611
					HOMO-4 -> LUMO	0.44101
					HOMO-3 -> LUMO	-0.22931
					HOMO-2 -> LUMO	0.20725
6	Singlet-A	2.9631	418.43	0.0579	HOMO-6 -> LUMO	0.4794
					HOMO-5 -> LUMO	-0.2641
					HOMO-4 -> LUMO	-0.38503
					HOMO-3 -> LUMO	-0.13518
					HOMO-2 -> LUMO	0.15724
7	Singlet-A	3.1052	399.28	0.0769	HOMO-5 -> LUMO	0.5482
					HOMO-4 -> LUMO	-0.35895
					HOMO-2 -> LUMO	0.11276
					HOMO-1 -> LUMO	-0.18528
8	Singlet-A	3.6937	335.67	0.0288	HOMO-7 -> LUMO	0.69135
9	Singlet-A	3.8842	319.2	0.0002	HOMO-9 -> LUMO	-0.15706
					HOMO-8 -> LUMO	0.68548
10	Singlet-A	3.891	318.64	0.0001	HOMO-9 -> LUMO	0.68627
					HOMO-8 -> LUMO	0.15887
11	Singlet-A	4.0204	308.39	0.3045	HOMO-10 -> LUMO	-0.11126
					HOMO -> LUMO+1	0.68557
12	Singlet-A	4.3552	284.68	0.0207	HOMO-11 -> LUMO	-0.18782
					HOMO-10 -> LUMO	0.66149
					HOMO -> LUMO+1	0.10532
13	Singlet-A	4.3819	282.95	0.0472	HOMO-11 -> LUMO	0.60116

					HOMO-10 -> LUMO	0.20376
					HOMO-1 -> LUMO+1	-0.20748
14	Singlet-A	4.5687	271.38	0.0118	HOMO-12 -> LUMO	0.24578
					HOMO-1 -> LUMO+1	-0.38207
					HOMO -> LUMO+2	0.48342
15	Singlet-A	4.6175	268.51	0.0486	HOMO-14 -> LUMO	0.10494
					HOMO-13 -> LUMO	-0.1342
					HOMO-12 -> LUMO	-0.3413
					HOMO-1 -> LUMO+1	0.28896
					HOMO -> LUMO+2	0.48789
16	Singlet-A	4.6708	265.45	0.0039	HOMO-12 -> LUMO	0.51526
					HOMO-11 -> LUMO	0.16474
					HOMO-6 -> LUMO+1	-0.13375
					HOMO-1 -> LUMO+1	0.38413
					HOMO -> LUMO+2	0.11326
17	Singlet-A	4.7336	261.93	0.0101	HOMO-15 -> LUMO	-0.20552
					HOMO-14 -> LUMO	-0.34527
					HOMO-13 -> LUMO	0.45764
					HOMO-12 -> LUMO	-0.17583
					HOMO-11 -> LUMO	0.18983
					HOMO-6 -> LUMO+1	0.12601
					HOMO-1 -> LUMO+1	0.14188
18	Singlet-A	4.7771	259.54	0.0645	HOMO-4 -> LUMO+1	0.12876
					HOMO-2 -> LUMO+1	0.14254
					HOMO -> LUMO+3	0.63867
19	Singlet-A	4.8822	253.95	0.0194	HOMO-14 -> LUMO	-0.11024
					HOMO-1 -> LUMO+1	0.12744
					HOMO -> LUMO+4	0.62784
					HOMO -> LUMO+6	-0.1061
20	Singlet-A	4.8864	253.73	0.0012	HOMO-16 -> LUMO	-0.10985
					HOMO-15 -> LUMO	-0.20355
					HOMO-14 -> LUMO	0.56109
					HOMO-13 -> LUMO	0.33412
					HOMO -> LUMO+4	0.10305

Table S23. Calculated electronic transitions for **SiPhMe_Br**

Excited State	Spin Multiplicity	Energy / eV	Wavelength / nm	f	Composition	Coefficient
1	Singlet-A	1.9769	627.17	0.6078	HOMO -> LUMO	0.70479
2	Singlet-A	2.469	502.16	0.0462	HOMO-5 -> LUMO	-0.10008
					HOMO-2 -> LUMO	0.34648
					HOMO-1 -> LUMO	0.5977
3	Singlet-A	2.552	485.82	0.0654	HOMO-6 -> LUMO	0.13943
					HOMO-5 -> LUMO	0.16874
					HOMO-2 -> LUMO	0.58158
					HOMO-1 -> LUMO	-0.32651
4	Singlet-A	2.7239	455.17	0.0019	HOMO-3 -> LUMO	0.70395
5	Singlet-A	2.8474	435.43	0.0564	HOMO-6 -> LUMO	-0.47229
					HOMO-5 -> LUMO	-0.11497
					HOMO-4 -> LUMO	0.49211
					HOMO-2 -> LUMO	0.10845
6	Singlet-A	2.8814	430.3	0.0498	HOMO-6 -> LUMO	0.48914
					HOMO-5 -> LUMO	-0.15515
					HOMO-4 -> LUMO	0.46226
					HOMO-2 -> LUMO	-0.12125
7	Singlet-A	3.1031	399.55	0.091	HOMO-5 -> LUMO	0.64421
					HOMO-4 -> LUMO	0.17783
					HOMO-2 -> LUMO	-0.10662
					HOMO-1 -> LUMO	0.17558
8	Singlet-A	3.7024	334.87	0.0291	HOMO-7 -> LUMO	0.69094
9	Singlet-A	3.9017	317.77	0.0003	HOMO-8 -> LUMO	0.70269
10	Singlet-A	3.9082	317.24	0.0001	HOMO-9 -> LUMO	0.70369
11	Singlet-A	4.0196	308.45	0.3068	HOMO-10 -> LUMO	-0.10747
					HOMO -> LUMO+1	0.68602
12	Singlet-A	4.3639	284.11	0.0219	HOMO-11 -> LUMO	0.27855
					HOMO-10 -> LUMO	0.62358
13	Singlet-A	4.3807	283.02	0.0433	HOMO-11 -> LUMO	0.56747
					HOMO-10 -> LUMO	-0.30111
					HOMO-1 -> LUMO+1	0.18384
14	Singlet-A	4.5716	271.21	0.0037	HOMO-14 -> LUMO	0.14189
					HOMO-12 -> LUMO	-0.26254

					HOMO-6 -> LUMO+1	0.14244
					HOMO-1 -> LUMO+1	0.54598
					HOMO -> LUMO+2	0.18798
15	Singlet-A	4.6637	265.85	0.0087	HOMO-12 -> LUMO	0.58392
					HOMO-11 -> LUMO	-0.1203
					HOMO-2 -> LUMO+1	0.10647
					HOMO-1 -> LUMO+1	0.19218
					HOMO -> LUMO+2	0.24205
16	Singlet-A	4.6695	265.52	0.0509	HOMO-12 -> LUMO	-0.1669
					HOMO-6 -> LUMO+1	-0.10394
					HOMO-2 -> LUMO+1	-0.16691
					HOMO-1 -> LUMO+1	-0.21167
					HOMO -> LUMO+2	0.59597
					HOMO -> LUMO+3	0.10052
17	Singlet-A	4.7286	262.2	0.0189	HOMO-15 -> LUMO	0.24389
					HOMO-14 -> LUMO	0.39571
					HOMO-13 -> LUMO	-0.2954
					HOMO-12 -> LUMO	0.11411
					HOMO-11 -> LUMO	0.21194
					HOMO-2 -> LUMO+1	0.21335
					HOMO-1 -> LUMO+1	-0.17904
					HOMO -> LUMO+2	0.16699
18	Singlet-A	4.7639	260.26	0.0462	HOMO-14 -> LUMO	-0.19295
					HOMO-13 -> LUMO	0.12441
					HOMO-12 -> LUMO	-0.15655
					HOMO-4 -> LUMO+1	0.12415
					HOMO-2 -> LUMO+1	0.42719
					HOMO -> LUMO+3	-0.42438
19	Singlet-A	4.7986	258.38	0.0206	HOMO-4 -> LUMO+1	-0.11461
					HOMO-2 -> LUMO+1	0.43737
					HOMO -> LUMO+3	0.47858
20	Singlet-A	4.871	254.53	0.0024	HOMO-15 -> LUMO	-0.30612
					HOMO-14 -> LUMO	0.46409
					HOMO-13 -> LUMO	0.41621

Table S24. Calculated electronic transitions for **SiPhOMe_Br**

Excited State	Spin Multiplicity	Energy / eV	Wavelength / nm	f	Composition	Coefficient
1	Singlet-A	1.9837	625	0.6072	HOMO -> LUMO	0.70454
2	Singlet-A	2.1047	589.07	0.0586	HOMO-1 -> LUMO	0.70186
3	Singlet-A	2.5307	489.91	0.0701	HOMO-5 -> LUMO	-0.19727
					HOMO-2 -> LUMO	0.67307
4	Singlet-A	2.8231	439.18	0.0004	HOMO-6 -> LUMO	0.57998
					HOMO-4 -> LUMO	0.34931
					HOMO-3 -> LUMO	0.18441
5	Singlet-A	2.8586	433.73	0.0904	HOMO-4 -> LUMO	-0.23963
					HOMO-3 -> LUMO	0.6521
6	Singlet-A	2.8795	430.57	0.0087	HOMO-6 -> LUMO	-0.38215
					HOMO-4 -> LUMO	0.56326
					HOMO-3 -> LUMO	0.16396
7	Singlet-A	3.1083	398.88	0.094	HOMO-5 -> LUMO	0.66388
					HOMO-2 -> LUMO	0.19632
8	Singlet-A	3.7221	333.1	0.0252	HOMO-7 -> LUMO	0.69157
9	Singlet-A	3.9149	316.7	0.0003	HOMO-8 -> LUMO	0.70204
10	Singlet-A	3.9262	315.79	0.0001	HOMO-9 -> LUMO	0.70241
11	Singlet-A	4.0227	308.21	0.3087	HOMO-10 -> LUMO	0.1069
					HOMO -> LUMO+1	0.68586
12	Singlet-A	4.2884	289.11	0.0089	HOMO-1 -> LUMO+1	0.69741
13	Singlet-A	4.3733	283.5	0.0186	HOMO-10 -> LUMO	0.68968
					HOMO -> LUMO+1	-0.10772
14	Singlet-A	4.4693	277.41	0.0382	HOMO-15 -> LUMO	-0.16287
					HOMO-14 -> LUMO	0.36584
					HOMO-12 -> LUMO	-0.12323
					HOMO-11 -> LUMO	0.43859
					HOMO-6 -> LUMO+1	-0.10971
					HOMO-2 -> LUMO+1	0.29205
15	Singlet-A	4.6214	268.28	0.0022	HOMO-15 -> LUMO	0.29019
					HOMO-14 -> LUMO	-0.32929
					HOMO-12 -> LUMO	0.22083
					HOMO-11 -> LUMO	0.19915

					HOMO-6 -> LUMO+1	0.13441
					HOMO-2 -> LUMO+1	0.38882
					HOMO -> LUMO+3	-0.1168
16	Singlet-A	4.6851	264.63	0.0005	HOMO-14 -> LUMO	-0.13443
					HOMO-12 -> LUMO	0.15981
					HOMO-11 -> LUMO	0.47357
					HOMO-6 -> LUMO+1	-0.10331
					HOMO-2 -> LUMO+1	-0.41564
17	Singlet-A	4.7434	261.38	0.0105	HOMO-16 -> LUMO	0.18138
					HOMO-14 -> LUMO	0.25733
					HOMO-12 -> LUMO	0.60197
					HOMO-11 -> LUMO	-0.10302
					HOMO -> LUMO+2	0.10269
18	Singlet-A	4.7659	260.15	0.0094	HOMO-16 -> LUMO	0.12198
					HOMO-15 -> LUMO	-0.28686
					HOMO-14 -> LUMO	-0.10651
					HOMO-13 -> LUMO	0.52842
					HOMO -> LUMO+2	-0.2045
					HOMO -> LUMO+3	-0.20826
19	Singlet-A	4.7753	259.64	0.0644	HOMO-15 -> LUMO	-0.12188
					HOMO-13 -> LUMO	0.24143
					HOMO-3 -> LUMO+1	-0.14196
					HOMO -> LUMO+2	0.56527
					HOMO -> LUMO+3	0.16625
20	Singlet-A	4.794	258.62	0.0717	HOMO-13 -> LUMO	0.12453
					HOMO-2 -> LUMO+1	0.19432
					HOMO -> LUMO+2	-0.21862
					HOMO -> LUMO+3	0.60595

Table S25. Calculated electronic transitions for **SiPhNMe_Br**

Excited State	Spin Multiplicity	Energy / eV	Wavelength / nm	f	Composition	Coefficient
1	Singlet-A	1.4093	879.73	0.0928	HOMO -> LUMO	0.70584
2	Singlet-A	1.9961	621.13	0.599	HOMO-1 -> LUMO	0.70461
3	Singlet-A	2.5425	487.66	0.0707	HOMO-5 -> LUMO	0.18532
					HOMO-2 -> LUMO	0.67822
4	Singlet-A	2.7623	448.84	0.001	HOMO-6 -> LUMO	0.11763
					HOMO-3 -> LUMO	0.69323
5	Singlet-A	2.8282	438.39	0.0057	HOMO-6 -> LUMO	0.64786
					HOMO-4 -> LUMO	0.20523
					HOMO-3 -> LUMO	-0.13076
6	Singlet-A	2.8853	429.72	0.0862	HOMO-6 -> LUMO	-0.21235
					HOMO-4 -> LUMO	0.66776
7	Singlet-A	3.1314	395.94	0.0935	HOMO-5 -> LUMO	0.66687
					HOMO-2 -> LUMO	-0.18238
8	Singlet-A	3.5195	352.28	0.0246	HOMO -> LUMO+1	0.6998
9	Singlet-A	3.745	331.07	0.022	HOMO-7 -> LUMO	0.68092
10	Singlet-A	3.869	320.45	0.0078	HOMO-10 -> LUMO	0.1342
					HOMO-8 -> LUMO	0.67133
11	Singlet-A	3.9748	311.93	0.0053	HOMO-10 -> LUMO	0.63856
					HOMO-9 -> LUMO	-0.22472
					HOMO-8 -> LUMO	-0.16806
12	Singlet-A	3.978	311.67	0.0003	HOMO-10 -> LUMO	0.23554
					HOMO-9 -> LUMO	0.66384
13	Singlet-A	4.0206	308.37	0.2998	HOMO-10 -> LUMO	-0.10779
					HOMO-1 -> LUMO+1	0.67672
14	Singlet-A	4.3657	284	0.0309	HOMO -> LUMO+2	0.58962
					HOMO -> LUMO+6	-0.15632
					HOMO -> LUMO+7	-0.31267
15	Singlet-A	4.4092	281.19	0.0156	HOMO-11 -> LUMO	0.66846
					HOMO -> LUMO+2	0.12075
					HOMO -> LUMO+3	-0.10037
16	Singlet-A	4.4431	279.05	0.0196	HOMO-15 -> LUMO	-0.10971
					HOMO-13 -> LUMO	0.27633

					HOMO-12 -> LUMO	0.42829
					HOMO-11 -> LUMO	-0.12781
					HOMO-2 -> LUMO+1	0.23827
					HOMO -> LUMO+2	0.17375
					HOMO -> LUMO+6	0.10634
					HOMO -> LUMO+7	0.27044
17	Singlet-A	4.4715	277.28	0.0667	HOMO-13 -> LUMO	-0.157
					HOMO-12 -> LUMO	-0.25743
					HOMO-2 -> LUMO+1	-0.13015
					HOMO -> LUMO+2	0.31919
					HOMO -> LUMO+6	0.20448
					HOMO -> LUMO+7	0.45373
18	Singlet-A	4.4871	276.31	0.0309	HOMO-11 -> LUMO	0.10246
					HOMO -> LUMO+3	0.68843
19	Singlet-A	4.6101	268.94	0.1523	HOMO-2 -> LUMO+1	-0.2278
					HOMO -> LUMO+4	0.54507
					HOMO -> LUMO+5	0.11884
					HOMO -> LUMO+6	-0.24494
					HOMO -> LUMO+7	0.18263
20	Singlet-A	4.6165	268.57	0.0208	HOMO-16 -> LUMO	0.10313
					HOMO-15 -> LUMO	0.20348
					HOMO-14 -> LUMO	0.12654
					HOMO-13 -> LUMO	-0.30343
					HOMO-6 -> LUMO+1	0.16167
					HOMO-2 -> LUMO+1	0.45936
					HOMO-1 -> LUMO+3	0.11016
					HOMO -> LUMO+4	0.19782

NMR Spectra

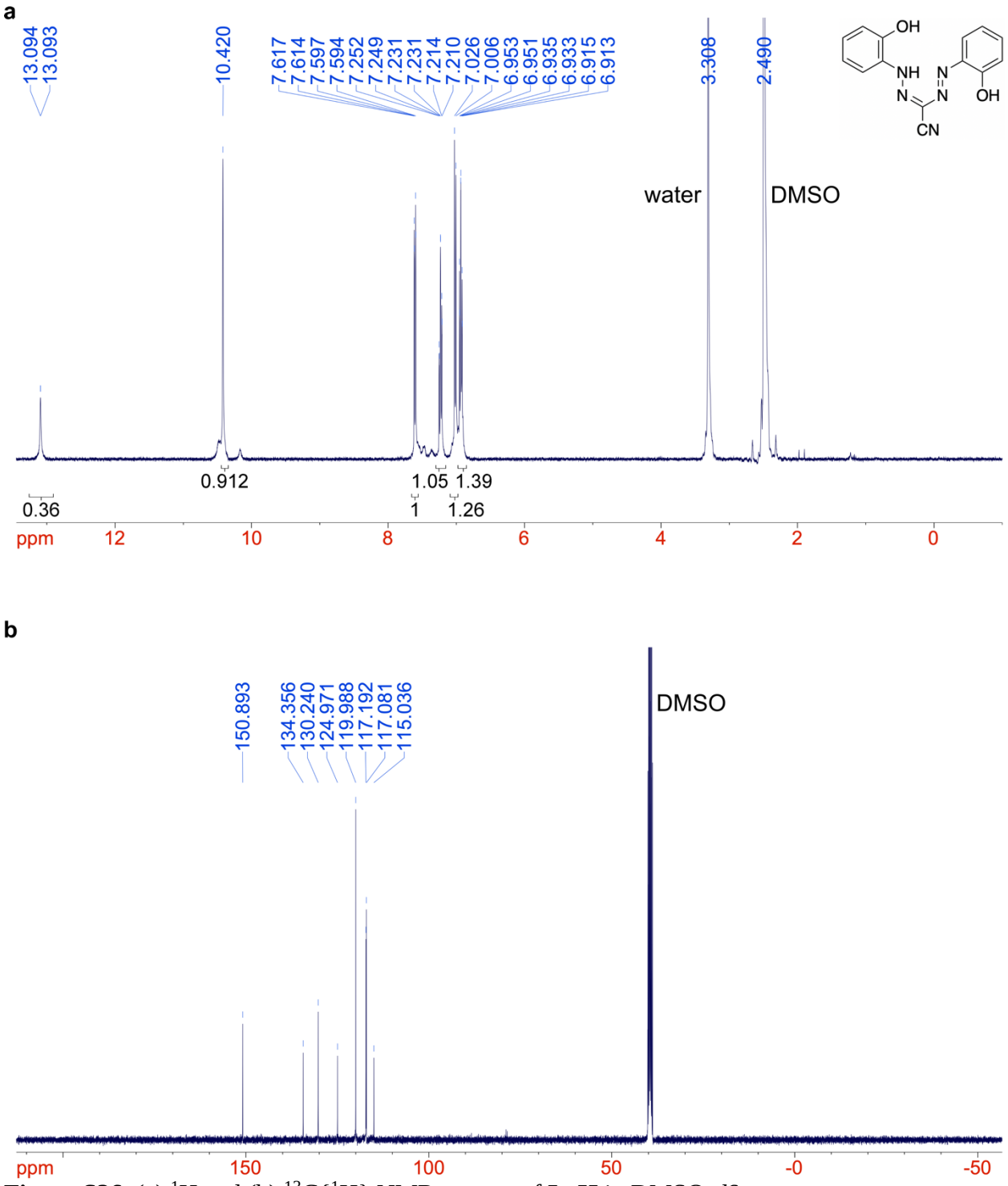

Figure S26. (a) ^{1}H and (b) ^{13}C{^{1}H} NMR spectra of **L_H** in DMSO-*d*6.

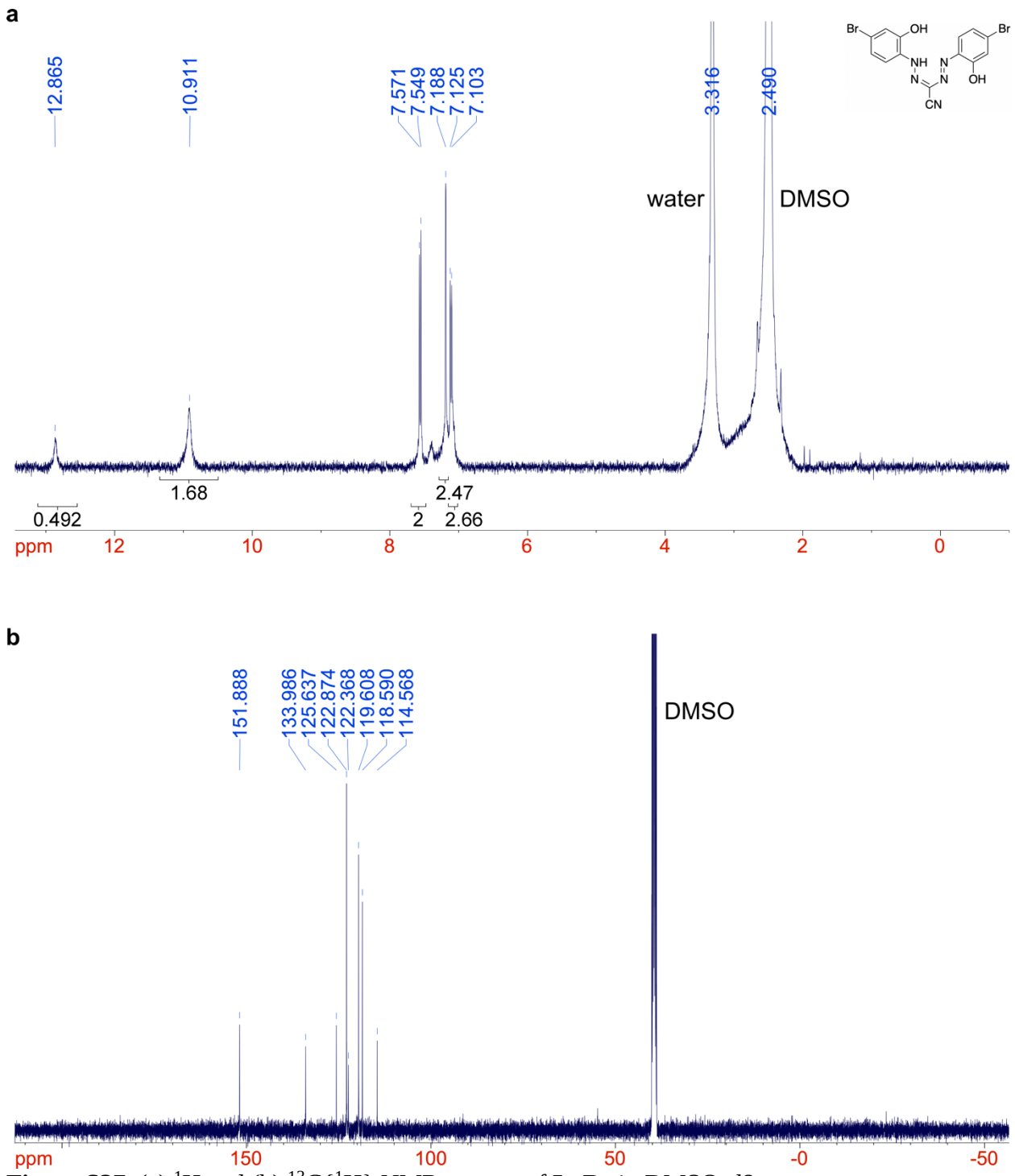

Figure S27. (a) ^{1}H and (b) ^{13}C{^{1}H} NMR spectra of **L_Br** in DMSO-*d*6.

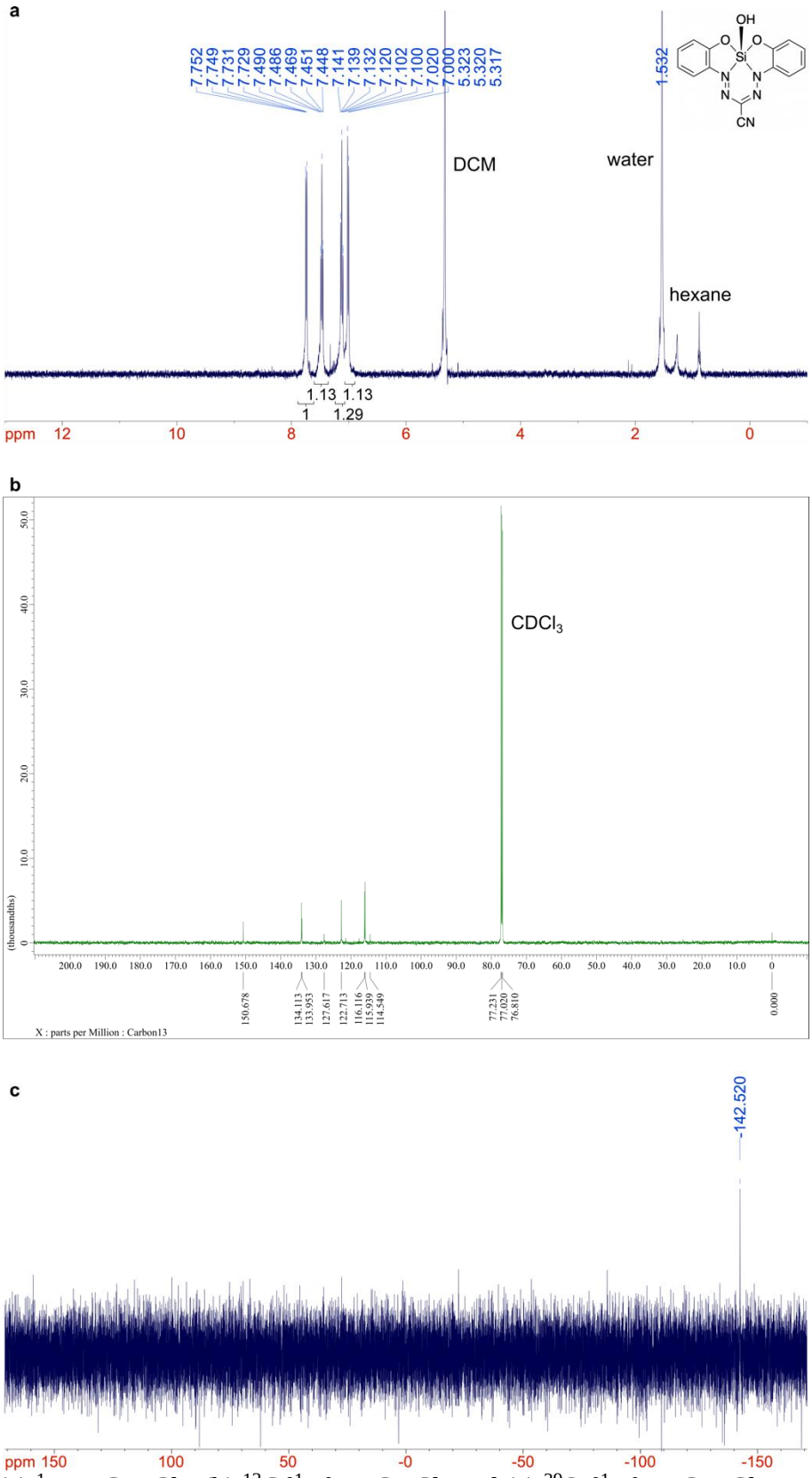

Figure S28. (a) ^{1}H in CD_2Cl_2, (b) $^{13}C\{^{1}H\}$ in $CDCl_3$ and (c) $^{29}Si\{^{1}H\}$ in CD_2Cl_2 NMR spectra of **SiOH_H**.

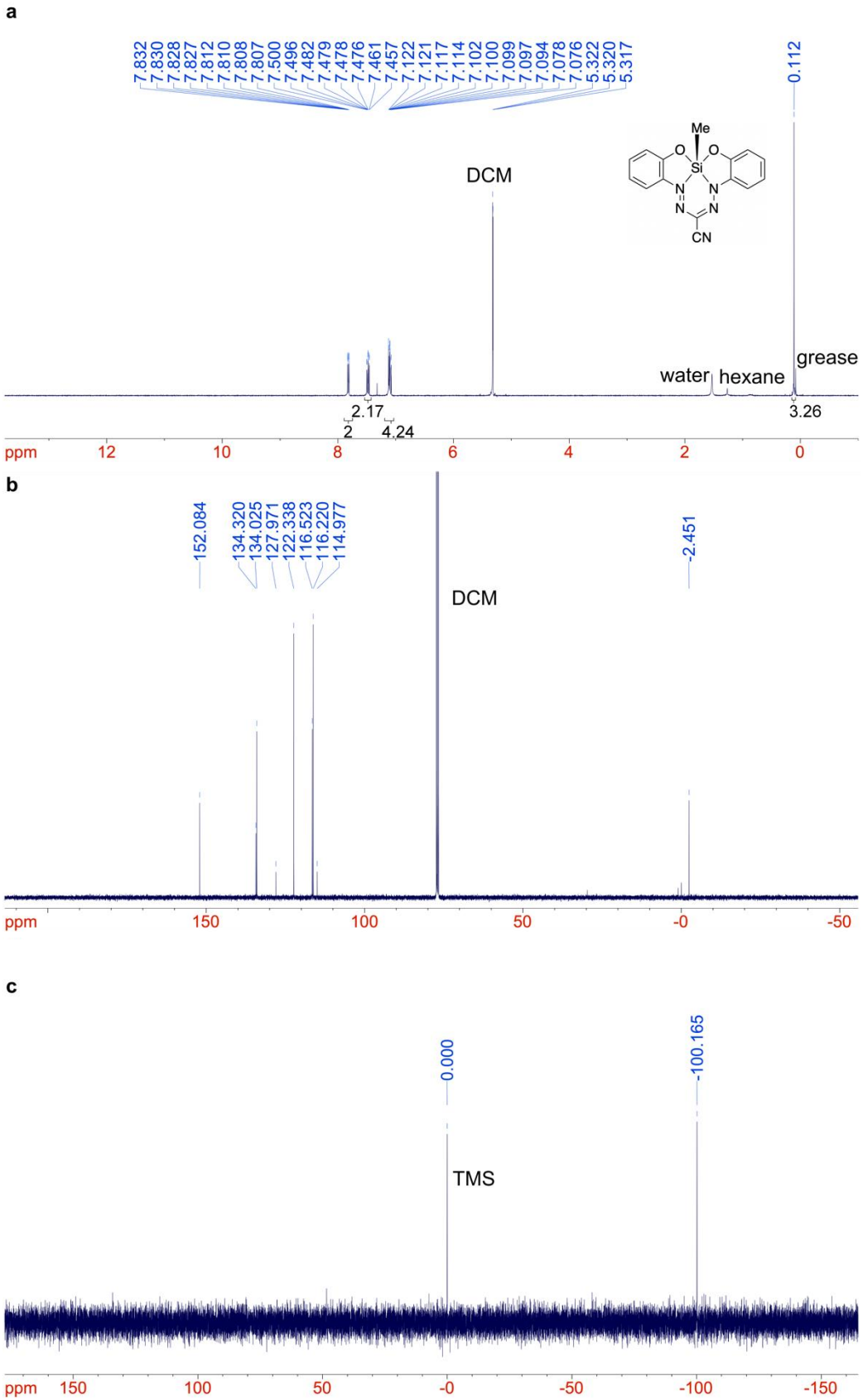

Figure S29. (a) ^{1}H, (b) ^{13}C{^{1}H} and (c) ^{29}Si{^{1}H} NMR spectra of **SiMe_H** in CD_2Cl_2.

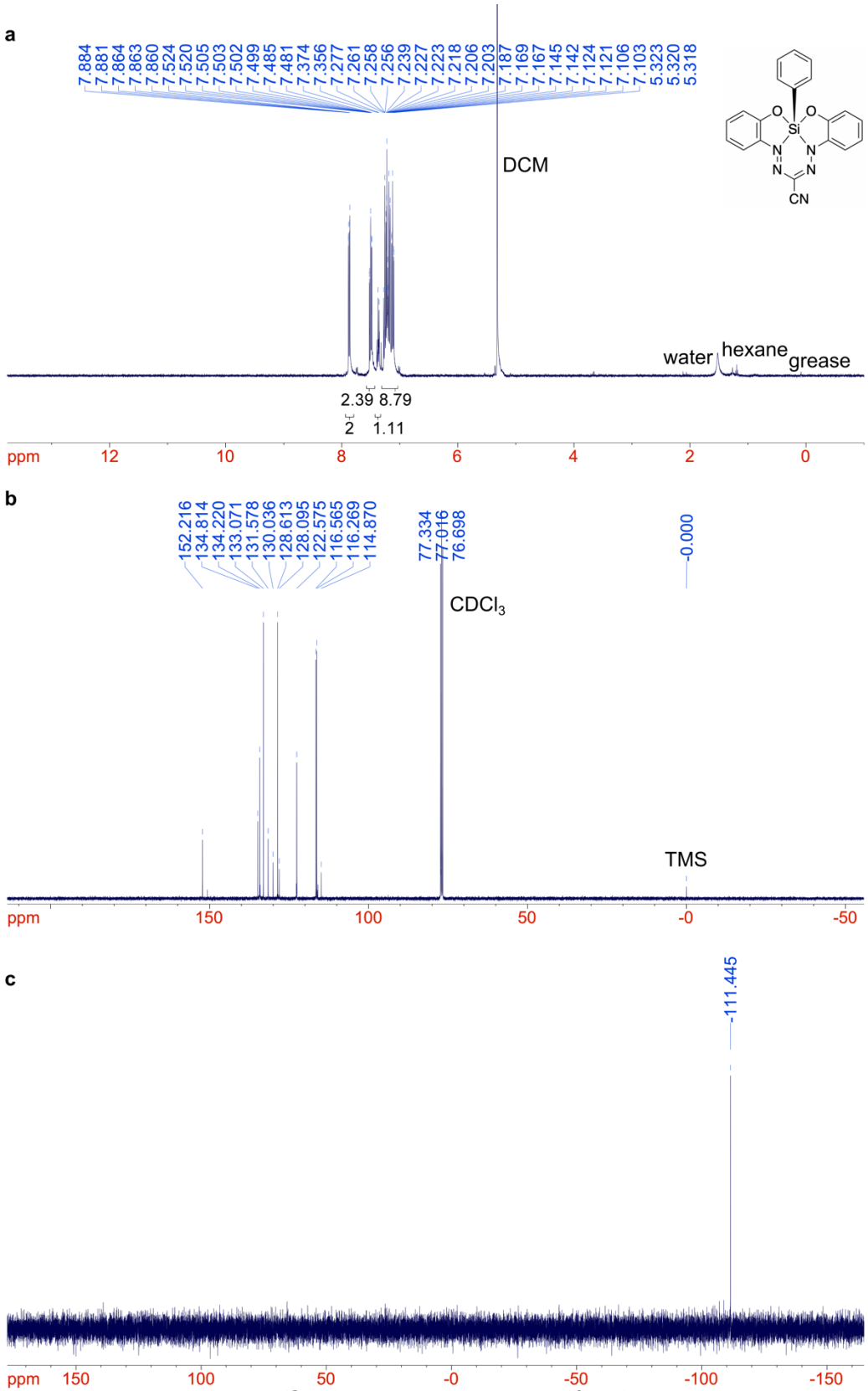

Figure S30. (a) ^{1}H in CD_2Cl_2, (b) $^{13}C\{^{1}H\}$ in $CDCl_3$ and (c) $^{29}Si\{^{1}H\}$ in CD_2Cl_2 NMR spectra of **SiPh_H**.

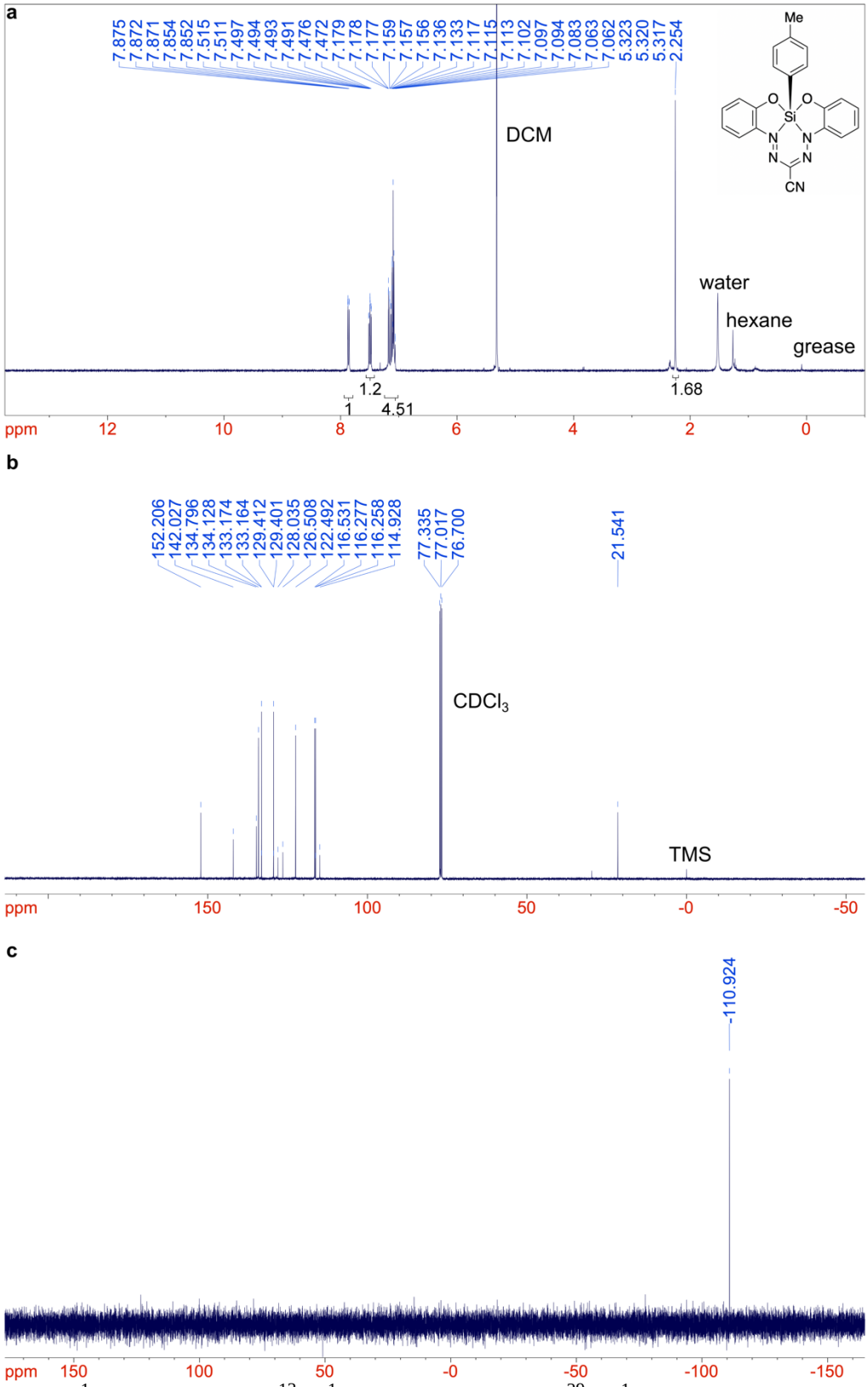

Figure S31. (a) ^{1}H in CD_2Cl_2, (b) $^{13}C\{^{1}H\}$ in $CDCl_3$ and (c) $^{29}Si\{^{1}H\}$ in CD_2Cl_2 NMR spectra of **SiPhMe_H**.

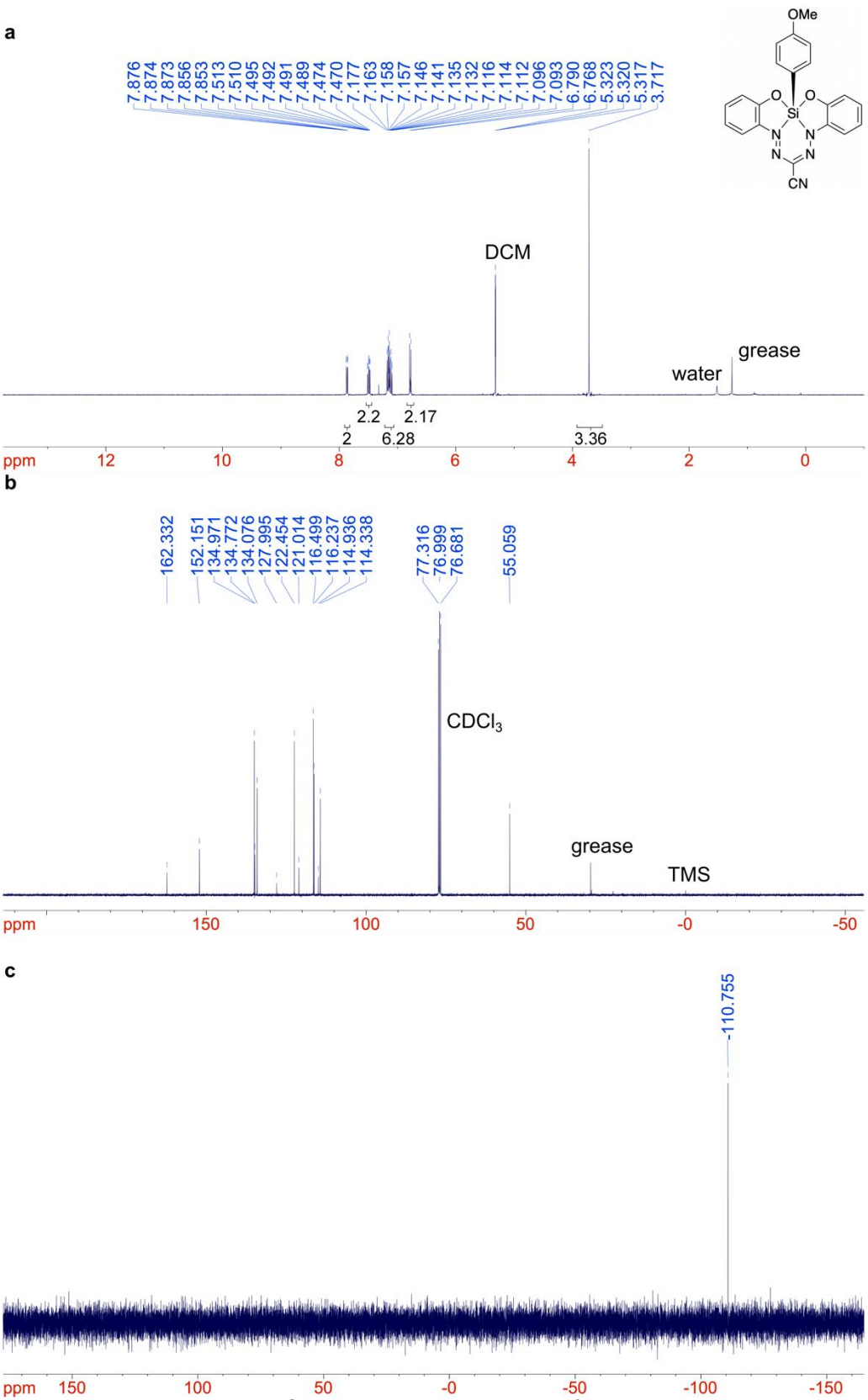

Figure S32. (a) ^{1}H in CD_2Cl_2, (b) $^{13}C\{^{1}H\}$ in $CDCl_3$ and (c) $^{29}Si\{^{1}H\}$ in CD_2Cl_2 NMR spectra of **SiPhOMe_H**.

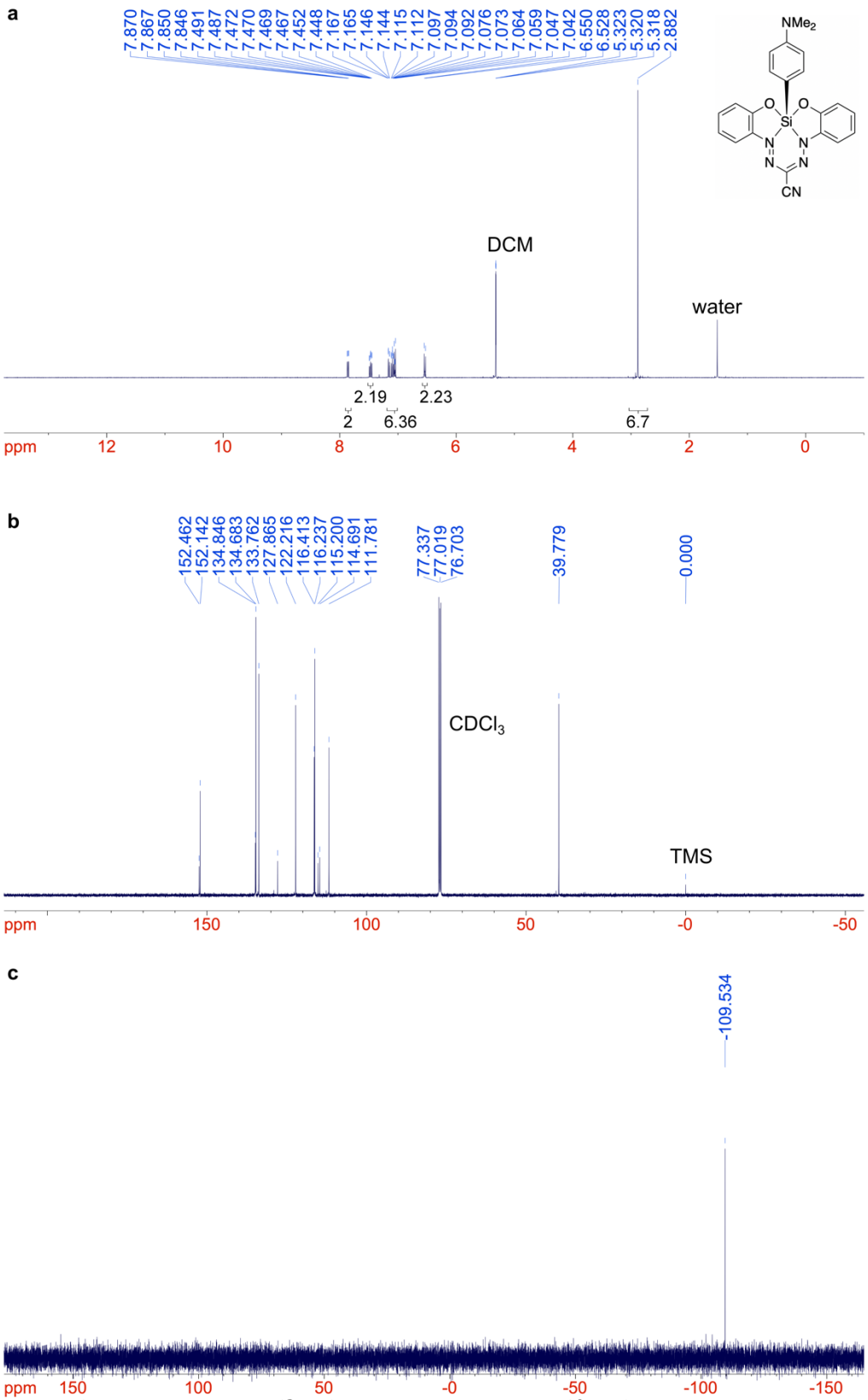

Figure S33. (a) ^{1}H in CD_2Cl_2, (b) $^{13}C\{^{1}H\}$ in $CDCl_3$ and (c) $^{29}Si\{^{1}H\}$ in CD_2Cl_2 NMR spectra of **SiPhNMe_H**.

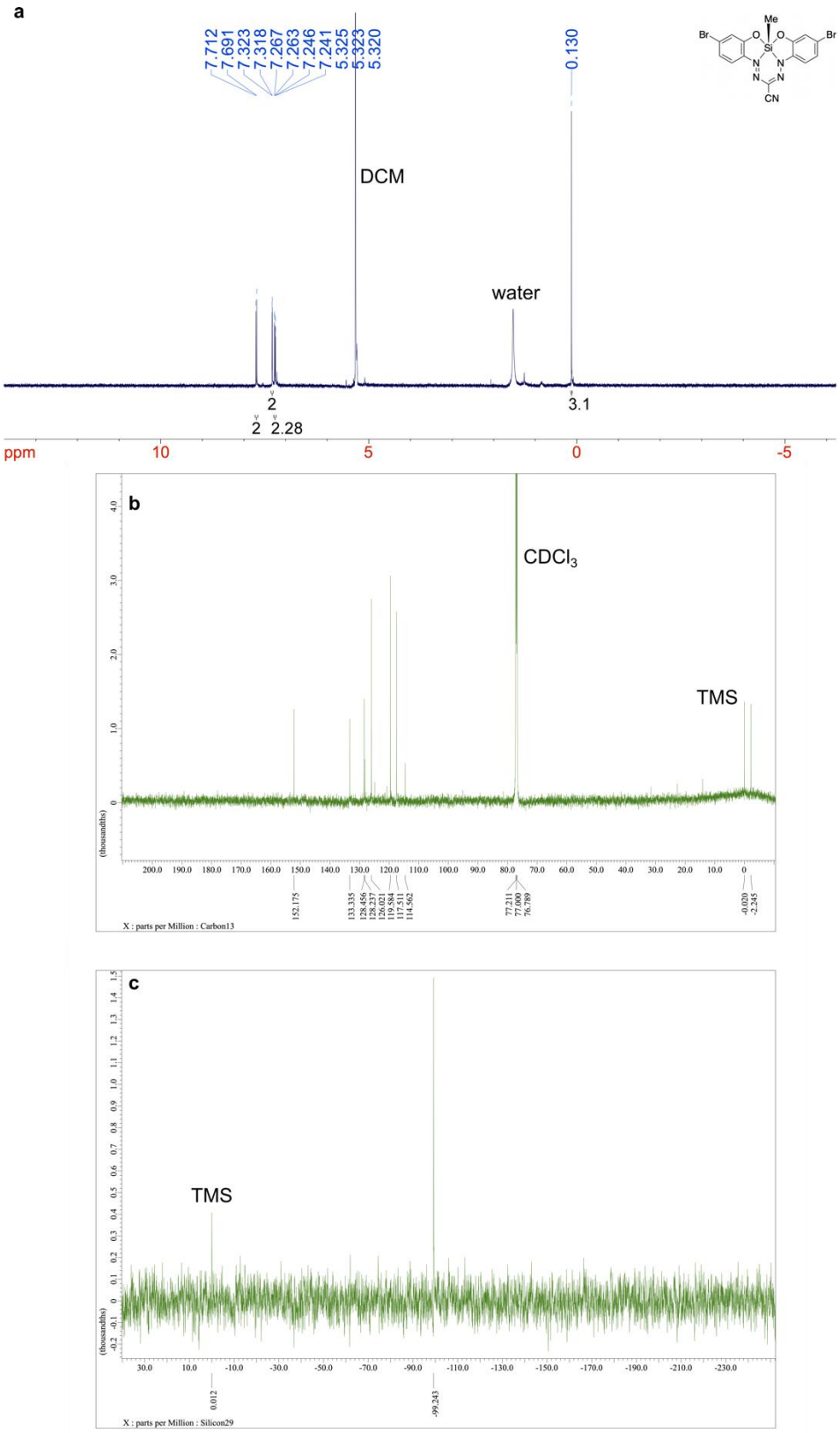

Figure S34. (a) ^{1}H in CD_2Cl_2, (b) $^{13}C\{^{1}H\}$ in $CDCl_3$ and (c) $^{29}Si\{^{1}H\}$ in CD_2Cl_2 NMR spectra of **SiMe_Br**.

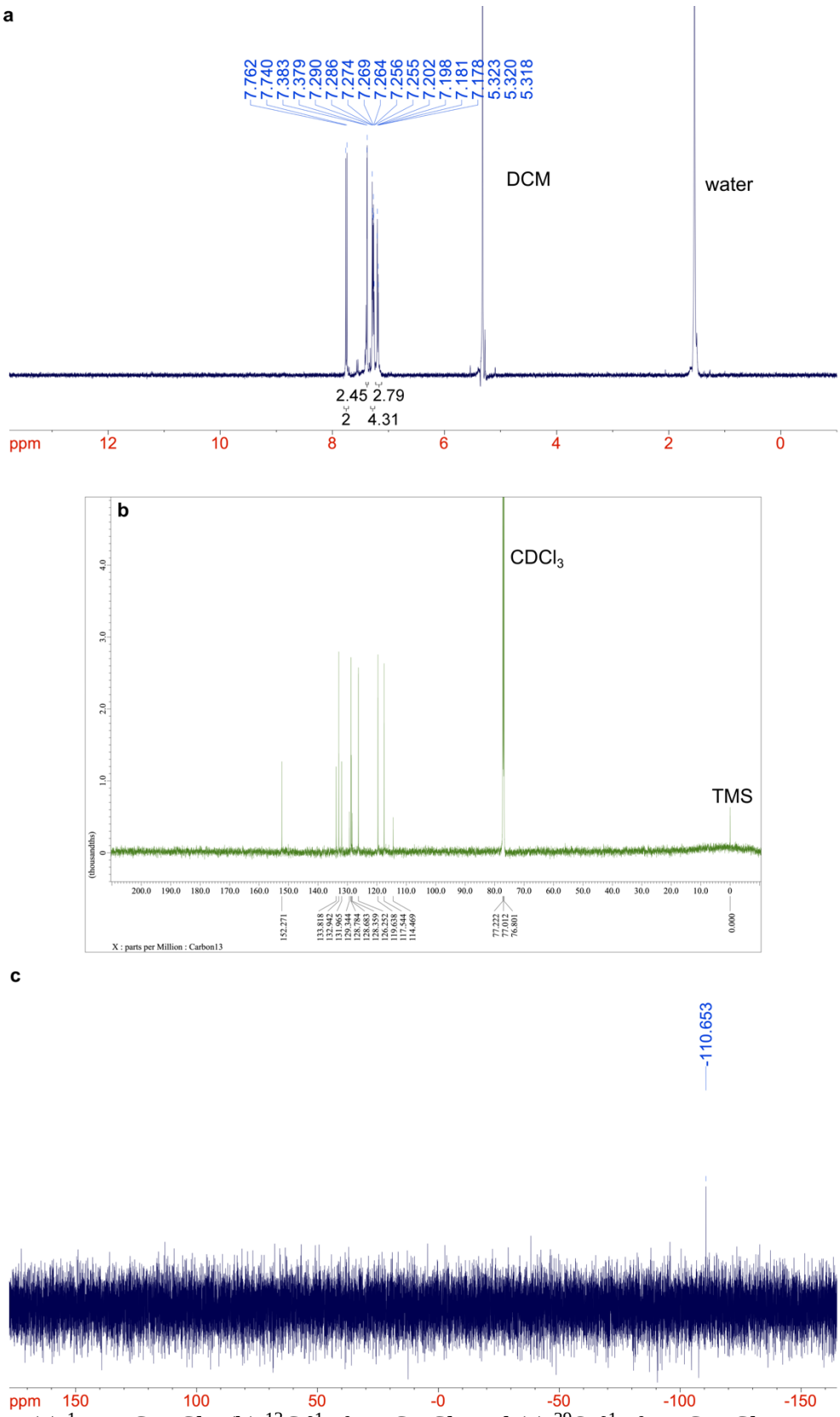

Figure S35. (a) ^{1}H in CD_2Cl_2, (b) $^{13}C\{^{1}H\}$ in $CDCl_3$ and (c) $^{29}Si\{^{1}H\}$ in CD_2Cl_2 NMR spectra of **SiPh_Br**.

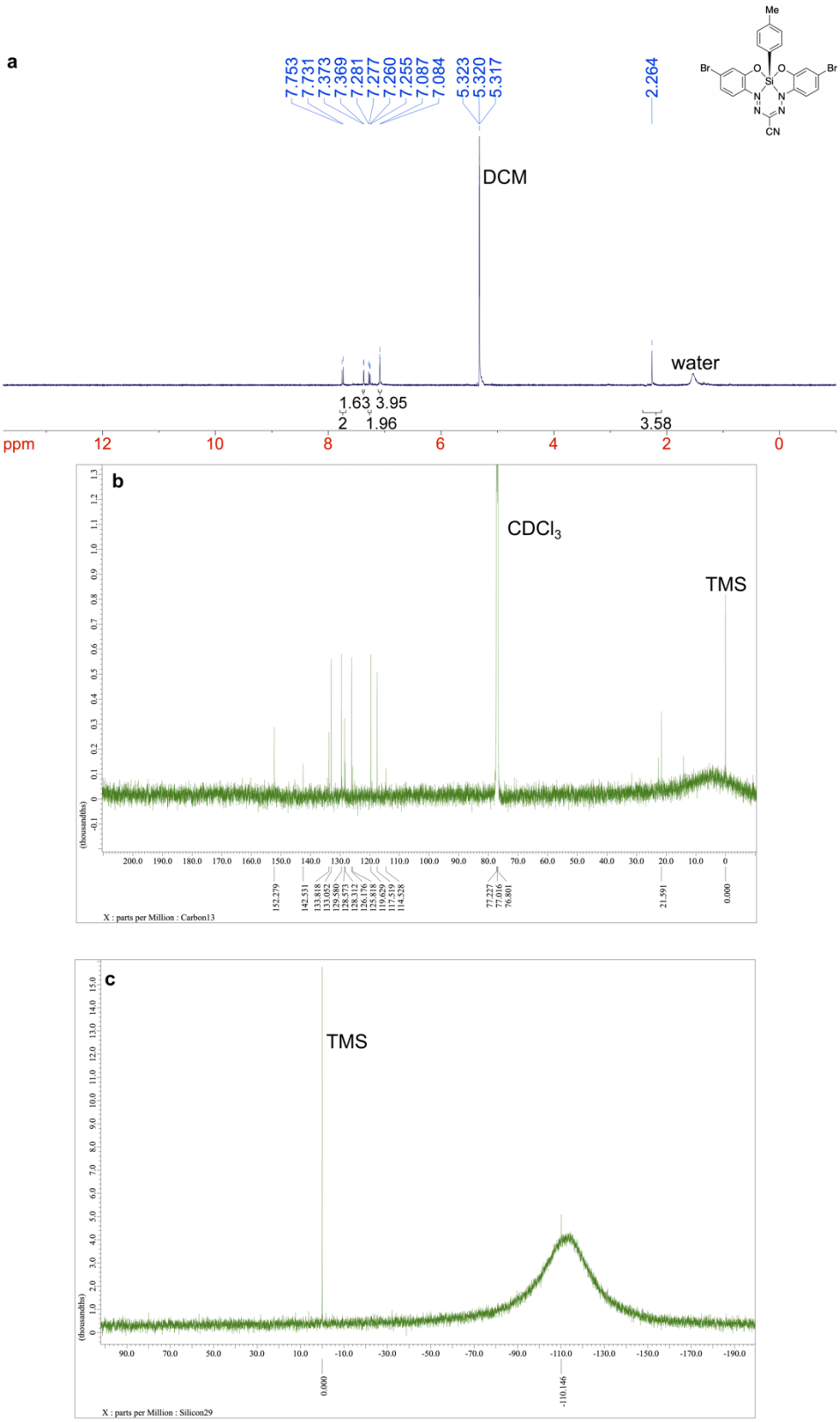

Figure S36. (a) ^{1}H in CD_2Cl_2, (b) $^{13}C\{^{1}H\}$ in $CDCl_3$ and (c) $^{29}Si\{^{1}H\}$ in CD_2Cl_2 NMR spectra of **SiPhMe_Br**.

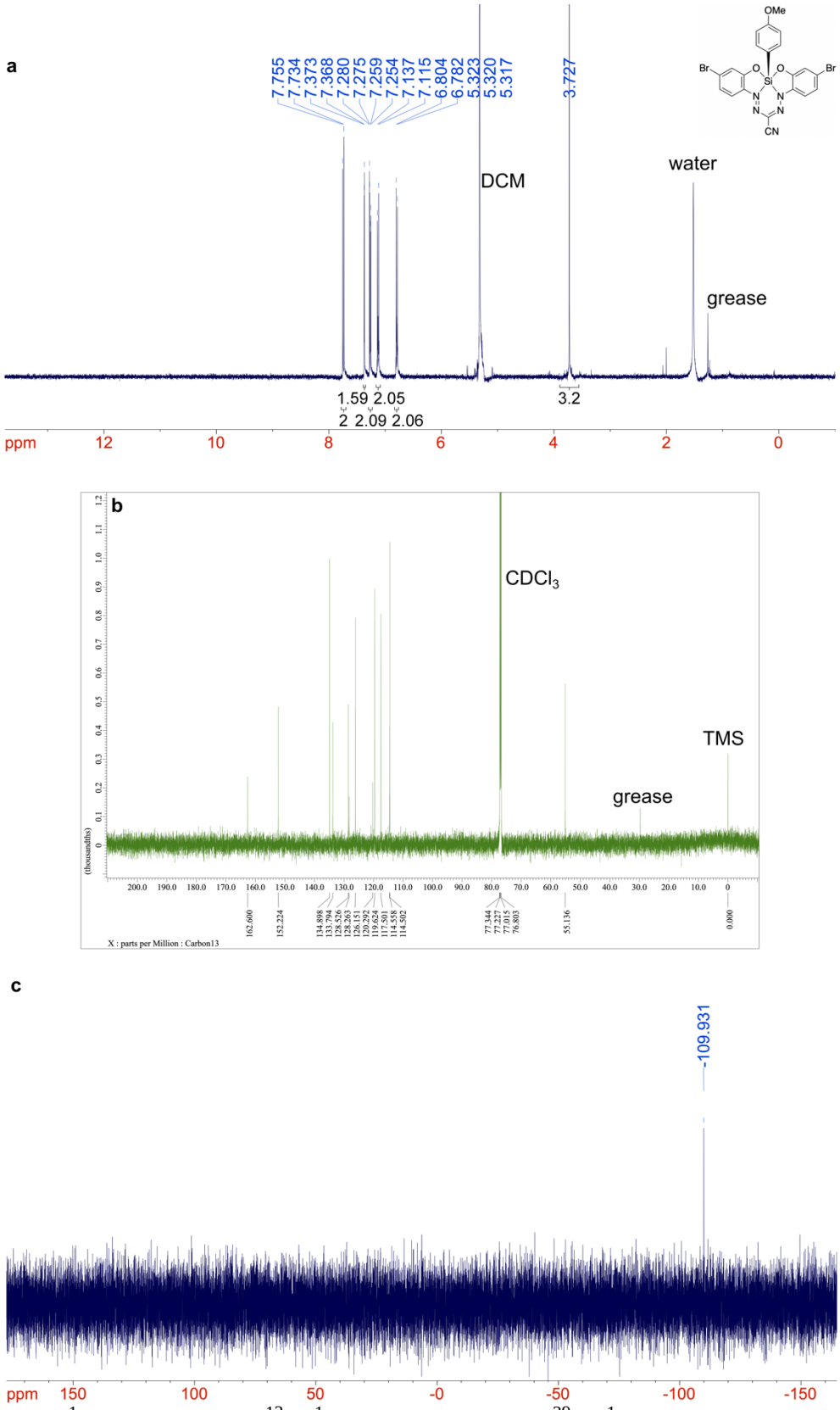

Figure S37. (a) ^{1}H in CD_2Cl_2, (b) $^{13}C\{^{1}H\}$ in $CDCl_3$ and (c) $^{29}Si\{^{1}H\}$ in CD_2Cl_2 NMR spectra of **SiPhOMe_Br**.

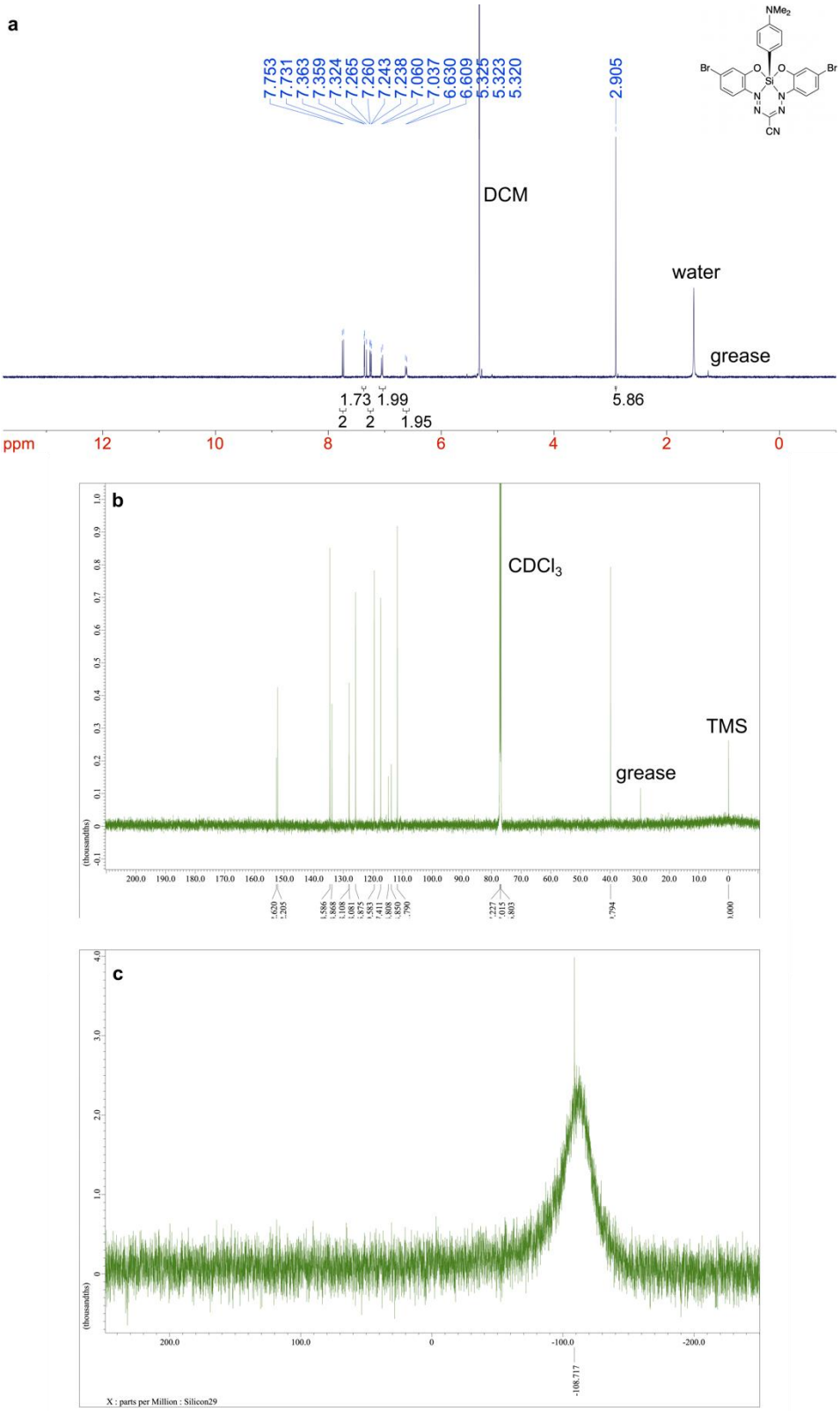

Figure S38. (a) ^{1}H in CD_2Cl_2, (b) $^{13}C\{^{1}H\}$ in $CDCl_3$ and (c) $^{29}Si\{^{1}H\}$ in CD_2Cl_2 NMR spectra of **SiPhNMe_Br**.

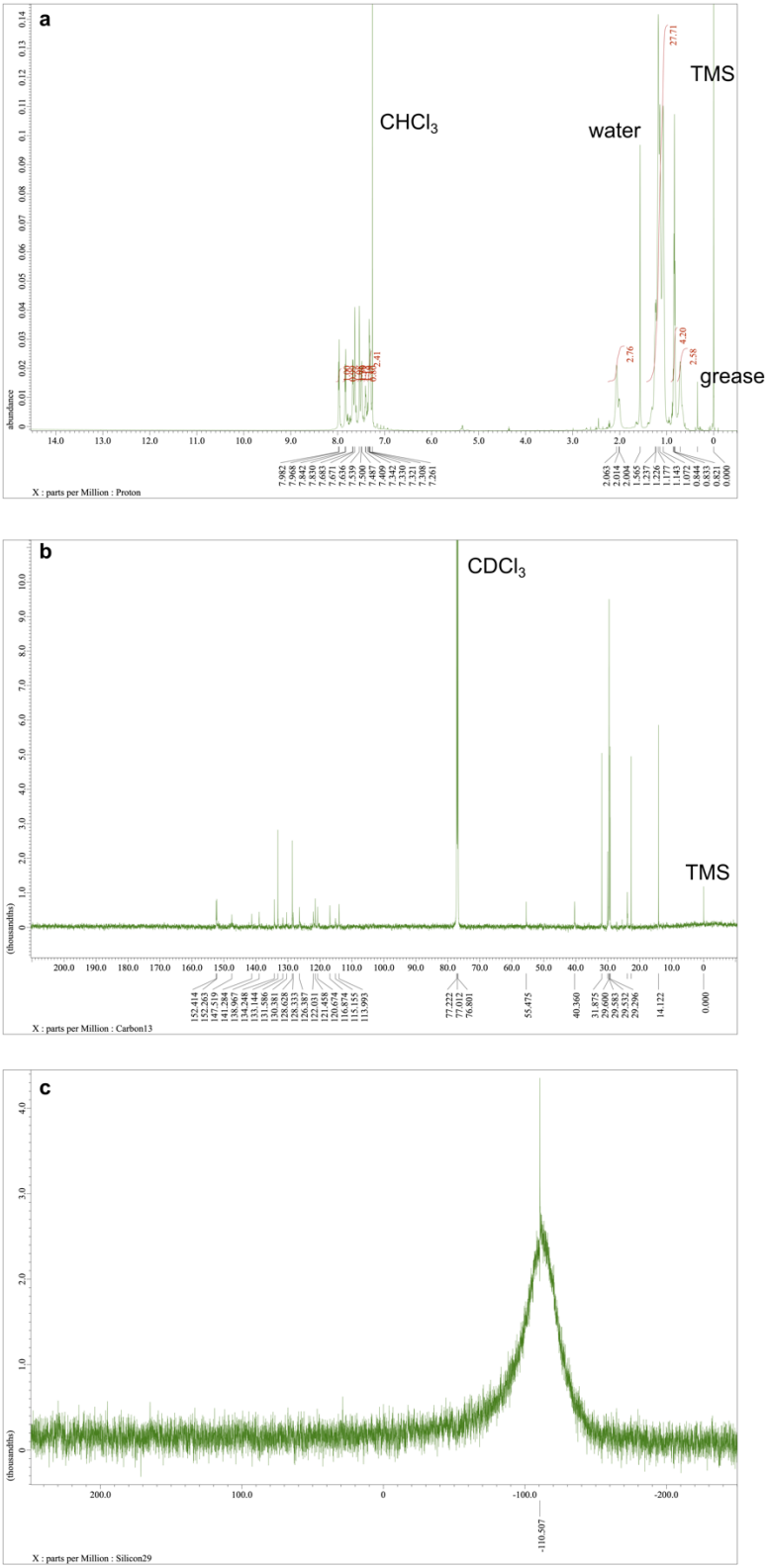

Figure S49. (a) ^{1}H, (b) ^{13}C{^{1}H} and (c) ^{29}Si{^{1}H} NMR spectra of **pSi_FL** in $CDCl_3$.

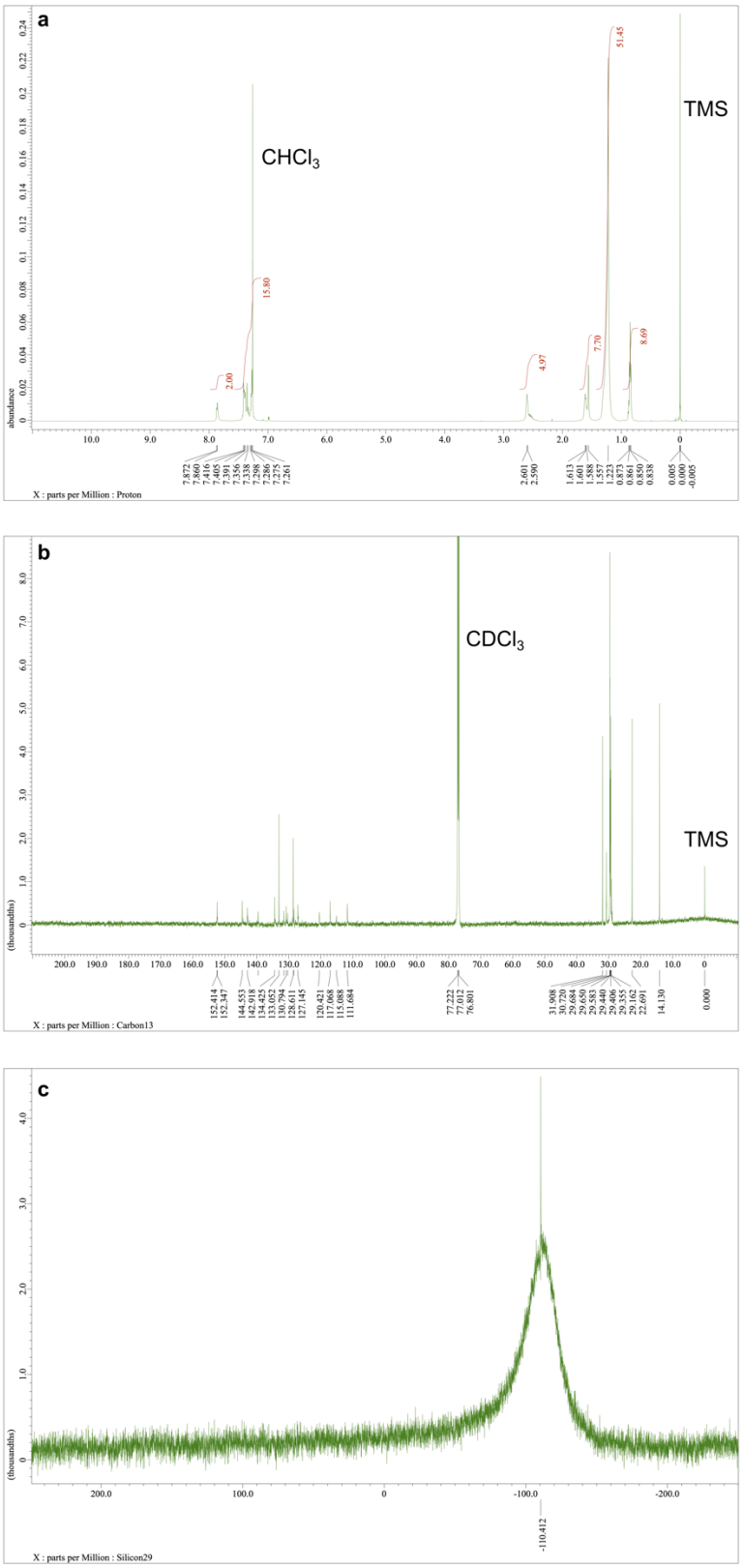

Figure S50. (a) ^{1}H, (b) ^{13}C{^{1}H} and (c) ^{29}Si{^{1}H} NMR spectra of **pSi_BT** in $CDCl_3$.

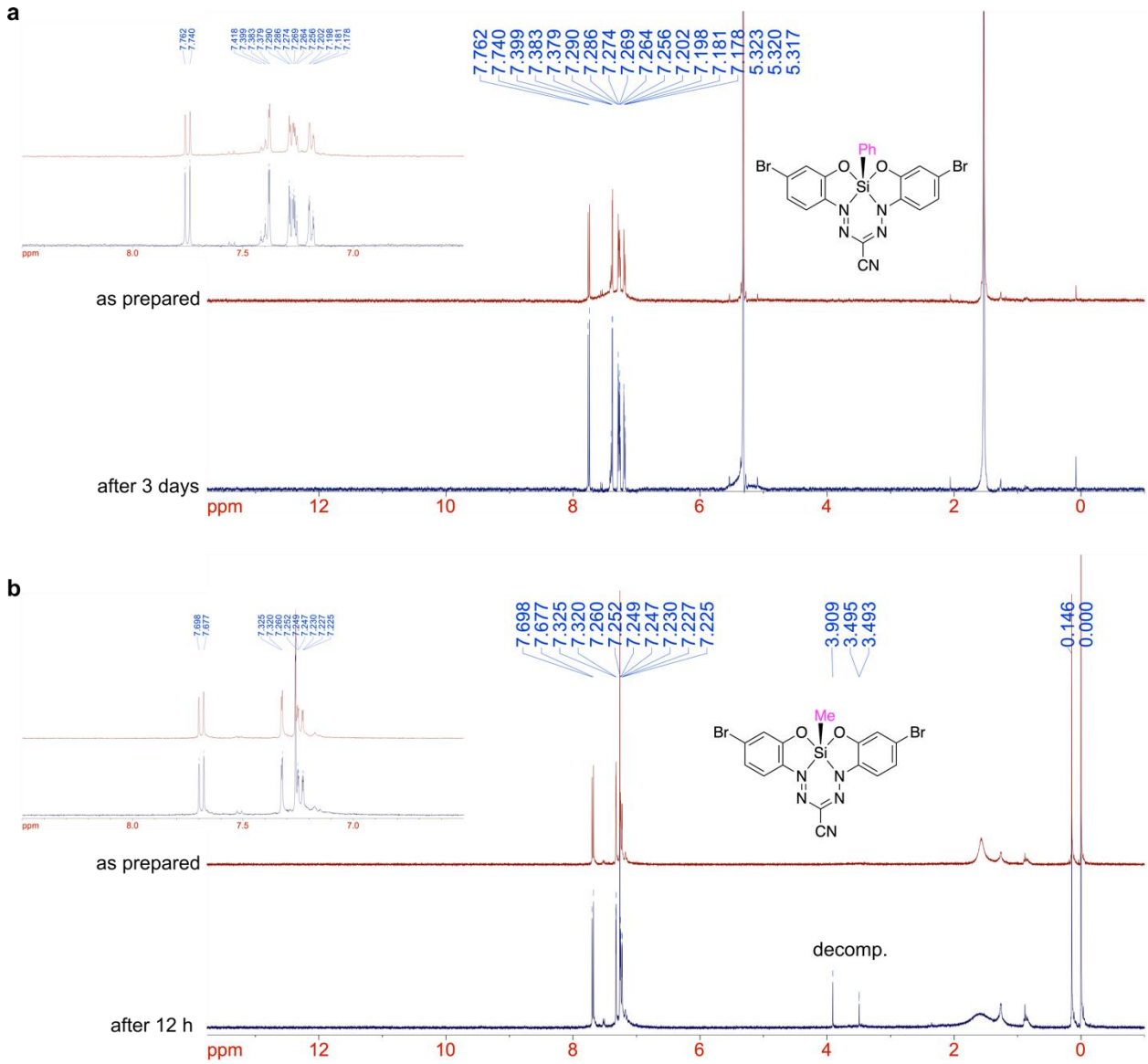

Figure S51. Stability test for (a) **SiPh_Br** in CD_2Cl_2 and (b) **SiMe_Br** in $CDCl_3$. Decomposition products were observed in the spectrum of **SiMe_Br** 12 h after the solution preparation, while the spectrum of **SiPh_Br** did not show any apparent changes even 3 days after the solution preparation.

References in Supporting Information

[1] A.W. Addison, T.N. Rao, J. Reedijk, J. van Rijn, G.C. Verschoor, Synthesis, structure, and spectroscopic properties of copper(II) compounds containing nitrogen–sulphur donor ligands; the crystal and molecular structure of aqua[1,7-bis(*N*-methylbenzimidazol-2′-yl)-2,6-dithiaheptane]copper(II) perchlorate, J. Chem. Soc. Dalton Trans. (1984) 1349–1356.